

AD-A052 702

SIMULATION PHYSICS INC BEDFORD MA  
IEMP/SGEMP SIMULATION PROGRAM.(U)

F/G 20/14

UNCLASSIFIED

MAR 77 R G LITTLE, S H FACE, R A LOWELL

DNA001-76-C-0134

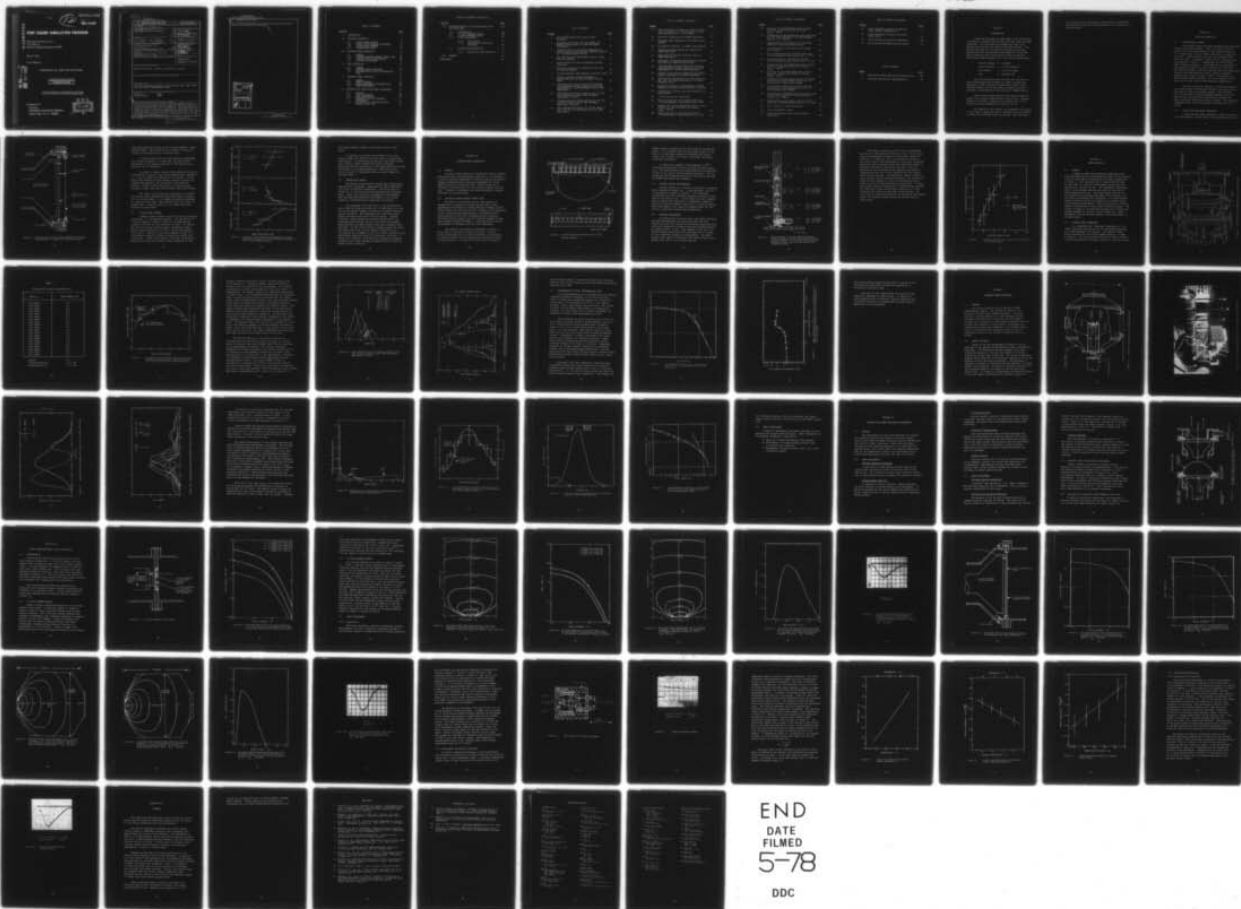
SPI-FR-10041

DNA-4448F

NL

| OF |

AD  
A052 702



END  
DATE  
FILMED  
5-78  
DDC

AD A 052702

12

AD-E300 146

DNA 4448F

# IEMP/SGEMP SIMULATION PROGRAM

Simulation Physics, Inc.  
P.O. Box D  
Bedford, Massachusetts 01730

March 1977

Final Report

CONTRACT No. DNA 001-76-C-0134

APPROVED FOR PUBLIC RELEASE;  
DISTRIBUTION UNLIMITED.

THIS WORK SPONSORED BY THE DEFENSE NUCLEAR AGENCY  
UNDER RDT&E RMSS CODE B323076464 R99QAXEB08962 H2590D.

Prepared for  
Director  
DEFENSE NUCLEAR AGENCY  
Washington, D. C. 20305

DDC  
RECEIVED  
APR 13 1978  
B

AD NO. 1  
DDC FILE COPY

18 DNA, SBIE

UNCLASSIFIED

SECURITY CLASSIFICATION OF THIS PAGE (When Data Entered)

19 REPORT DOCUMENTATION PAGE		READ INSTRUCTIONS BEFORE COMPLETING FORM
1. REPORT NUMBER DNA 4448F, AD-E302 146	2. GOVT ACCESSION NO.	3. RECIPIENT'S CATALOG NUMBER
4. TITLE (and Subtitle) IEMP/SGEMP SIMULATION PROGRAM.	5. TYPE OF REPORT & PERIOD COVERED Final Report.	6. PERFORMING ORG. REPORT NUMBER SPI-FR-10041
7. AUTHOR(s) R. G. Little, ↓ R. A. Lowell S. H. Face, W. A. Seidler	8. CONTRACT OR GRANT NUMBER(s) DNA 001-76-C-0134	10. PROGRAM ELEMENT, PROJECT, TASK AREA & WORK UNIT NUMBERS NWED Subtask R99QAXEB089-62
9. PERFORMING ORGANIZATION NAME AND ADDRESS Simulation Physics, Inc. P. O. Box D Bedford, Massachusetts 01730	11. CONTROLLING OFFICE NAME AND ADDRESS Director Defense Nuclear Agency Washington, D. C. 20305	12. REPORT DATE March 1977
14. MONITORING AGENCY NAME & ADDRESS (if different from Controlling Office)	13. NUMBER OF PAGES 90	15. SECURITY CLASS (of this report) UNCLASSIFIED
16. DISTRIBUTION STATEMENT (of this Report) Approved for public release; distribution unlimited.		
17. DISTRIBUTION STATEMENT (of the abstract entered in Block 20, if different from Report)		
18. SUPPLEMENTARY NOTES This work sponsored by Defense Nuclear Agency under RDT&E RMSS Code B323076464 R99QAXEB08962 H2590D.		
19. KEY WORDS (Continue on reverse side if necessary and identify by block number) Simulation IEMP Electron Beams SGEMP		
20. ABSTRACT (Continue on reverse side if necessary and identify by block number) This report presents the status of IEMP and SGEMP simulations with pulsed low voltage electron beams and describes certain low voltage bremsstrahlung X-ray environments. The techniques for producing electron beams of the appropriate characteristics and employing them in simulation geometries are described. The diagnostic approaches to characterizing both electron and X-ray environments are discussed. Data are presented for specific IEMP and SGEMP simulation examples.		

DD FORM 1473 1 JAN 73

EDITION OF 1 NOV 65 IS OBSOLETE

UNCLASSIFIED

SECURITY CLASSIFICATION OF THIS PAGE (When Data Entered)

390 900

UNCLASSIFIED

SECURITY CLASSIFICATION OF THIS PAGE(When Data Entered)

20. ABSTRACT (Continued)

Low voltage bremsstrahlung environments produced using these pulsed electron beams are described.

ACCESSION for	
NTIS	White Section <input checked="" type="checkbox"/>
DDC	Buff Section <input type="checkbox"/>
UNANNOUNCED	<input type="checkbox"/>
JUSTIFICATION _____	
BY _____	
DISTRIBUTION/AVAILABILITY CODES	
Dist. Avail. and/or SPECIAL	
A	

UNCLASSIFIED

SECURITY CLASSIFICATION OF THIS PAGE(When Data Entered)



## TABLE OF CONTENTS

<u>SECTION</u>	<u>PAGE</u>
I INTRODUCTION	7
II ELECTRON GENERATION	9
2.1 PULSED POWER SYSTEMS	9
2.2 DIODE PULSE-TAILORING TECHNIQUES	9
2.3 DIODE MIXING CHAMBER	13
2.4 TRANSMITTING ANODE	15
III ELECTRON BEAM DIAGNOSTICS	16
3.1 GENERAL	16
3.2 INJECTED ELECTRON ENERGY VERSUS TIME	16
3.3 CURRENT DENSITY MEASUREMENTS	18
3.4 ELECTRON RADIOGRAPHY	18
IV IEMP SIMULATION	22
4.1 GENERAL	22
4.2 INJECTED BEAM PARAMETERS	22
4.3 REPRESENTATIVE CAVITY PHENOMENOLOGY DATA	31
V EXTERNAL SGEMP SIMULATION	35
5.1 GENERAL	35
5.2 SGEMP APPARATUS	35
5.3 EMITTED ELECTRON CHARACTERISTICS	39
5.4 SGEMP EXPERIMENTS	47
VI CONCEPTS FOR OTHER IEMP/SGEMP EXPERIMENTS	48
6.1 GENERAL	48
6.2 IEMP EXPERIMENTS	48
6.3 SGEMP EXPERIMENTS	49
6.4 COMBINED X-RAY AND ELECTRON EXPERIMENTS	50
6.5 EVALUATION OF SIMULATOR VACUUM CHAMBER CLEAR TIME	50

# TABLE OF CONTENTS (Continued)

<u>SECTION</u>		<u>PAGE</u>
VII	CHARACTERIZATION OF X-RAYS PRODUCED WITH SPI-PULSE 6000	54
7.0	INTRODUCTION	54
7.1	2.5-INCH-DIAMETER SOURCE	54
7.2	12-INCH DIAMETER SOURCE	57
7.3	X-RAY CALORIMETER	57
	7.3.1 Description	57
	7.3.2 Calorimeter Calibration Technique	72
7.4	SCINTILLATOR/PHOTODIODE	79
	7.4.1 Description and Operation	79
VIII	SUMMARY	83
	REFERENCES	85

## LIST OF FIGURES

<u>FIGURE</u>		<u>PAGE</u>
1	SPI-PULSE <sup>TM</sup> Model 5000 Electron Beam Generator	11
2	Representative Diode, Mixing Chamber and Window Configuration for IEMP and SGEMP Experiments	12
3	Injected Current Pulse Width Dependence on Diode Pressure, Diode Gap and Charging Voltage for 12-Inch-Diameter Emitter	14
4	SPI 180° Magnetic Spectrometer with 10 Time-Resolved Channels	17
5	Design Aspects of 4-Ring Segmented Faraday Collector	19
6	Relative Sensitivity of Kodak AA X-Ray Film to Electron Energy	21
7	12-Inch-Diameter IEMP Apparatus (Quarter Scale)	23
8	Typical Injected Current Waveform as Determined with the Mixing Chamber Current Shunt	24
9	Injected Beam Current Density Distribution from Segmented Faraday Collector and X-Ray Radiograph for 12-Inch-Diameter Cavity IEMP Experiments	27
10	Time Resolved Electron Spectral Data for HDL 12-Inch-Diameter Cavity IEMP Benchmark Experiment (on axis)	29
11	Injected Electron Energy and Current for HDL 12-Inch-Diameter Cavity IEMP Benchmark Experiment (average)	30
12	Peak Transmitted Current vs. Cavity Depth at $10^{-4}$ Torr for 12-Inch-Diameter Cavity IEMP Experiments	32

# LIST OF FIGURES (Continued)

<u>FIGURE</u>		<u>PAGE</u>
13	Peak Transmitted Current vs. Cavity Pressure at 15 cm Depth for 12-Inch-Diameter Cavity IEMP Experiments ( $t = 35$ ns fwhm)	33
14	Diagram of Apparatus for SGEMP Experiments	36
15	SPI-PULSE 6000 Attached to the SGEMP Vacuum Chamber	37
16	Cylindrical "Emitter" in SGEMP Vacuum System	38
17	Injected Electron Energy and Current for SGEMP Experiment	40
18	Time Resolved Electron Spectral Data for SGEMP Experiment	41
19	Comparison of Average Time-Integrated Spectra for IEMP and SGEMP Configurations	43
20	Injected Beam Current Density Distribution from Segmented Faraday Collector and X-Ray Radiograph for 12-Inch SGEMP Experiment	44
21	Electron Distribution Determined with Radiographic Techniques for SGEMP Experiment	45
22	Peak Transmitted Current vs. Cavity Depth at $10^{-4}$ Torr for SGEMP Experiment in 12-Inch-Diameter Cavity	46
23	Conceptual Designs for Hemispherical SGEMP Emission and Side-on IEMP Cylinder Injection	51
24	Simultaneous Electron and X-Ray Exposure for TREE Studies	52
25	2.5-Inch-Diameter X-Ray Source	55
26	Axial Fluence Map for SPI-PULSE 6000 with 2.5-Inch-Diameter X-Ray Source; Gap = 8 mm	56
27	Fluence Map for SPI-PULSE 6000 with 2.5-Inch-Diameter X 0.005-Inch-Thick Ta Target; $E_{\text{PEAK}} = 200\text{keV}$	58
28	Axial Dose Map for SPI-PULSE 6000 with 2.5-Inch-Diameter X-Ray Source; Gap = 8 mm	59



# LIST OF FIGURES (Continued)

<u>FIGURE</u>		<u>PAGE</u>
29	Dose Map for SPI-PULSE 6000 with 12-Inch-Diameter, 0.005-Inch Thick Ta Target; $E_{\text{PEAK}} = 200\text{keV}$	60
30	Representative Bremsstrahlung Energy Spectrum for SPI-PULSE 6000 with 2.5-Inch-Diameter Source; $V_o = 300 \text{ keV}$	61
31	Bremsstrahlung Time History for SPI-PULSE 6000 with 2.5-Inch-Diameter Source	62
32	12-Inch-Diameter X-Ray Source and Vacuum Test Chamber	63
33	Axial Fluence Map for SPI-PULSE 6000 with 12-Inch-Diameter X-Ray Source; Gap = 1.5 cm	64
34	Axial Dose Map for SPI-PULSE 6000 with 12-Inch-Diameter X-Ray Source; Gap = 1.5 cm	65
35	Fluence Map for SPI-PULSE 6000 with 12-Inch-Diameter, 0.00035-Inch-Thick Ta Target; $E_{\text{PEAK}} = 120\text{keV}$	66
36	Dose Map for SPI-PULSE 6000 with 12-Inch-Diameter, 0.00035-Inch-Thick Ta Target; $E_{\text{PEAK}} = 120\text{keV}$	67
37	Extrapolated X-Ray Fluence Map for SPI-PULSE 6000 with 12-Inch-Diameter Source for 10-Foot-Diameter Vacuum Test Chamber	68
38	Extrapolated X-Ray Dose Map for SPI-PULSE 6000 with 12-Inch-Diameter Source for 10-Foot-Diameter Test Chamber	69
39	Representative Bremsstrahlung Energy Spectrum for SPI-PULSE 6000 with 12-Inch-Diameter Source; $V_o = 300\text{keV}$	70
40	Bremsstrahlung Time History for SPI-PULSE 6000 with 12-Inch-Diameter Source; $V_o = 300\text{kV}$	71
41	SPI's Gold Foil X-Ray Calorimeter	73
42	X-Ray Calorimeter Output	74
43	X-Ray Calorimeter Output versus Ambient Temperature	76

# LIST OF FIGURES (Continued)

<u>FIGURE</u>		<u>PAGE</u>
44	X-Ray Calorimeter Output Calibration versus Ambient Temperature	77
45	X-Ray Calorimeter Sensitivity versus Output Level	78
46	SPI's 500 mHz Scintillator Photodiode	80
47	Scintillator/Photodiode Typical Output	82

# LIST OF TABLES

<u>TABLE</u>		<u>PAGE</u>
1	Nominal SPI-PULSE Generator Characteristics	10
2	Injected Peak Current Reproducibility	26

## SECTION I

### INTRODUCTION

Significant progress has been made in the development of pulsed low voltage electron beams for both IEMP and SGEMP simulation! The electrons are produced by flash X-ray pulsed power systems with large area plasma cathodes. The emitted electrons are utilized by allowing them to pass through very thin transmitting anode mesh/foil structures. Their characteristics, which can be varied by changing machine and diode parameters fall into the following ranges:

Electron Energy,  $V = 1-100\text{keV}$

Current Density,  $J = 0.1-100 \text{ amps/cm}^2$

Pulse Width,  $t = 2-100 \text{ ns (fwhm)}$

Area,  $A = 100-1000 \text{ cm}^2$

Such electrons have been injected into cavities of varying geometries and pressures in order to assess the magnitude of IEMP currents and associated fields.<sup>2-6</sup> Also, inverted geometries have been used to simulate exterior emission of photoelectrons from surfaces in SGEMP studies.<sup>7</sup>

These electron beam machines have been modified to produce low voltage bremsstrahlung X-rays using a tantalum target as the anode. Maximum X-ray fluences of  $2 \times 10^{-3} \text{ cal/cm}^2$  have been produced over areas of  $30 \text{ cm}^2$ .

The purpose of this report is to summarize the status of this type of simulation and to indicate areas of research to which the technology might be applied. The techniques

for producing and characterizing these beams are described. Representative IEMP and SGEMP experiments are discussed and data presented.



## SECTION II

### ELECTRON GENERATION

#### 2.1 PULSED POWER SYSTEMS

The electron beams have been produced using Simulation Physic's SPI-PULSE machines. These are solid dielectric coaxial lines with approximately 2 ohm impedance that are d.c. charged with a Van de Graaff generator to voltages up to 500 kV. Three machines are used, the SPI-PULSE 2500, 5000, and 6000. A summary of their nominal characteristics is presented in Table 1. A photograph of the SPI-PULSE 5000 is shown in Figure 1. The difference in generators is the voltage to which they can be charged (the SPI-PULSE 6000 has the highest) and the front-end discharge geometries. The 6000 has been modified to have a lower inductance geometry than either the 2500 or 5000. This results in a faster diode current risetime: 25 ns as compared to 50 ns and 40 ns for the 2500 and 5000 machines, respectively.

Once the machine is charged to the desired voltage, the stored energy is discharged through a gas switch into a diode with a large area plasma cathode. The SPI-PULSE 2500 and 5000 have a single breakdown channel, while the 6000 has six trigatron-initiated parallel channels for lower inductance and faster current risetime. The trigatron arrangement also allows synchronous switching with  $\pm 2$  ns jitter.

#### 2.2 DIODE PULSE TAILORING TECHNIQUES

A representative diode geometry is shown in Figure 2. An 8-inch-diameter, 40-ohm vacuum coax expands through an 8-

Table 1  
Nominal SPI-PULSE Generator Characteristics

PARAMETER	SPI-PULSE		
	2500	5000	6000
Impedance	1.6 ohm	1.8 ohm	1.8 ohm
Charging Voltage	150 kV	300 kV	500 kV
Electron Energy	1-80 keV	1-150 keV	1-250 keV
Peak Current	20 kA	35 kA	50 kA
Current Risetime	50 ns	40 ns	25 ns
Pulse width at Half-Maximum	3-150 ns	3-250 ns	3-400 ns
Size	3' Dia. x 15' Long	3' Dia. x 15' Long	3' Dia. x 15' Long

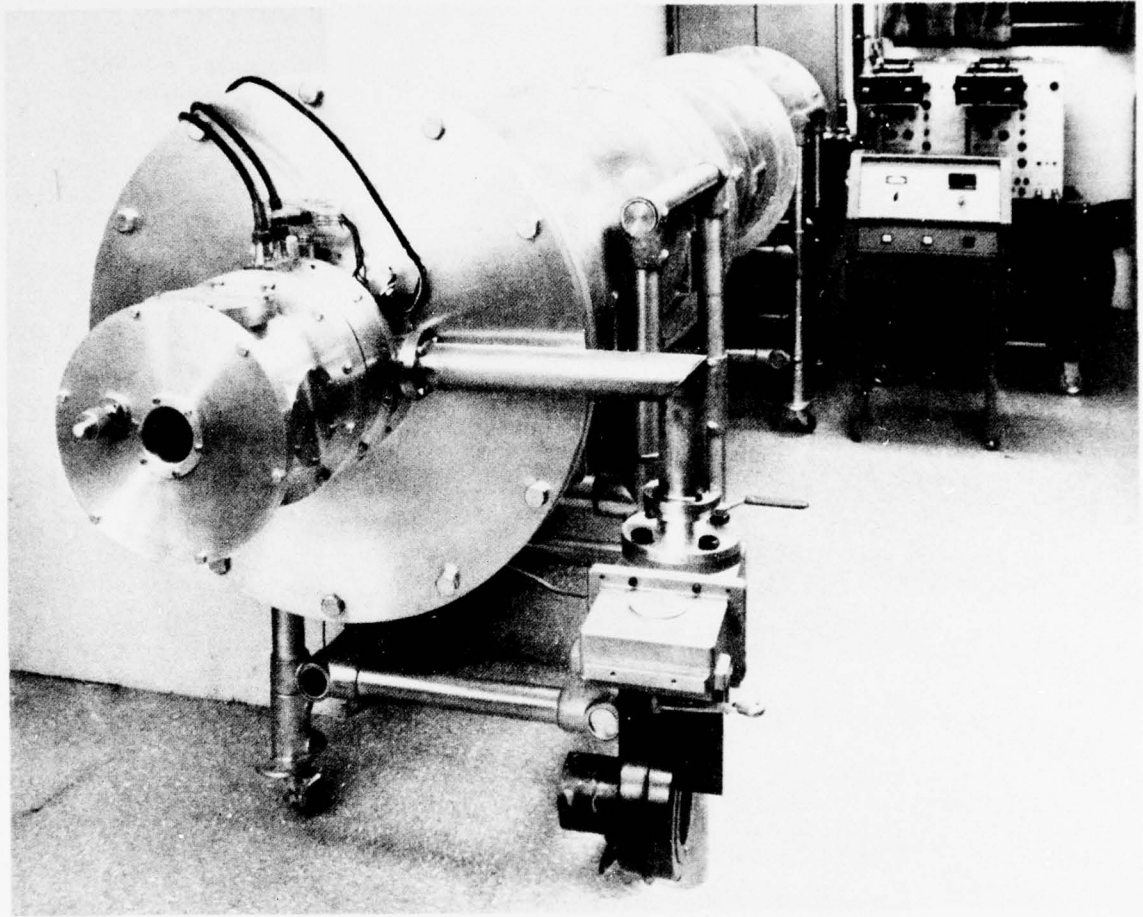


Figure 1. SPI-PULSE™ Model 5000 Electron Beam Generator

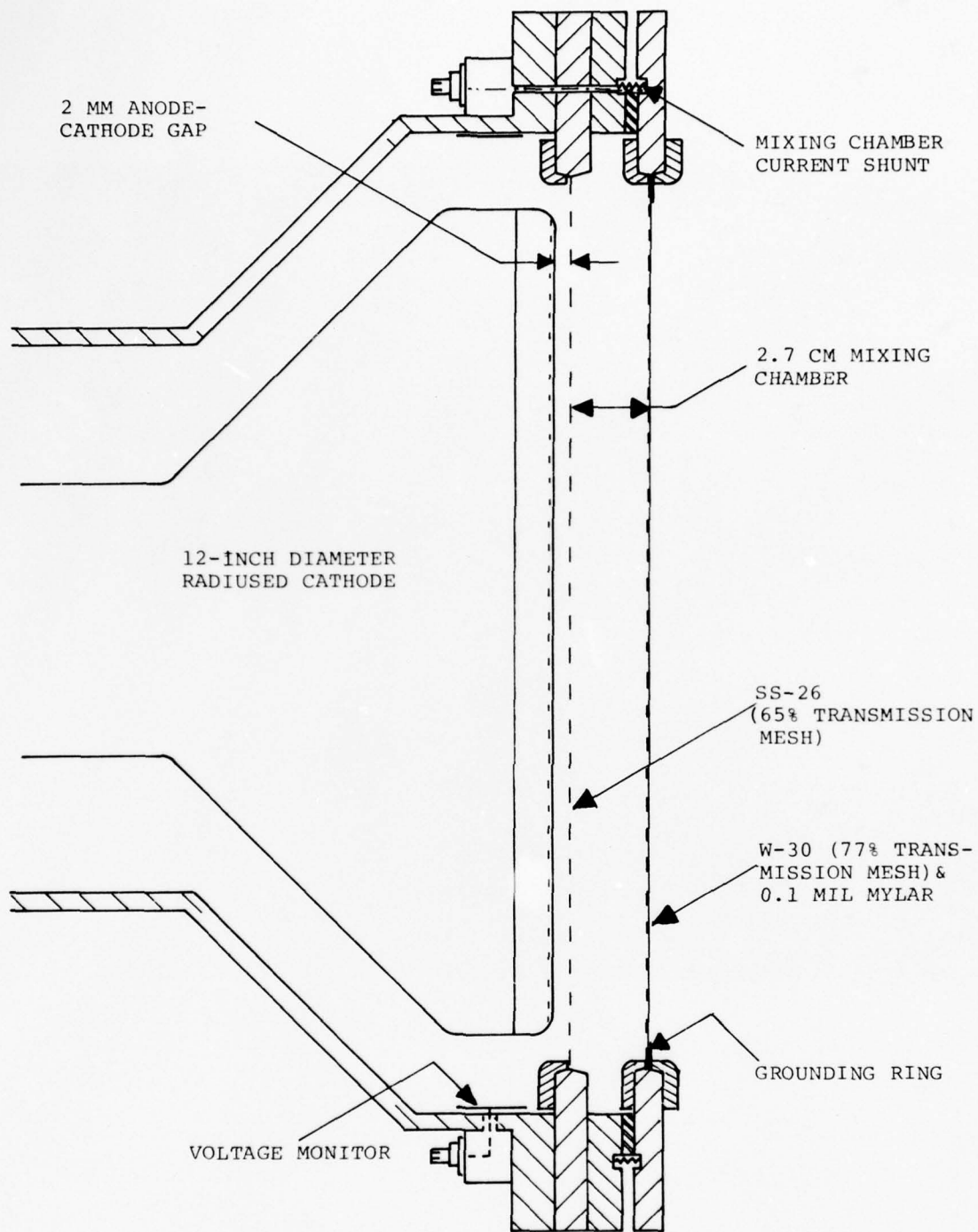


Figure 2. Representative Diode, Mixing Chamber and Window Configuration for IEMP and SGEMP Experiments.



inch-long transition section into a 12-inch-diameter, 9-ohm cathode holder. The surface of the cathode is textured to initiate field emission over its entire area.

In normal operations the diode exhibits underdamped R-L-C Circuit response. In this case, the pulse width corresponds to the ringing frequency of the system and is typically 120 ns (baseline).

In order to achieve shorter pulse widths the diode is "crow-barred" by using a very narrow anode-cathode separation (1 - 3 mm) and adding low-density air in the gap. A given pulse width depends upon the machine charging voltage, the cathode edge geometry, the gap spacing, and diode air pressure. Figure 3 shows the effect of varying machine charging voltage, gap, and diode pressure upon pulse widths.

The effect of this crow-bar technique is to shorten the current pulse transmitted through the anode by cutting off its trailing edge, i.e. by completing machine discharge in a short-circuit mode. The technique does not effect the leading edge. Pulses as short as 1 ns (fwhm) have been achieved in this manner.

### 2.3 DIODE MIXING CHAMBER

Cathode emission tends to be in the form of uniformly distributed 2 - 3 mm diameter beamlets. By the addition of a "mixing chamber", shown in Figure 2, the beamlets are allowed to mix and the fine structure is lost. For some of the very low voltage electron beams, considerable space charge limiting would occur in the 1-inch mixing chamber drift region. Therefore, the mixing chamber is kept at an intermediate pressure to allow for some space charge neutralization. Figure 2 also shows a front end configuration employing an anode mesh without a Mylar diaphragm so that

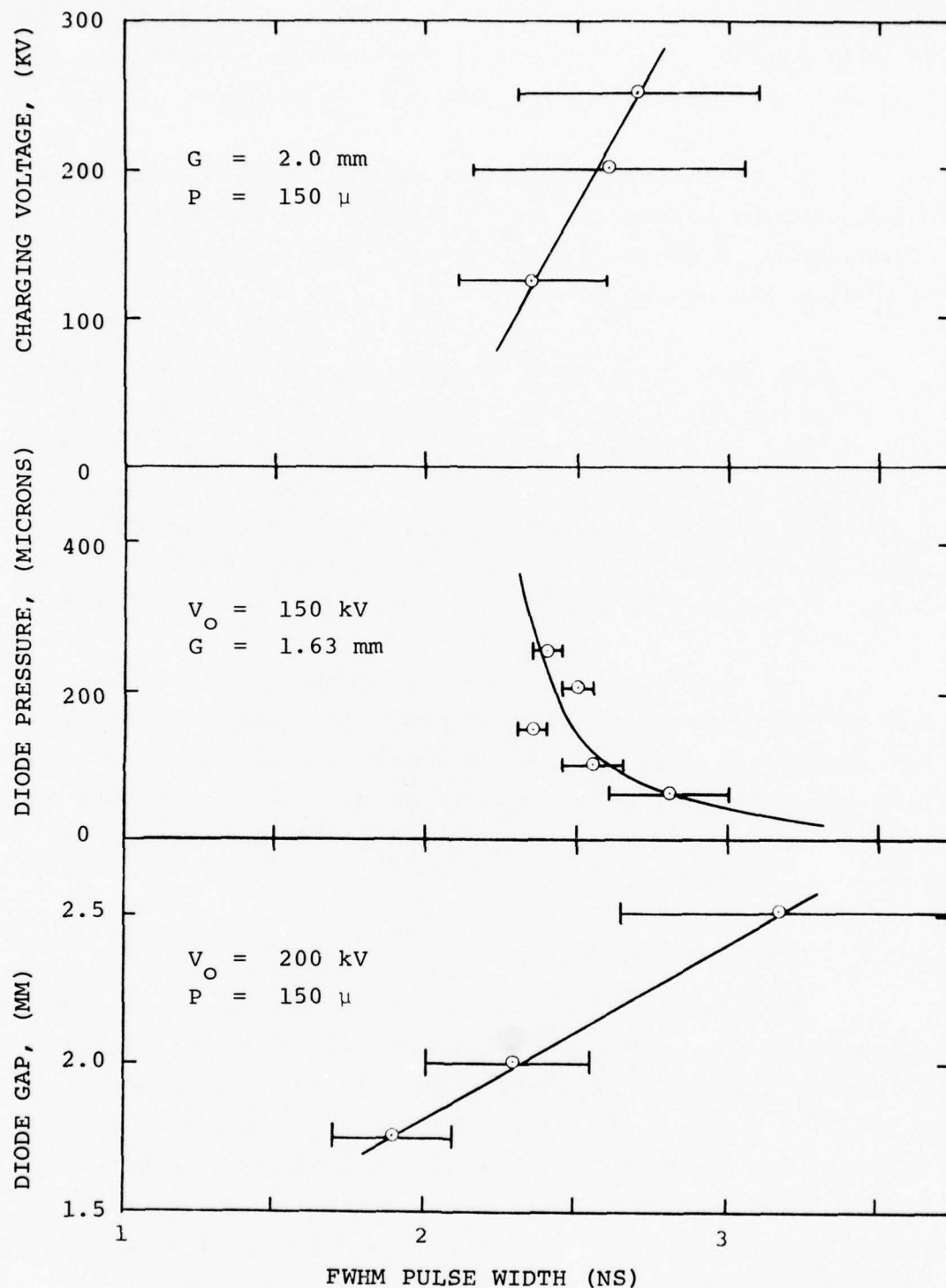


Figure 3. Injected Current Pulse Width Dependence on Diode Pressure,  $P$ , Diode Gap,  $G$ , and Charging Voltage,  $V_O$ , for 12-Inch-Diameter Emitter

the mixing chamber pressure is the same as that of the diode.

In addition to allowing the beamlets to mix, the mixing chamber also employs a current shunt to measure the beam current. A current monitor placed at the diode records total current, which includes the current component associated with the conduction of low-energy electrons through the plasma in the anode/cathode gap. This diode short-circuit current is segregated from the mixing chamber by the anode mesh.

#### 2.4 TRANSMITTING ANODE

The emitted electrons pass through thin transmitting mesh and foil structures. Representative mesh characteristics allow 77% optical transmission. The foils used are either 0.1 or 0.25 mil-thick non-aluminized and aluminized Mylar. Again, the particular configuration used depends upon the beam being generated and whether or not mixing chambers or extended machine geometries are present.

The thickness of the last foil in the configuration (this could be either the anode foil or that which is at the exit of the mixing chamber) is chosen to eliminate multiple electron transits. This phenomenon can occur when space-charge limiting occurs within the test cavity. Emitted electrons, turned around by the space-charge fields, are accelerated back through the foil into the mixing chamber diode gap where the space-charge field again reverses their direction. If the initial electron energy exceeds the energy loss associated with a triple transit through the foil, the electron will reappear in the test volume, thereby raising space-charge densities above the "realistic" condition. A proper foil thickness is determined by gradually increasing thickness until diode impedance characteristics and mixing chamber current stabilize.

## SECTION III

### ELECTRON BEAM DIAGNOSTICS

#### 3.1 GENERAL

In order to make meaningful comparisons between computer code predictions and phenomenology observed, it is necessary to have an accurate knowledge of electron injection parameters. Complete characterization requires measurement of current density across the injection plane, electron energy as a function of time and position, and electron angular distribution. A number of techniques have been developed to acquire this data on a routine basis.

#### 3.2 INJECTED ELECTRON ENERGY VERSUS TIME

The diode of the pulsed electron beam machine is equipped with a capacitive voltage monitor which, after appropriate corrections for shank inductive voltages, yields diode voltage as a function of time. However, this measurement is not a satisfactory determination of injected electron energy because of the error introduced by the inductive correction and the energy loss the electrons undergo as they pass through the mixing chamber. A time resolving electron spectrometer is therefore used for this measurement.

The magnetic spectrometer, diagrammed in Figure 4, gives electron energy as a function of time. Careful attention has been paid to electron dynamics in the design of the spectrometer and its magnetically shielding mu-metal collimation slits. An array of 10 equal area rectangular



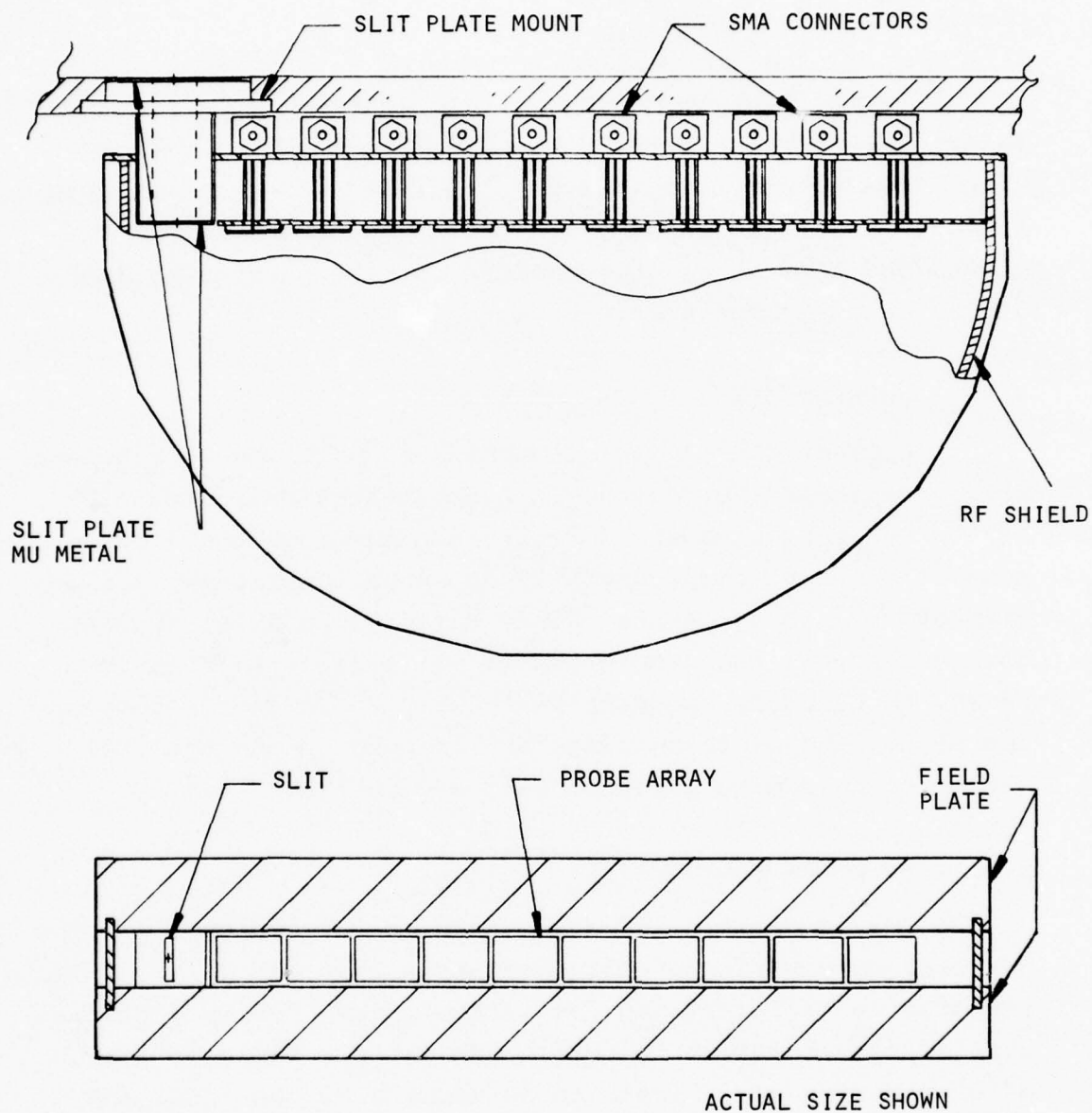


Figure 4. SPI 180° Magnetic Spectrometer with 10 Time Resolved Channels

copper probes is placed at the focal plane of the spectrometer. A 1/e response time for each probe signal of less than 0.3 ns has been achieved by extending the coaxial signal line to within 1/16 inch of the probe, minimizing connection inductance.

In addition to magnetic field mapping, a  $\text{Cd}^{109}$  internal-conversion beta source has been used for calibration. The spectrometer can be positioned off the beam axis, as well as on, and at varying angular positions. Time resolved and time integrated spectra for the particular IEMP and SGEMP experiments were measured.

### 3.3 CURRENT DENSITY MEASUREMENTS

Current density as a function of position is measured with a segmented Faraday cup. A cross-sectional view of a 4 ring monitor is shown in Figure 5. Low inductance connections have been carefully designed to achieve a rise-time of less than 0.4 ns. Since Faraday cup axial symmetry does not permit the resolution of azimuthally asymmetric beams, an electron stopping plate with a  $\pi/4$  sector removed was placed ahead of the rings and stepped around the full circle to determine electron beam asymmetries.

### 3.4 ELECTRON RADIOGRAPHY

The sensitivity of X-ray film to low energy electrons has been demonstrated.<sup>15</sup> The data shows that the film sensitivity falls off rapidly with electron energy providing sufficient resolution to obtain additional characterization of electron beams. First, anode mapping of the total integrated charge distribution was performed and correlated to time integrated Faraday cup measurements. The radiography yields spacial information more readily than do the Faraday cups, but it is not time resolved.

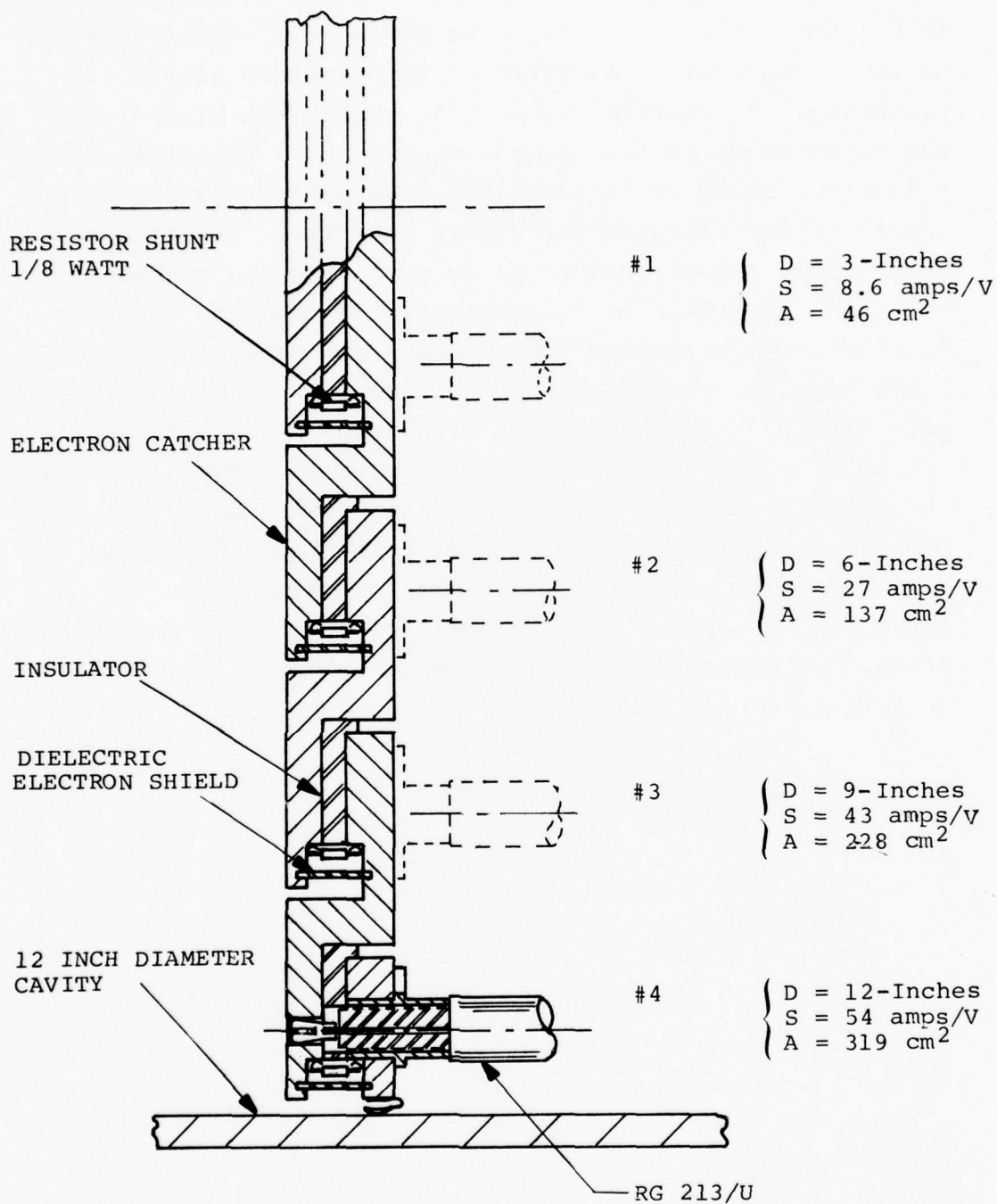


Figure 5. Design Aspects of 4-Ring Segmented Faraday Collector Where D is the Outer Diameter of the Electron Catcher, S is the Current Calibration in Amps per Volt, and A is the Area of the Collector Segment.

The electron deposition profile can be determined by placing a step wedge over the X-ray film. This profile gives an approximate estimate of the electron energy distribution. In addition, thin film strips are placed at the focal plane of the spectrometer to give time integrated spectra for those electrons which have sufficient energy to penetrate the emulsion and expose the film. The film sensitivity can be determined by comparing the spectrum obtained from the film to that obtained from the spectrometer channel response. The results are shown in Figure 6 along with the results obtained by Dudley.<sup>15</sup> The sensitivity scale has been changed to relative units because the No-screen film has a different absolute sensitivity. Finally, the electron angular distribution is determined by allowing the electrons to pass through small apertures in a thin aluminum plate placed on the anode of the machine. An X-ray film is placed approximately one cm behind the aperture plate; its exposure pattern gives the electron angular distribution.



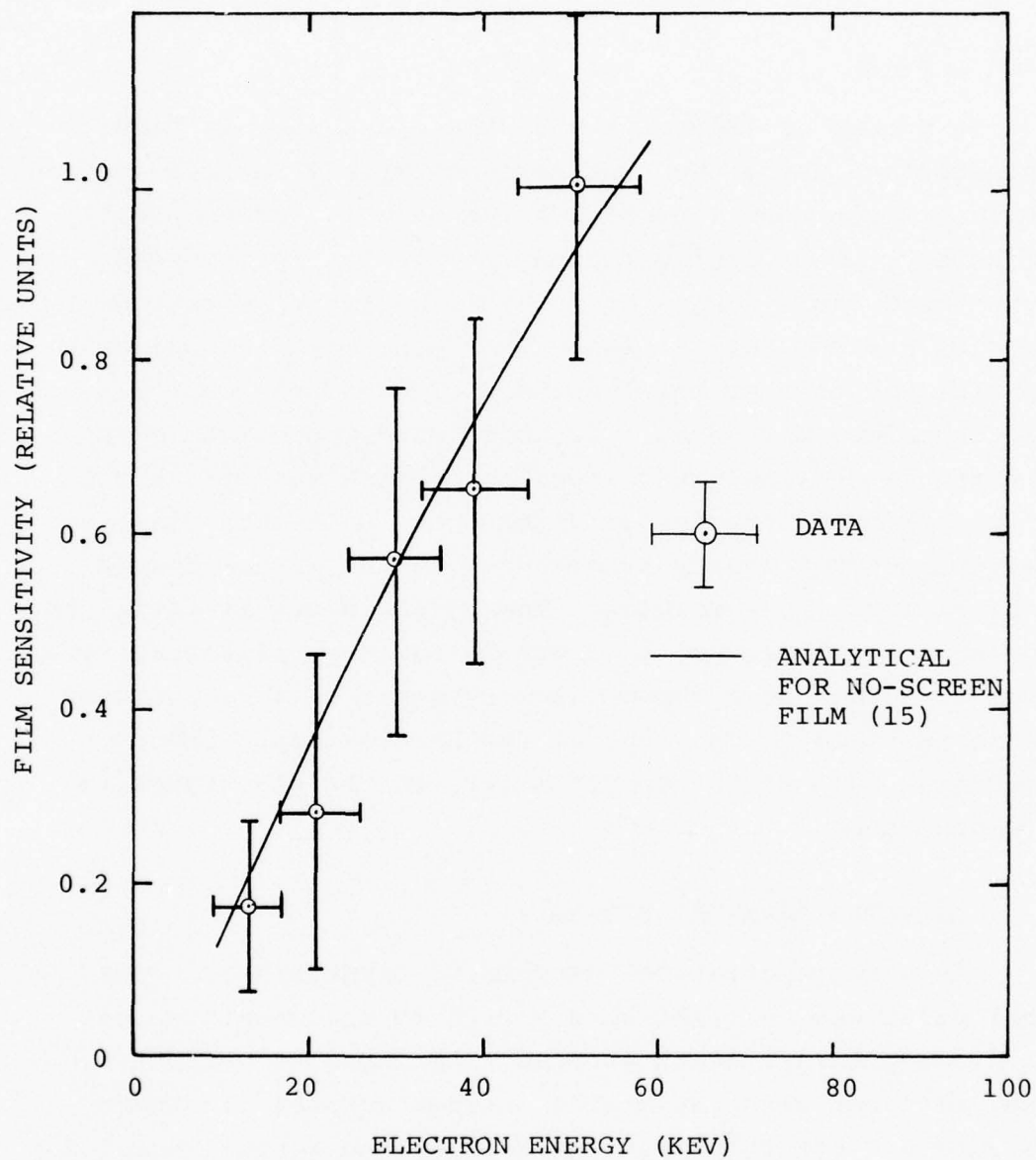


Figure 6. Relative Sensitivity of Kodak AA X-Ray Film to Electron Energy

## SECTION IV

### IEMP SIMULATION

#### 4.1 GENERAL

A number of IEMP cavity-response experiments have been performed using the techniques described in this section.<sup>8</sup> A typical experimental configuration is shown schematically in Figure 7. This configuration is essentially the same as that used for a series of "Benchmark" experiments conducted by SPI and HDL for DNA. The "Benchmark" experiments used a mixing chamber between the diode and test cavity; these experiments do not. The anode window consists of a 65% transmitting stainless steel mesh which supports a 0.1 mil-thick non-aluminum Mylar diaphragm. A 12-inch-diameter right-cylindrical cavity is attached to the window flange of the electron beam machine. The cavity depth is varied by changing the position of the movable Faraday collector. The cavity is housed in a vacuum tank by means of a vacuum feed-through assembly to the rear of the Faraday cup. Other implements, such as the spectrometer, can be positioned in the same manner.

#### 4.2 INJECTED BEAM PARAMETERS

In a representative "Benchmark" experiment, a 3 ns (fwhm) pulse was obtained with a 3.25 mm anode-cathode gap at a diode pressure of 60 microns. An injected current pulse, measured with the mixing chamber monitor, is shown in Figure 8. For this particular pulse the actual injected current measured with a Faraday collector in the test cavity

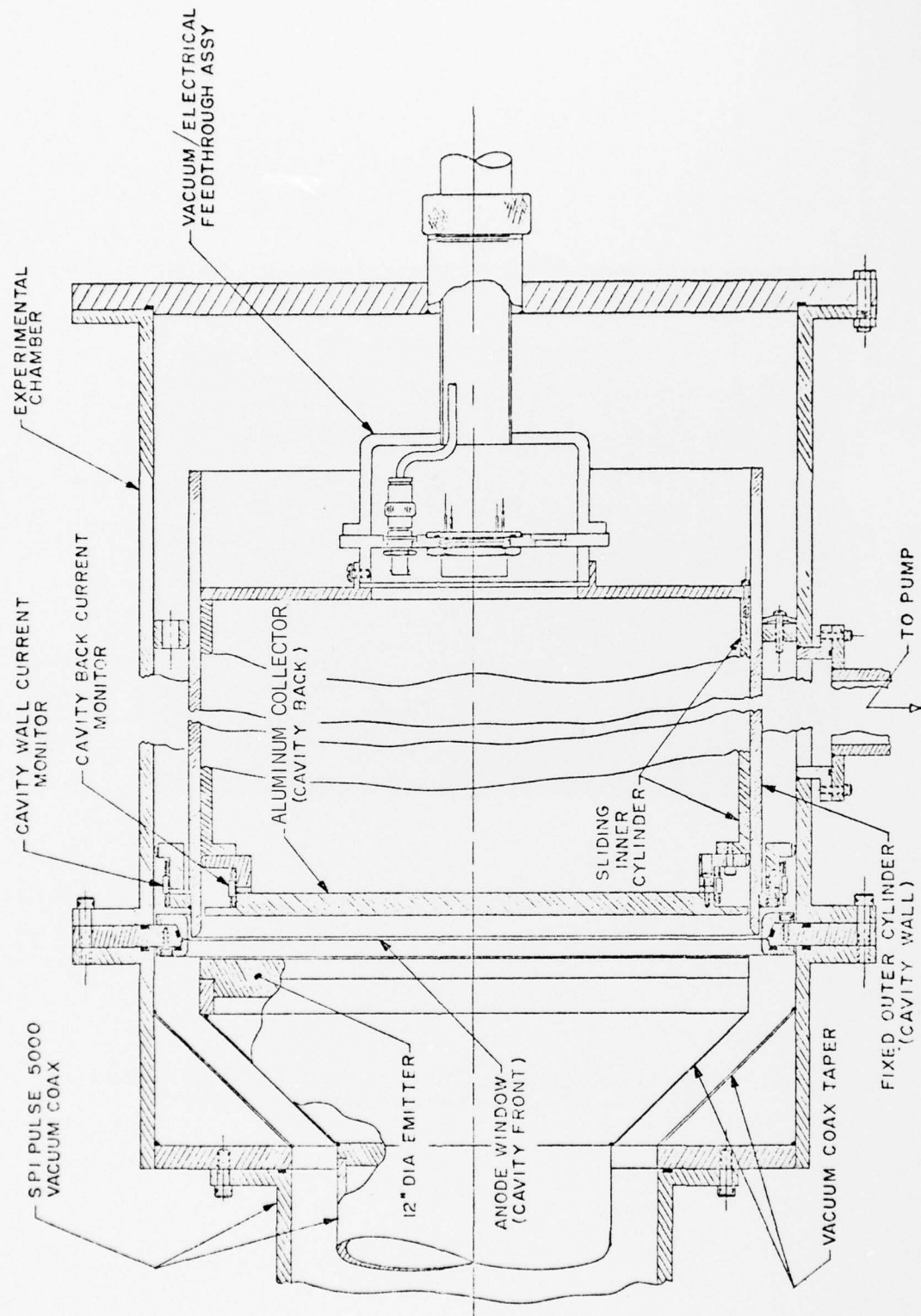
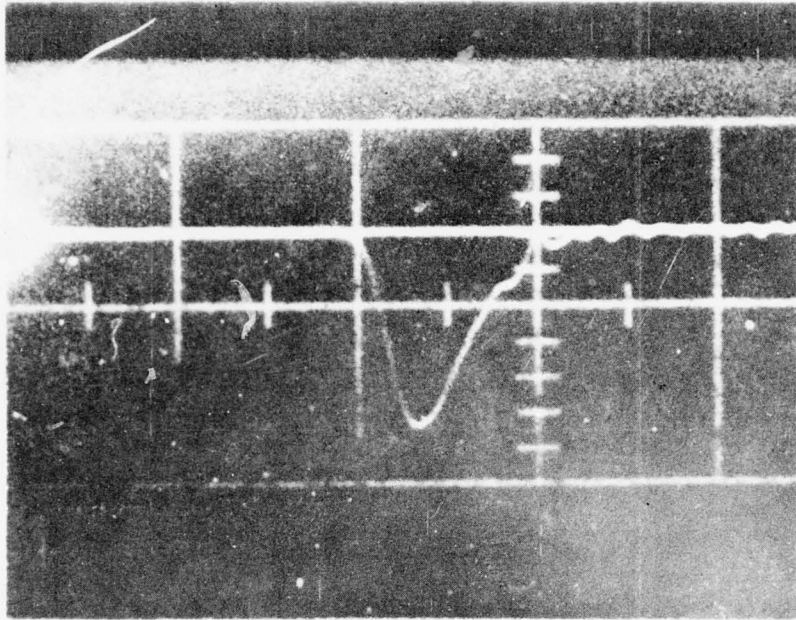


Figure 7. 12-Inch-Diameter IEMP Apparatus (Quarter Scale)



VERTICAL SENSITIVITY: 5.6 KA/DIV  
HORIZONTAL SWEEP: 5 NS/DIV

Figure 8. Typical Injected Current Waveform Measured  
with the Mixing Chamber Current Shunt



is within 10% of the mixing chamber current. There is a small decrease in amplitude and pulse width for the actual injected pulse. Table 2 lists peak current measurements for a series of 20 consecutive shots taken during the spectrometer run. The standard deviation of the peak current amplitude can be seen to be  $\pm 4\%$  with a maximum deviation of  $-6\%$ . This is representative of the reproducibility of the current pulse.

A sample radiograph of the injected current density pattern normalized to measurements made with the segmented Faraday collector is shown in Figure 9. In this instance, the current density distribution is somewhat nonuniform in radius. Distribution depends strongly upon the precise conditions of the cathode surface, the anode-cathode gap, and the configuration of the anode and mixing chamber. Annular, peaked and more uniform beams have been produced with different configurations. Once the diode has been fixed, the current density distribution remains relatively stable from shot to shot.

Although the diode is instrumented with a voltage monitor whose signal can be corrected to give the diode voltage as a function of time, it is questionable whether the diode voltage can be used to determine the injected electron energy as a function of time. First, it is difficult to make a cathode shank inductive voltage correction when a significant portion of the total current is short-circuit. Second, the electron energy is degraded during transit through the Mylar window to an extent dependent on the incident energy. The injected electron energy as a function of time is therefore best determined with the magnetic spectrometer.

In most cases, in order to obtain maximum resolution, the magnetic field is adjusted to give signals on 9 of the 10

TABLE 2

## Injected Peak Current Reproducibility

SHOT NO.	PEAK CURRENT (KA)
5138 (HD36)	4.9
5139 (HD37)	4.9
5140 (HD38)	4.8
5141 (HD39)	4.8
5142 (HD40)	4.8
5143 (HD41)	4.7
5144 (HD42)	5.0
5145 (HD43)	5.0
5146 (HD44)	4.9
5147 (HD45)	5.0
5148 (HD46)	4.8
5149 (HD47)	5.0
5150 (HD48)	4.9
5151 (HD49)	4.8
5152 (HD50)	4.8
5153 (HD51)	4.9
5154 (HD52)	4.9
5155 (HD53)	4.9
5156 (HD54)	4.8
5157 (HD55)	4.7

Average	4.9
Standard Deviation	$\pm 0.1$ (2%)
Maximum Deviation	- 0.2 (4%)

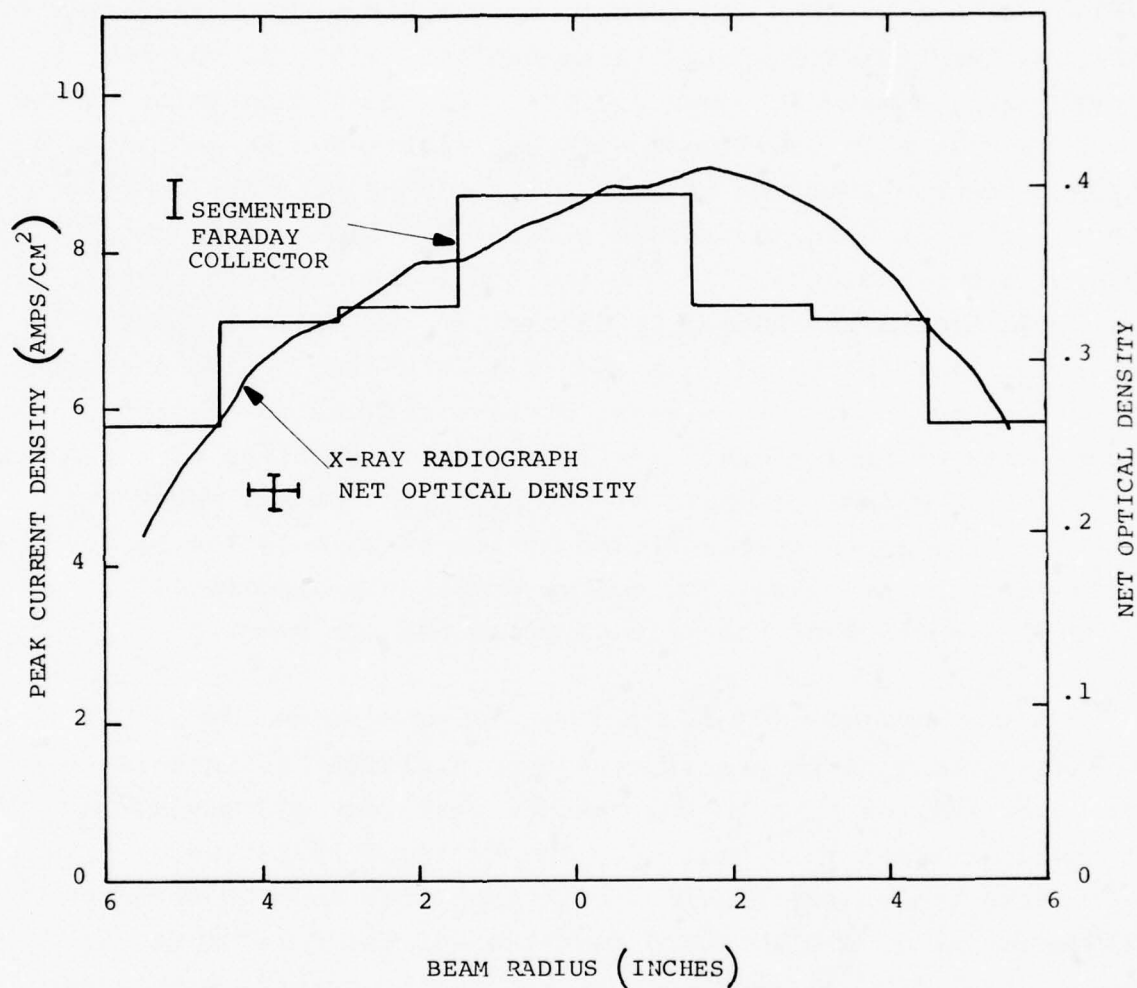


Figure 9. Injected Beam Current Density Distribution From Segmented Faraday Collector and X-Ray Radiograph for 12-Inch Diameter Cavity IEMP Experiments

channels (channel 10 gives no signal; verifying peak energy is on channel 9). Individual channel signals are shown in Figure 10 for one position of the spectrometer. The signals are chopped at a level corresponding to noise for clarity of presentation. The channel signals are time-synchronized using a fiducial mark. If a single beam oscilloscope, e.g. Tektronix 7904, is used the fiducial mark is duplexed with the channel signal using a matched power divider. For this experiment channel 8 was used as a fiducial mark after an additional length of delay cable was inserted to separate the channel signals. The channel signals were normalized according to the amplitude of channel 8 and timed relative to the other channel signals by their position with respect to channel 8. An additional time correction is applied to each channel, depending on the energy, to compensate for time-of-flight differences in the spectrometer. The channel signals are limited to a risetime of 1.2 ns due to the combined response of the oscilloscope and spectrometer. Also, since the magnitude of the current is low in the early part of the pulse, low energy components associated with the rising portion of the voltage pulse are not seen.

The electron energy as a function of time can be reconstructed from this data as shown in Figure 11. In this case, the average time of the channel peaks for all positions of the spectrometer is plotted. The vertical deviation represents the energy binwidth of the channel and the horizontal deviation is the standard deviation of the time of the channel peak for all positions of the spectrometer. Presented for comparison is the electron energy determined from the voltage monitor signal. The mixing chamber current is also shown to illustrate the timing of the injected current and the electron energy. These traces have been time-synchronized using a dual beam Tektronix 7844 oscilloscope, which triggers both beams simultaneously with a jitter of less than 50 ps.



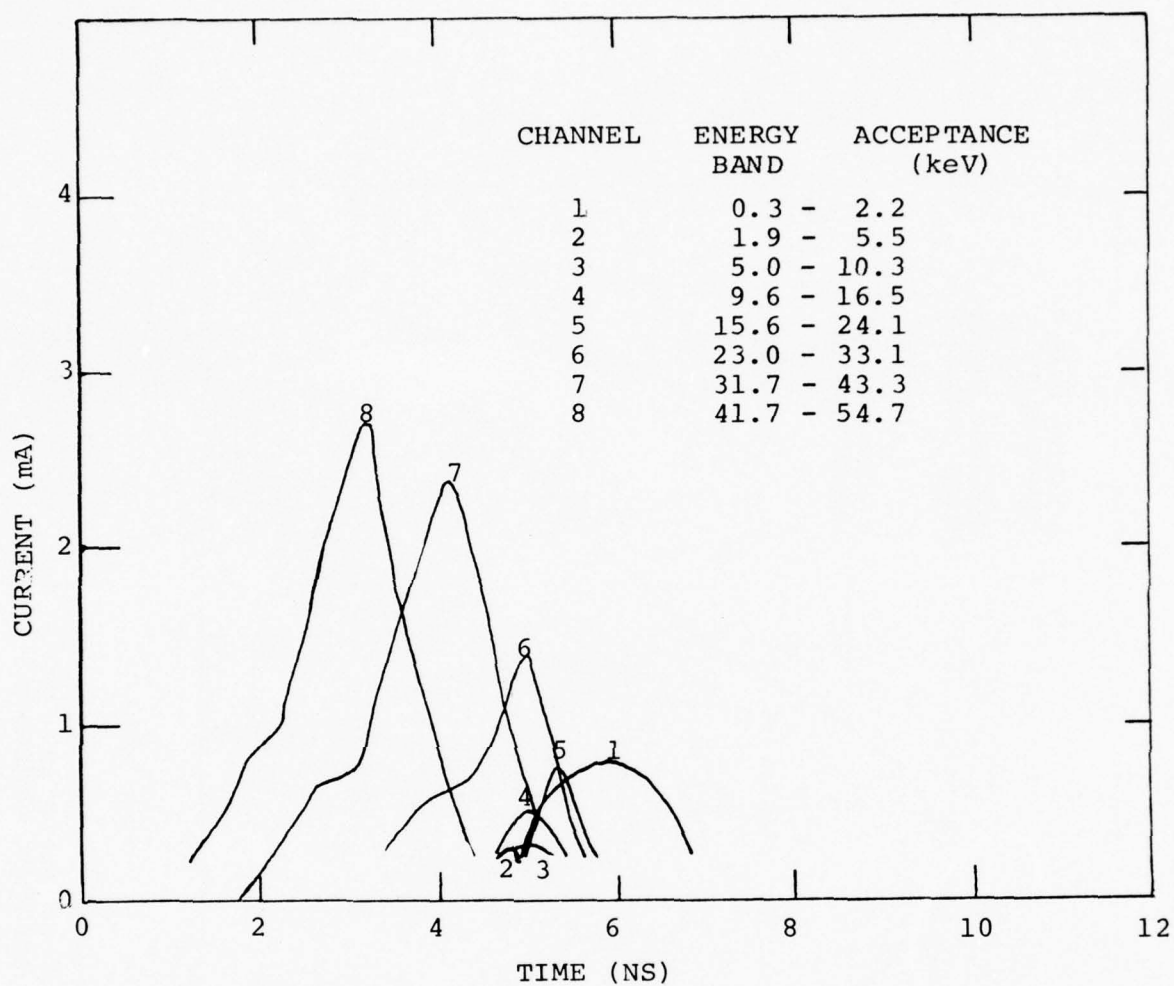


Figure 10. Time Resolved Electron Spectral Data for the HDL 12-Inch-Diameter Cavity IEMP Benchmark Experiment (on axis)

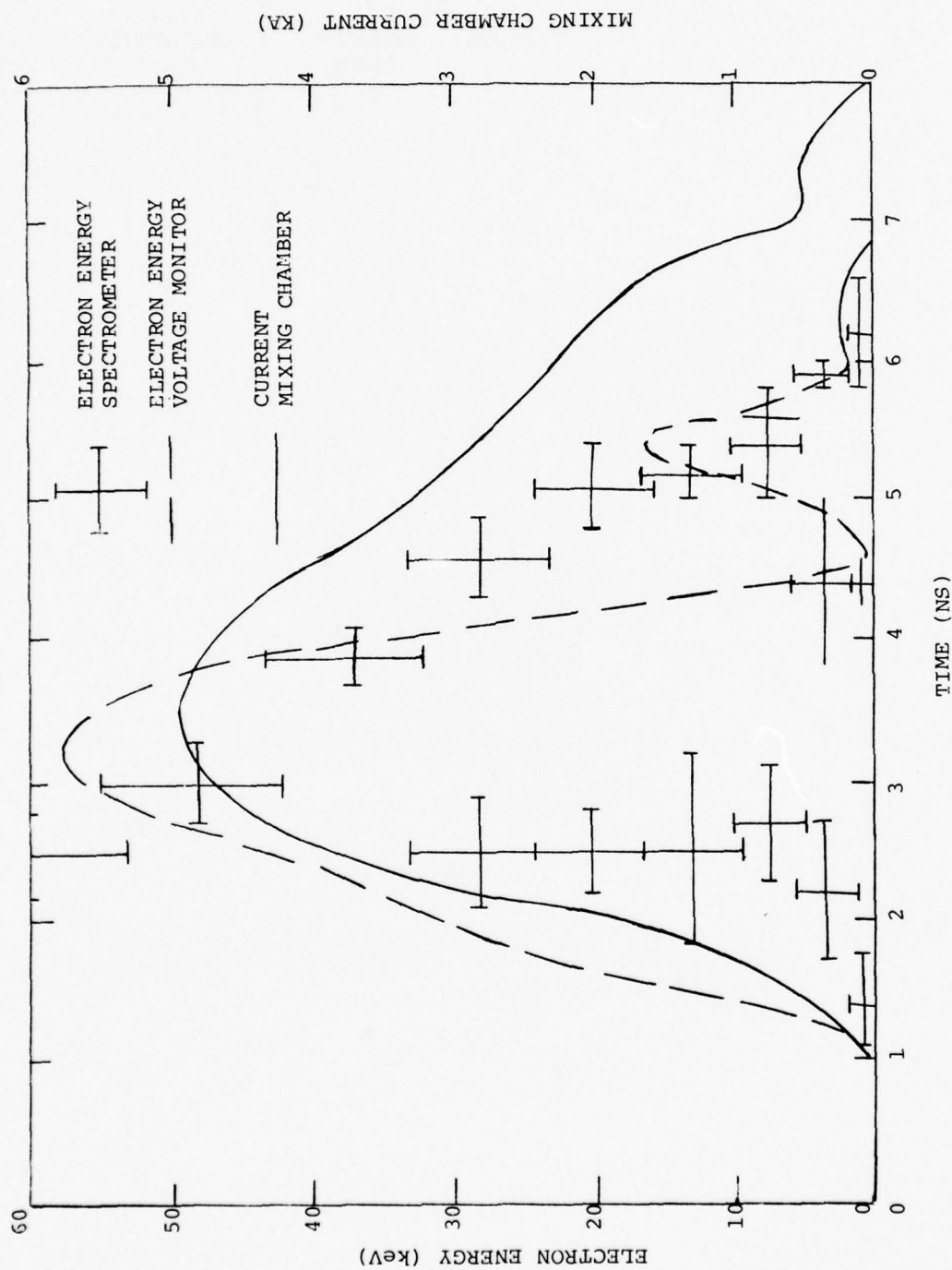


Figure 11. Injected Electron Energy and Current for HDL 12-Inch Diameter Cavity IEMP Benchmark Experiment (average)

Delay between signals is determined by measuring the time delay on the film and correcting for cable length differences measured with a TDR.

#### 4.3 REPRESENTATIVE CAVITY PHENOMENOLOGY DATA

Cavity phenomenology can be studied using the electron injection parameters discussed in the previous section. Figure 12 shows peak transmitted current as a function of cavity depth, at a pressure of  $10^{-4}$  torr. For shallow cavities, little space charge limiting occurs. At a depth of about 4 cm, the space charge barrier is essentially complete. As cavity depth ( $d$ ) is further increased, the transmitted current falls approximately as  $1/d^2$ .

Cavity pressure can then be varied from  $10^{-4}$  torr up to the point at which the Mylar window ruptures, about 10 torr. Representative cavity pressure data is shown in Figure 13 for a 35 ns (fwhm) pulse width at 15 cm deep cavity. At low pressures, (less than 10 microns in this case) the air has little effect upon the peak transmitted current. As pressure is further increased in the range from 20 to 70 microns, air ionization results in space charge barrier dissipation and the transmitted current increases rapidly to its peak at 70 microns. Subsequent increases in pressure causes a reduction of transmitted current, due to increased plasma conductivity. The emf associated with the primary electron current risetime causes back-streaming plasma currents which reduce the net transmitted current.

Experiments have been conducted to determine peak transmitted current data versus pressure for a range of injected electron pulse widths from 2 to 80 ns (risetimes proportional). In all cases the peak current was about the same and electron spectra were comparable. The pressure at

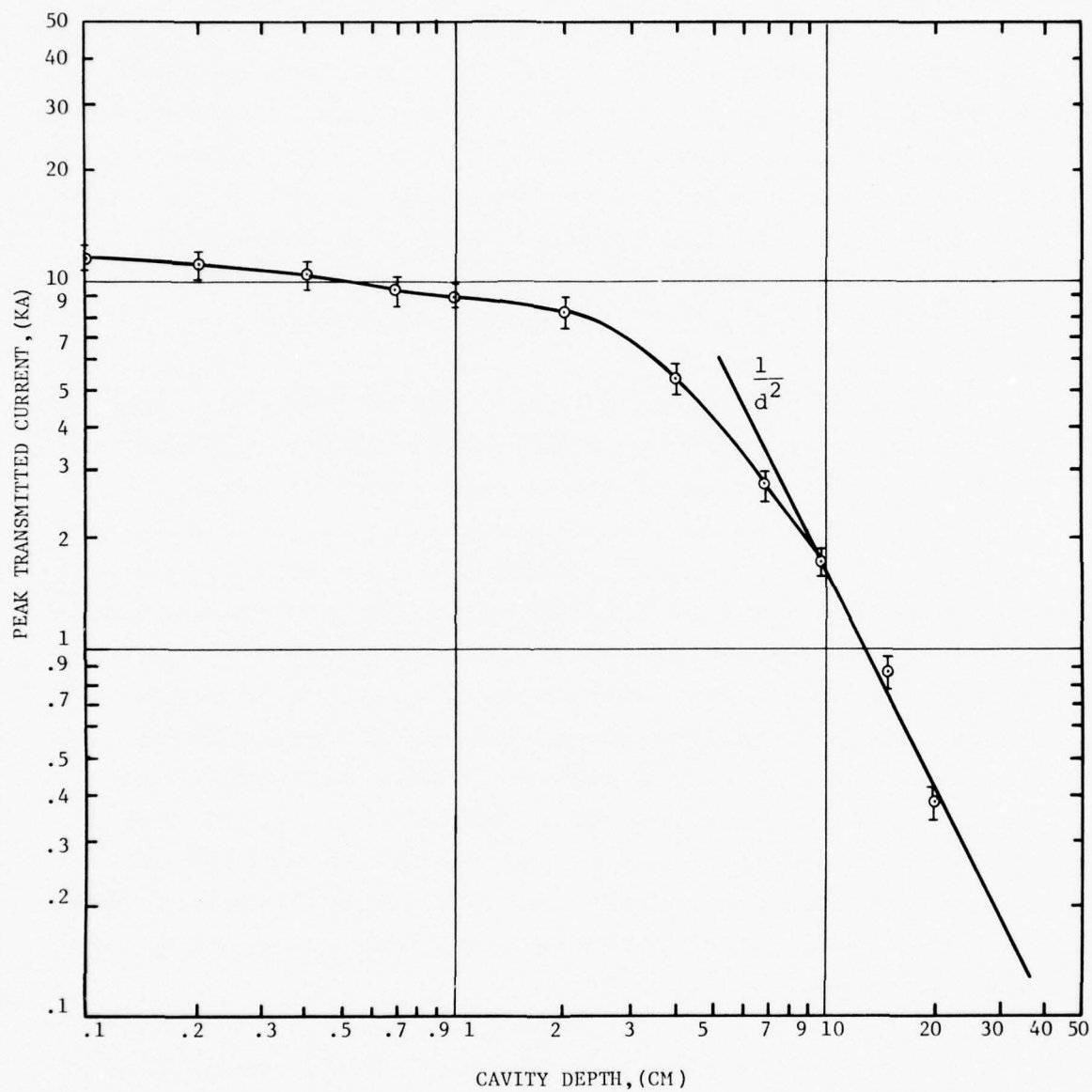


Figure 12. Peak Transmitted Current vs. Cavity Depth at  $10^{-4}$  Torr for 12-Inch Diameter Cavity IEMP Experiments



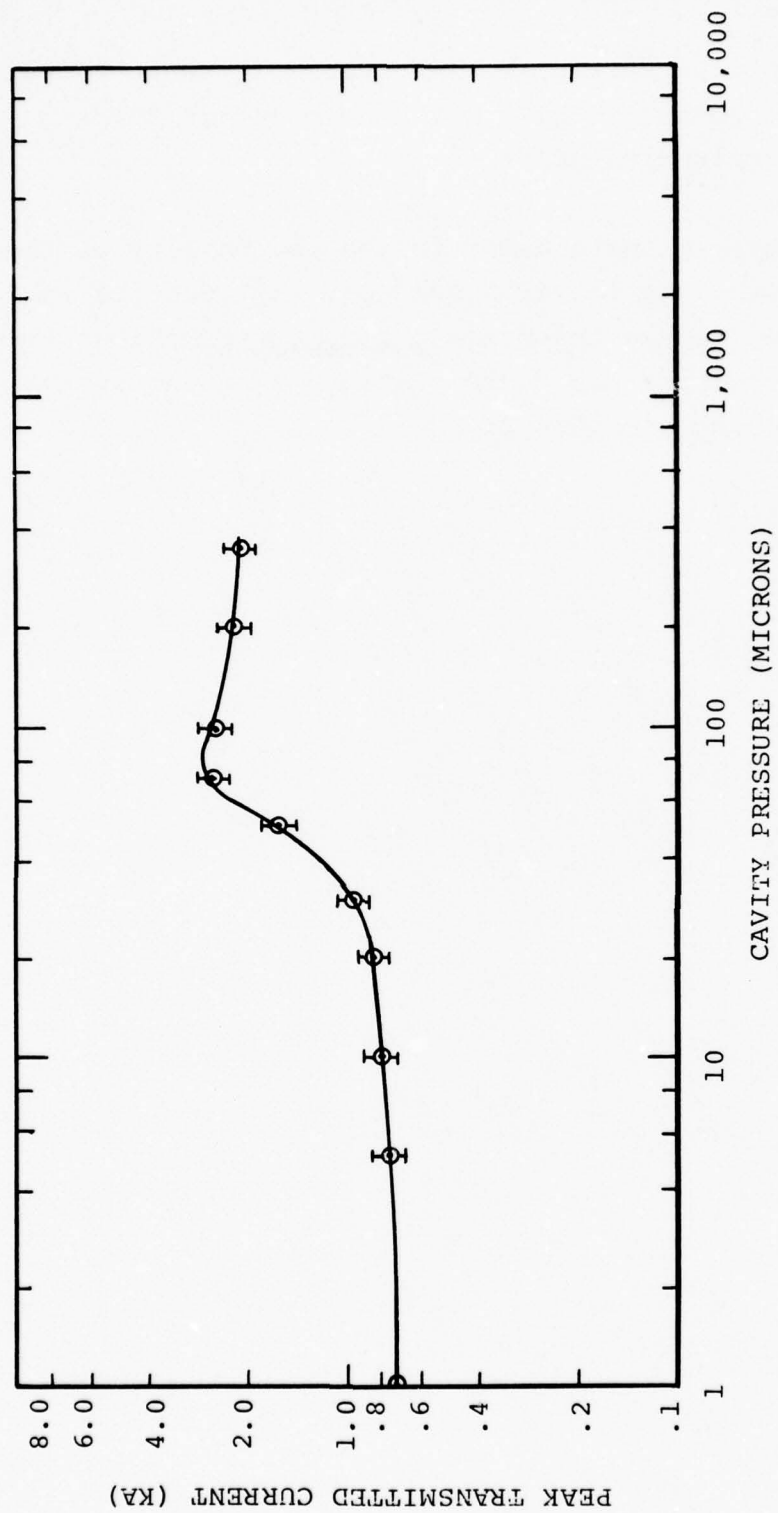


Figure 13. Peak Transmitted Current vs. Cavity Pressure at 15 cm Depth for 12-Inch Diameter Cavity IEMP Experiments ( $t = 35$  ns fwhm)

which space charge neutralization occurs is shown to vary strongly with pulse width as would be expected for a collisional ionization model.

This type of data demonstrates the utility of the simulation technique for IEMP studies. In addition to empty cylinder end-on injections, side-on injections into "cluttered" cavities are contemplated and scaled system geometries can be considered.<sup>9</sup>

## SECTION V

### EXTERNAL SGEMP SIMULATION

#### 5.1 GENERAL

Low voltage electrons can be applied to SGEMP phenomenology studies. The diagram of Figure 14 illustrates an electron beam, SGEMP experiment. Electrons have been injected through a 12.5-inch diameter surface centered on the end of a 6-foot long, 30-inch diameter cylinder as a simulation of photo-electron emission from the cylinder when exposed to X-rays end-on. By keeping the emission pulse width short compared to the two-way transit time for the emitter-tank separation, early current is comparable to that for an isolated cylindrical object in vacuum.

#### 5.2 SGEMP APPARATUS

Figure 14 and the photographs of Figures 15 and 16 show most of the aspects of the apparatus used to perform the experiment. The SPI-PULSE 6000 was extended 6-feet with a 2-ohm solid dielectric line into the center of a 10-foot diameter by 12-foot long vacuum tank. The 14-inch transition chamber which houses the 12-inch emitter attaches to the 8 inch diameter of the 2-ohm machine extension. The extension is expanded in diameter to 30-inches with the addition of a lightweight aluminum shroud. The result is emission from the 12.5-inch diameter window at the center of the 30-inch shroud cylinder end. In addition to establishing the exterior surface of the test object, the shroud also provides a region for

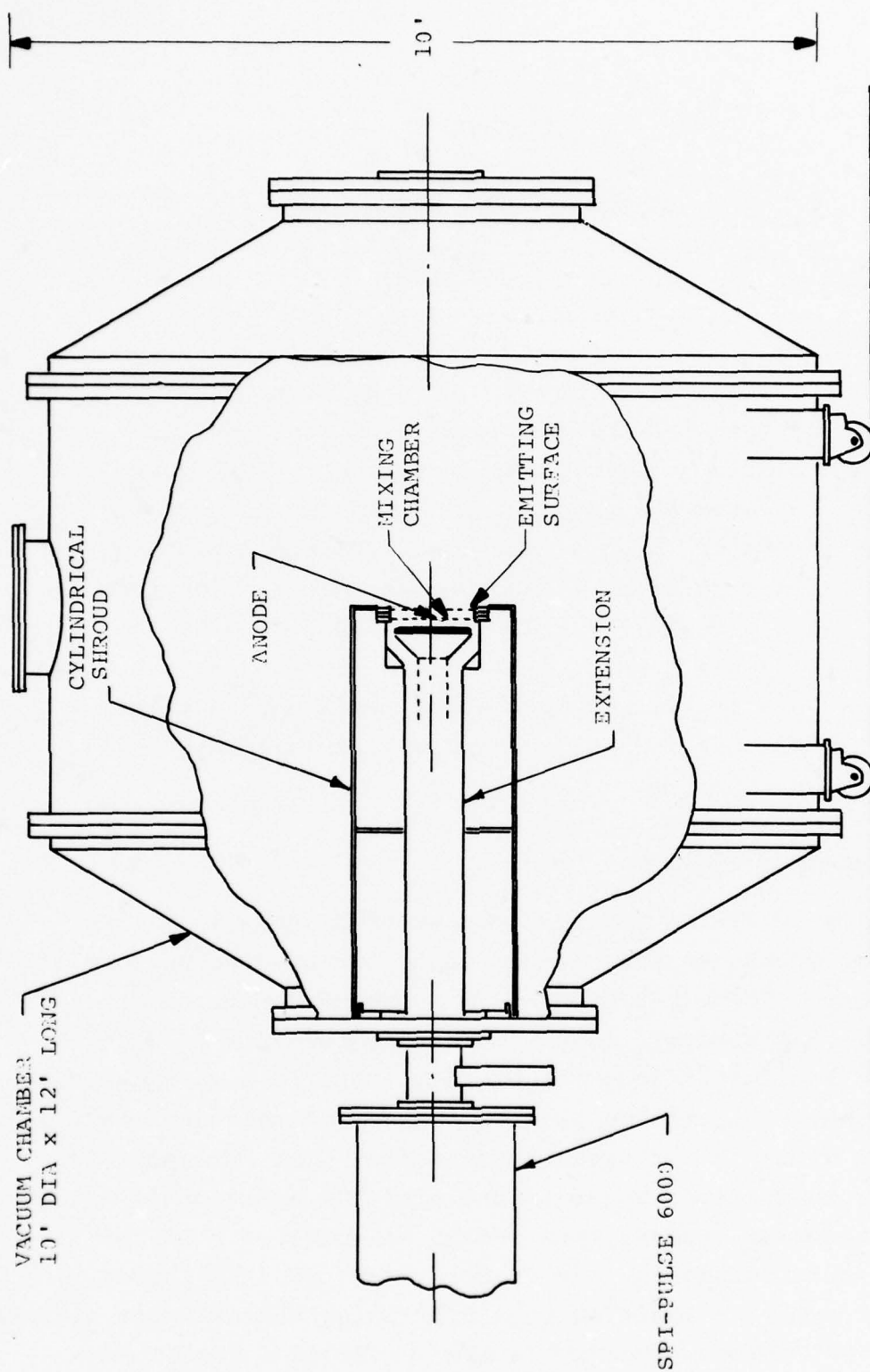


Figure 14. Diagram of Apparatus for SEMP Experiments



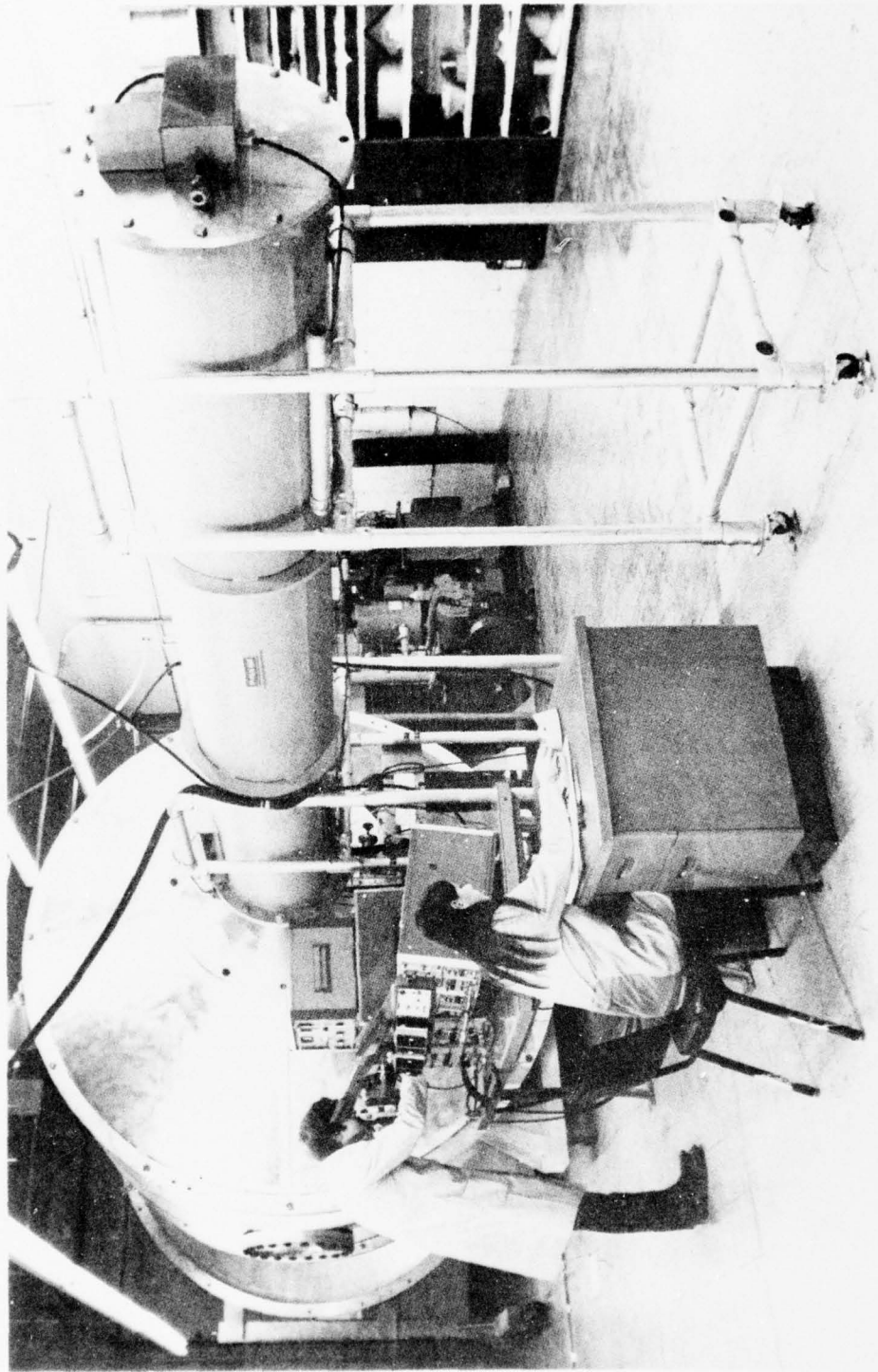


Figure 15. SPI-PULSE 6000 Attached to the SGEMP Vacuum Chamber.

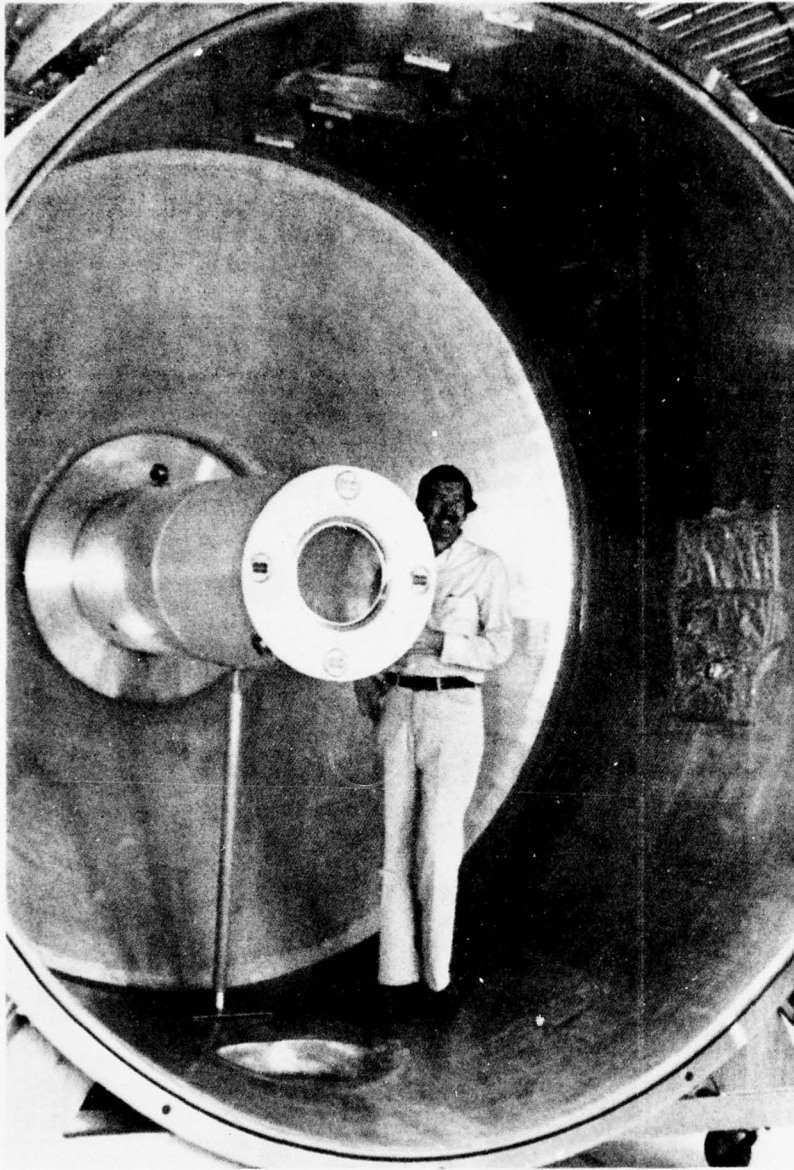


Figure 16. Cylindrical "Emitter" in SGEMP Vacuum System

cabling. This geometry is different from the IEMP experiment previously described in the use of the 6-foot long 2-ohm extension (Figure 14).

Although this shroud is cylindrical to simulate a cylindrical satellite, any shape can be fabricated from light weight aluminum sheet metal. Also, by using intermediate drift regions, other shape objects can be made to "emit" photoelectrons.

### 5.3 EMITTED ELECTRON CHARACTERISTICS

An important requirement for this experiment is that the clear time of the chamber, i.e. the transit time of an electro-magnetic signal from the emitting surface, be greater than the electron pulse width. A 6 ns baseline pulse was therefore chosen.

In order to characterize the electron beam, the same apparatus as that used for the IEMP experiments is used. The 14-inch vacuum chamber containing the 12-inch diameter IEMP cavity with diagnostics is attached directly to the extended diode/mixing chamber configuration.

The emitted current pulse of Figure 17 shows a 6 ns baseline and a 3 ns fwhm with a peak current of about 4 kA. The current amplitude is lower than that obtained in the IEMP study. This is a result of losses associated with energy transfer through the extension. The voltage pulse also shown in Figure 17 was constructed from the time resolved spectral data of Figure 18. The spectral data shown does not include the time correction for time-of-flight differences in the spectrometer.

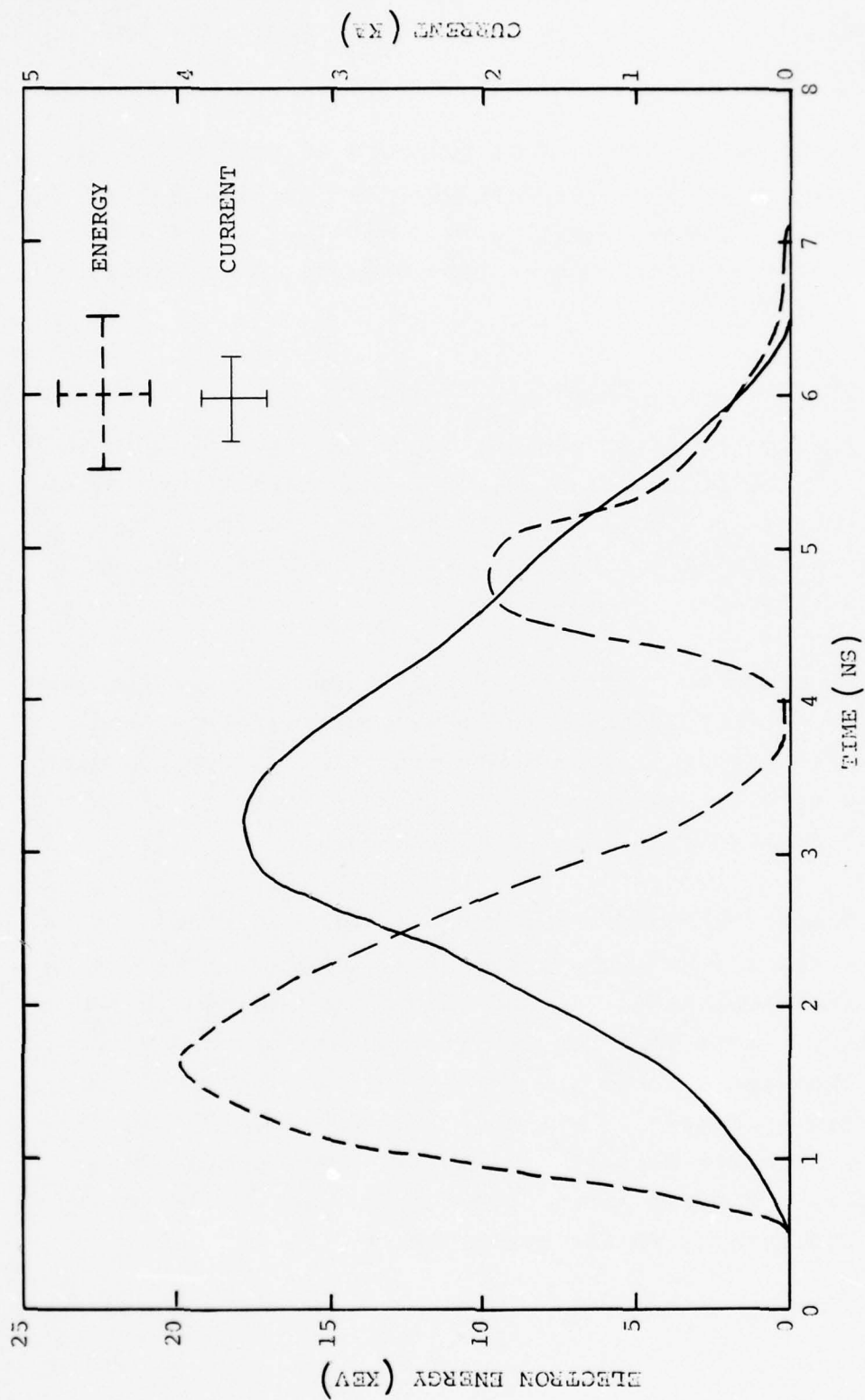


Figure 17. Injected Electron Energy and Current for the SGEMP Experiment



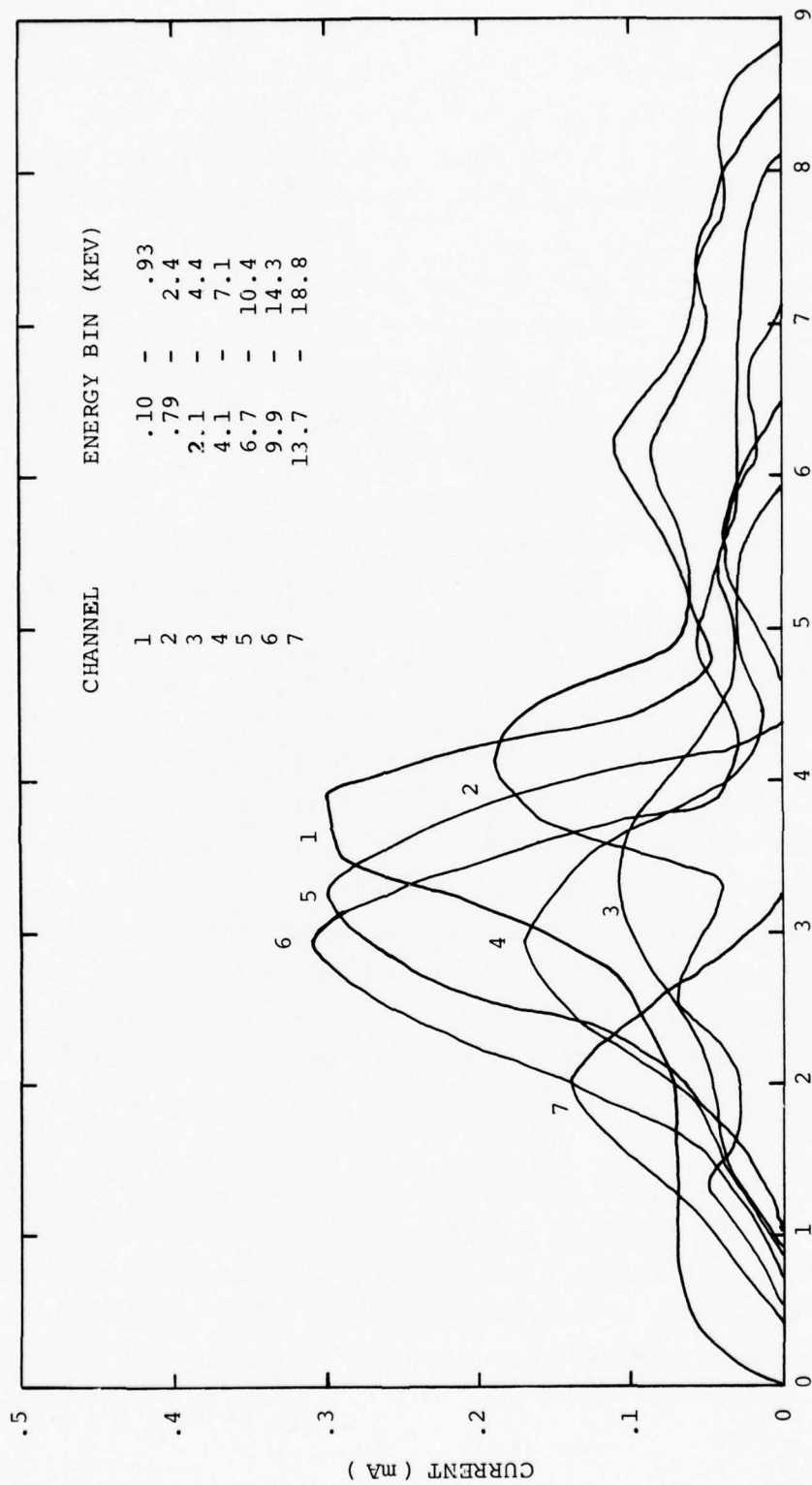


Figure 18. Time Resolved Electron Spectral Data for the SEMP Experiment.

In contrast to previously presented data for the IEMP experiments, the electron energies are much lower for the SGEMP experiment, with a maximum energy of 20keV. A time integrated spectrum for this case is compared to that previously discussed in the IEMP experiment in Figure 19.

Figure 20 shows the emitted current density distribution determined with both radiography and multiple ring Faraday cups. This distribution is more peaked on the beam axis than the IEMP beam density. The peak can be attributed primarily to space-charge expansion of the electron beam.

The angular distribution of the emitted electrons was also determined using radiographic techniques. The distribution of electrons passing through 2 mm diameter holes in a thin aluminum stopping plate at a distance of 7 mm is shown in Figure 21 with an overlay of the experimental geometry. All electrons fall within a  $30^\circ$  cone angle and the angle of half intensity is approximately  $15^\circ$ . This agrees reasonably well with a Monte Carlo transport calculation which indicates that electron scatter would fall within a  $25^\circ$  to  $35^\circ$  cone. It is possible, however, that a wider distribution is present containing low energy electrons for which the film is not sensitive (Figure 6). There has been data obtained that indicates that part of the exposure of the film may have been due to X-rays produced in the diode.

Using the 12-inch IEMP cavity, the transmitted current for this particular beam was determined as a function of cavity depth at  $10^{-4}$  torr. The results, shown in Figure 22, demonstrate the rapid space-charge limiting of electrons as would be expected in view of their very low energy. Although

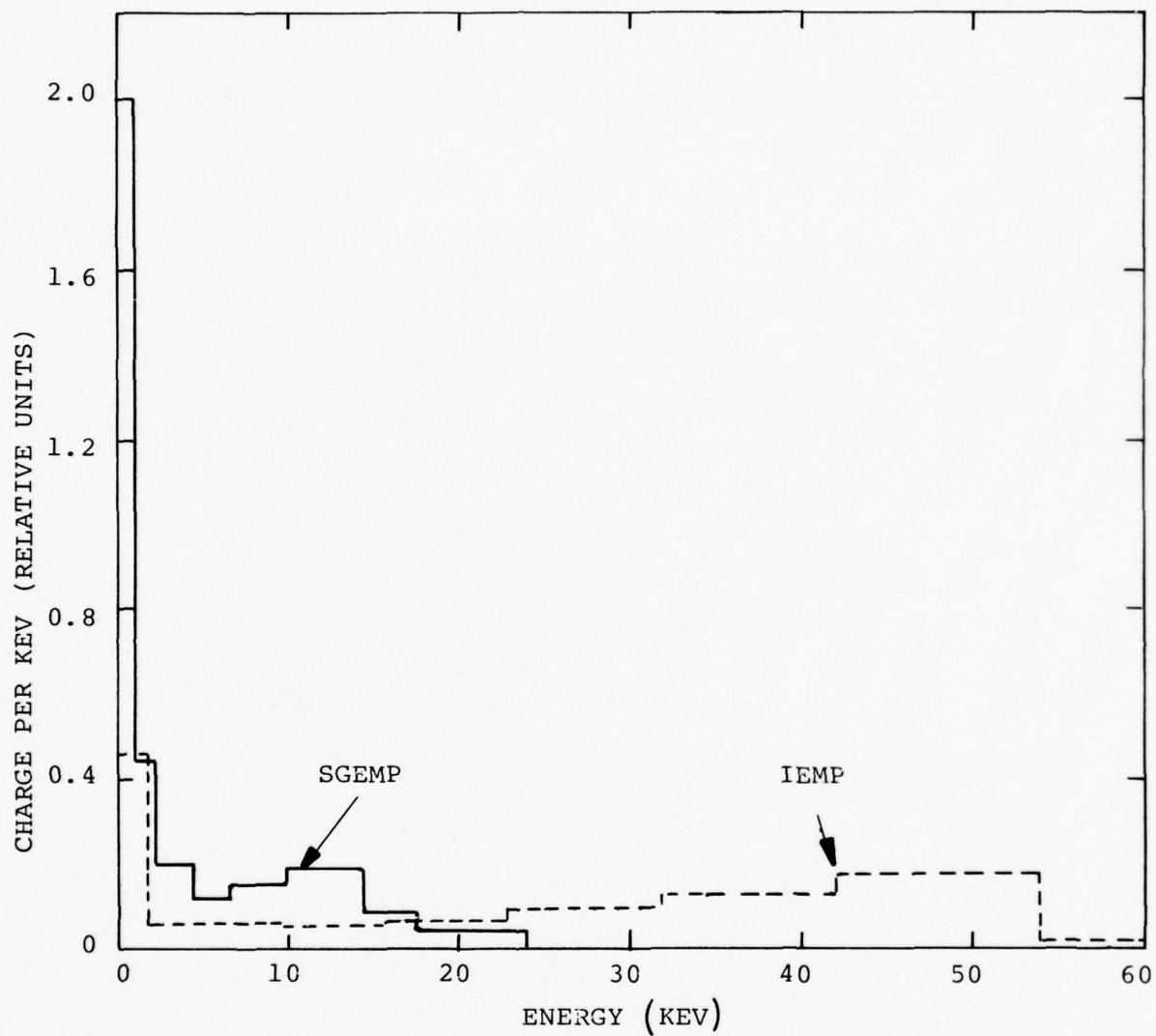


Figure 19. Comparison of Average Time Integrated Spectra for IEMP and SGEMP Configurations

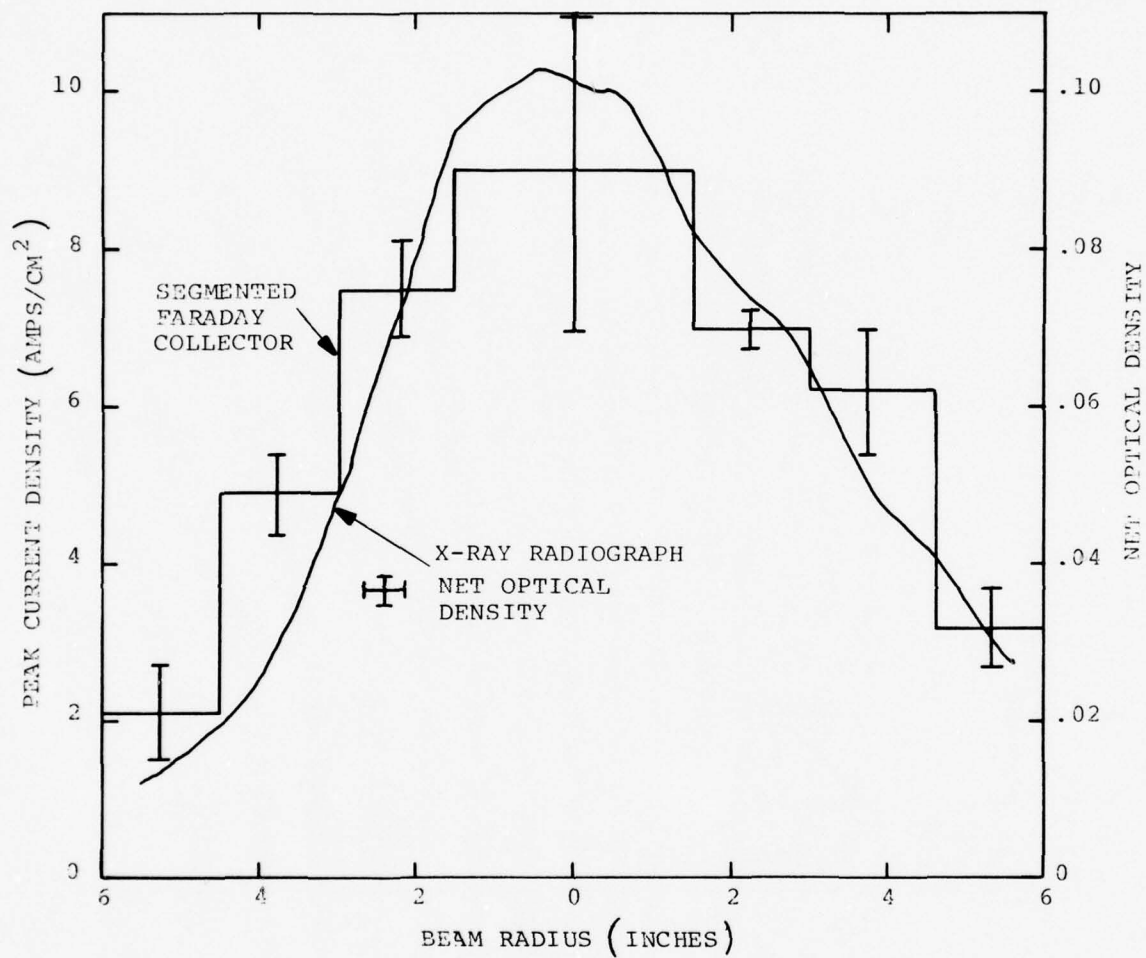


Figure 20. Injected Beam Current Density Distribution From Segmented Faraday Collector and X-Ray Radiograph for 12-Inch SGEMP Experiment



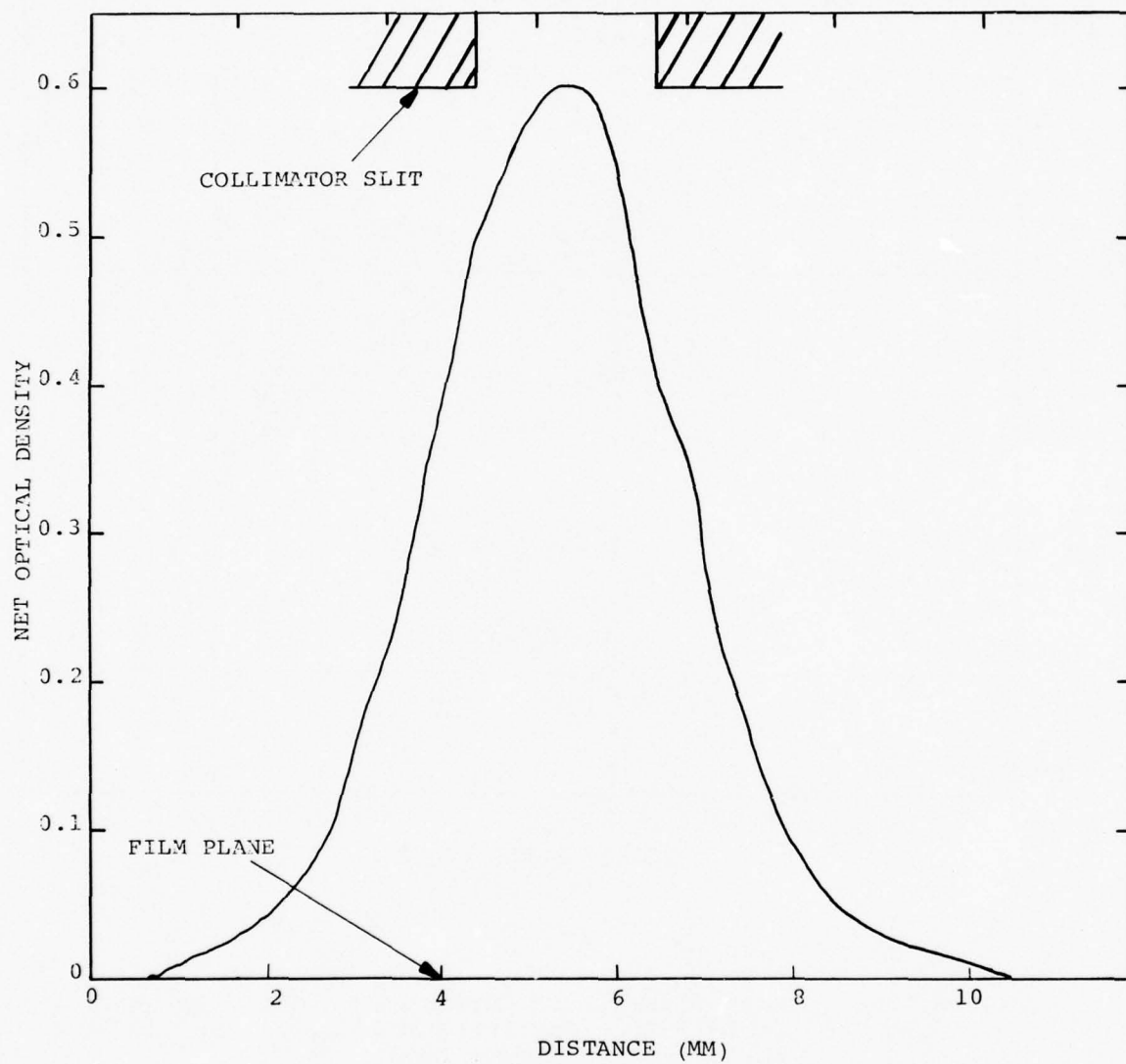


Figure 21. Electron Distribution Determined with Radiographic Techniques for the SGEMP Experiment

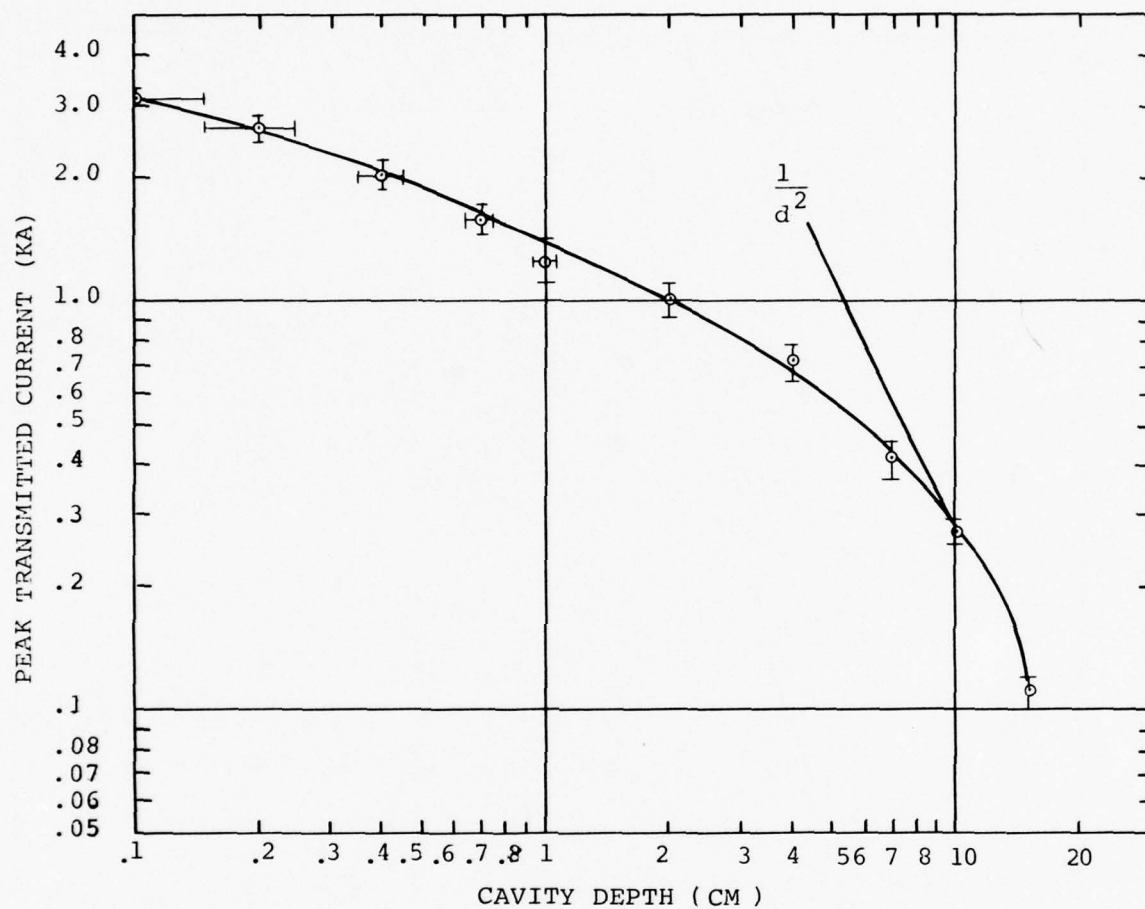


Figure 22.

Peak Transmitted Current vs. Cavity Depth  
at  $10^{-4}$  Torr for the SGEMP Experiment in  
the 12-Inch-Diameter Cavity

in a different geometry, this data indicates that space-charge limiting will be a strong effect in the SGEMP emission case.

#### 5.4 SGEMP EXPERIMENTS

A number of experiments have been performed with the apparatus and electron beam described. These experiments (to be discussed elsewhere<sup>10</sup>) consisted of:

- Check out of AFWL UGT magnetic field sensors.
- Measurement of cylinder surface currents with  $2\pi$  emission and  $\pi$  emission.
- Measurement of surface current with a gap in the cylindrical shroud.

## SECTION VI

### CONCEPTS FOR OTHER IEMP/SGEMP EXPERIMENTS

#### 6.1 GENERAL

The experiments that have been described are perhaps the simplest application of pulsed low voltage electron beams to both IEMP and SGEMP simulation and have demonstrated the utility of these techniques. Based upon this demonstration and the available apparatus, it is meaningful to consider other, and in some cases, more complex experiments. Many of the experimental concepts to be described have resulted from discussions with HDL, IRT, KSC, S<sup>3</sup>, and SAI.

#### 6.2 IEMP EXPERIMENTS

##### Variable Electron Parameters

A wide range of pulse widths, electron spectra and current densities can be injected end-on into the 12-inch IEMP cavity. The relevance of pulse length (tactical versus UGT) to space-charge barrier breakdown can thereby be assessed.

##### Oblique Angle Injection

In addition to end-on injection, side-on injection and even injection at oblique angles can be considered. It should be possible to use mixing chamber type geometries to drift a beam such that it can be injected into an irregularly shaped surface.



### Cluttered Cavities

HDL has planned a series of experiments which involve "cluttered" cavities; such as, cavities which contain cables, diaphragms, and symmetrically and asymmetrically positioned half-discs.

### Dielectric Phenomenology

Some experiments have been performed assessing the effects of the presence of dielectric materials upon cavity IEMP.<sup>3,11</sup> The precise conditions for which dielectric surfaces can provide space charge neutralization have not been identified. Also the effects of dielectric surface transient conductivity upon cavity electric field distributions are yet to be assessed.<sup>12</sup>

### Larger Cavities

With the availability of 3-foot and 10-foot diameter vacuum chambers, missile size cavity IEMP experiments can be considered. Experiments have been performed which indicate that 1 meter diameter cathodes can be made to emit uniformly to achieve such scale-ups.

## 6.3 SGEMP EXPERIMENTS

### Variable Electron Parameters

"Cluttered" type geometries, (e.g. cables attached to the emitting structure) can be evaluated. IRT is currently planning experiments of this nature.

### Structure and Emitting Geometries

The geometry of the emitting structure can also be changed easily by changing the shroud. The effects of dielectric windows or separations of skin structure upon surface

currents can then be evaluated. This geometry change can involve not only the shroud structure but the emitting surface itself. Again, as in the IEMP case, the beam can be drifted to and through almost any shaped surface, causing it to emit photoelectrons, Figure 23. The effects of corners and edges can therefore be assessed.

#### Electron Spraying

KSC has performed an analytical evaluation<sup>13</sup> of the utility of spraying electrons upon surfaces to simulate the removal of photo-electrons from a surface exposed to X-rays. The results of the analysis indicate that this could be a valuable technique for inducing relaxation currents and potentials on a body of opposite sign but with the correct power spectrum.

#### 6.4 COMBINED X-RAY AND ELECTRON EXPERIMENTS

A high Z target can be used to convert electron energy to low energy X-rays via bremsstrahlung. X-ray spectra and fluences produced by beams quite comparable to those discussed above are considered in Section VII. These environments have been used for a number of cable response experiments.<sup>14</sup> By use of a partially transmitting high Z anode, X-rays could be produced and electrons injected simultaneously into a cavity containing cabling and electronic circuitry (such as depicted in Figure 24). This configuration would add a TREE capability to the present technology.

#### 6.5 EVALUATION OF SIMULATOR VACUUM CHAMBER CLEAR TIME

A number of analytical studies have been performed to evaluate problems associated with performing an SGEMP experiment in a vacuum tank whose dimensions are small compared to

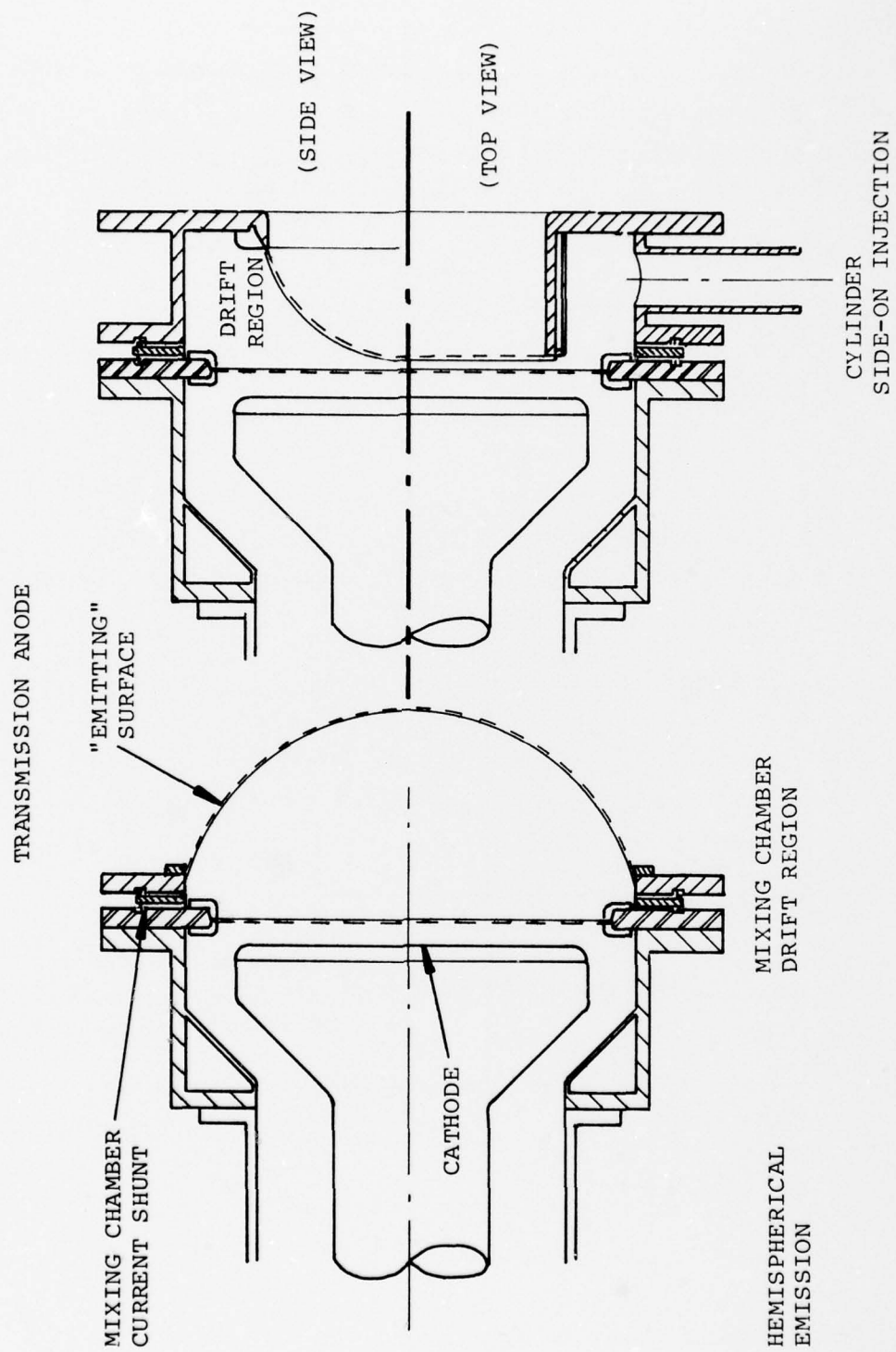


Figure 23. Conceptual Designs for Hemispherical SGEMP Emission and Side-on IEMP Cylinder Injection

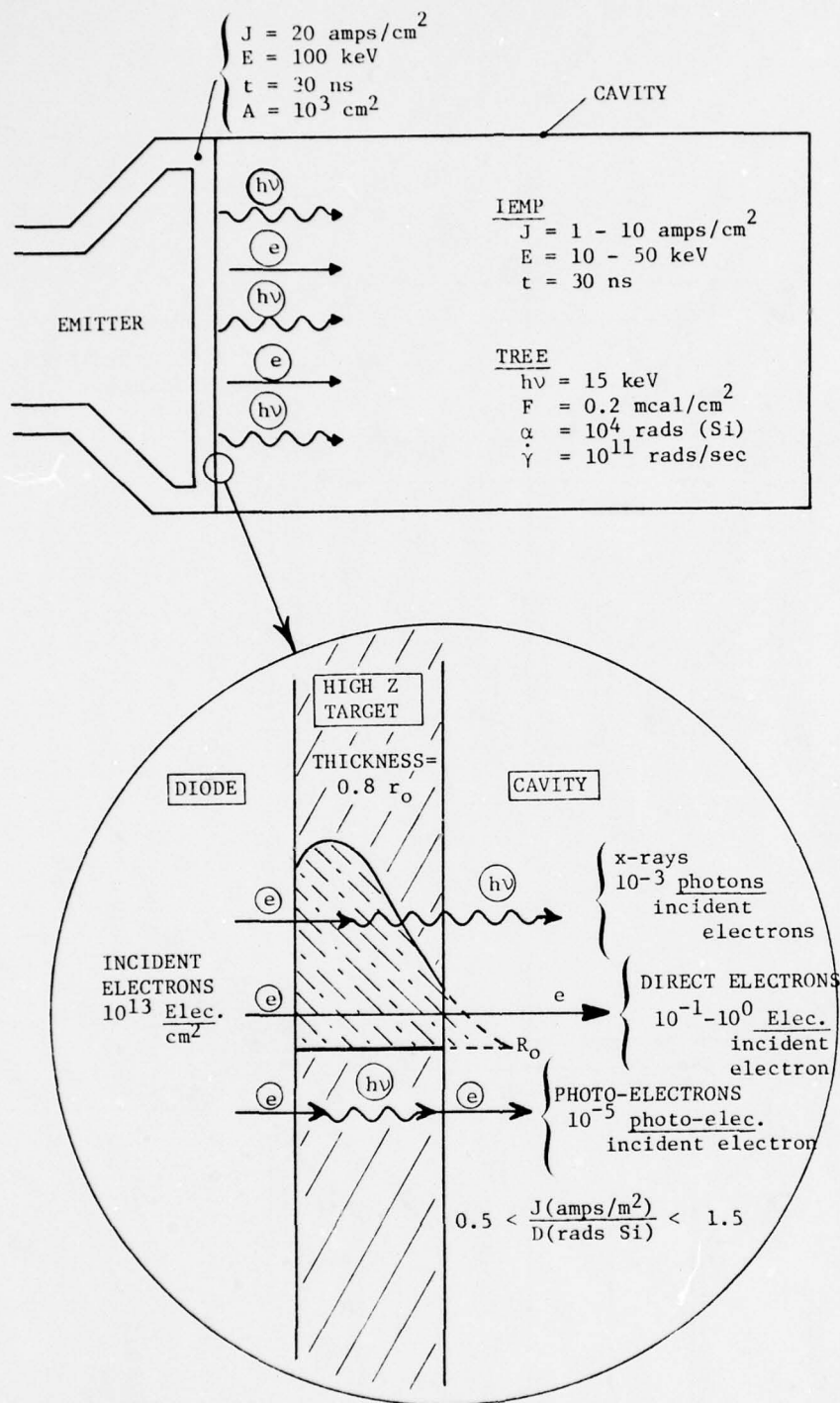


Figure 24. Simultaneous Electron and X-Ray Exposure for TREE Studies.



irradiation pulse width. Considerable interference of the body skin currents and subsequent emission response can be predicted. Little data however, exists to demonstrate these effects!<sup>6</sup>

The 10-foot diameter chamber and an electron beam having a variable pulse width provides an ideal opportunity to study such effects. Skin currents on the cylindrical structure could be measured for electron pulse widths shorter than, equal to, and longer than chamber clear time. In addition, the effectiveness of varying damper designs could be assessed. The conclusions of such studies would have significant economic impact upon the fabrication of a full scale SGEMP simulator.

## SECTION VII

### X-RAY CHARACTERIZATION OF SPI-PULSE 6000

#### 7.0 INTRODUCTION

The SPI-PULSE 6000 has been characterized for two X-ray diode configurations. A 2.5-inch diameter high impedance diode is used for small area, high fluence irradiations. A 12-inch diameter low impedance diode is used for large area, lower fluence work. X-ray fluences have been accurately measured using SPI's gold foil X-ray calorimeter described in Section 7.3. The X-ray output time histories have been determined using  $\text{CaF}_2\text{:Mn}$  TLD's with values verified by an absorber foil technique with the calorimeter.

Both sources were optimized for maximum X-ray production with reasonable target lifetime by adjusting the thickness of the tantalum target. In most cases radiation fields were measured for more than one machine charging voltage,  $V_0$ .

#### 7.1 2.5-INCH DIAMETER SOURCE

Figure 25 shows a simplified diagram of the 2.5-inch diameter X-ray diode. A 0.005-inch target ( $\gg$  electron range) is used to insure unlimited lifetime with the high electron fluences. The 0.125-inch aluminum backing plate provides an atmospheric seal allowing irradiation of objects without a vacuum test chamber. Figure 26 presents axial fluence maps for several charging voltages and target thicknesses. Maximum working fluence at the face is approximately  $2 \times 10^{-3} \text{ cal/cm}^2$ . Figure 27 shows a two dimensional map for the configuration producing this fluence.

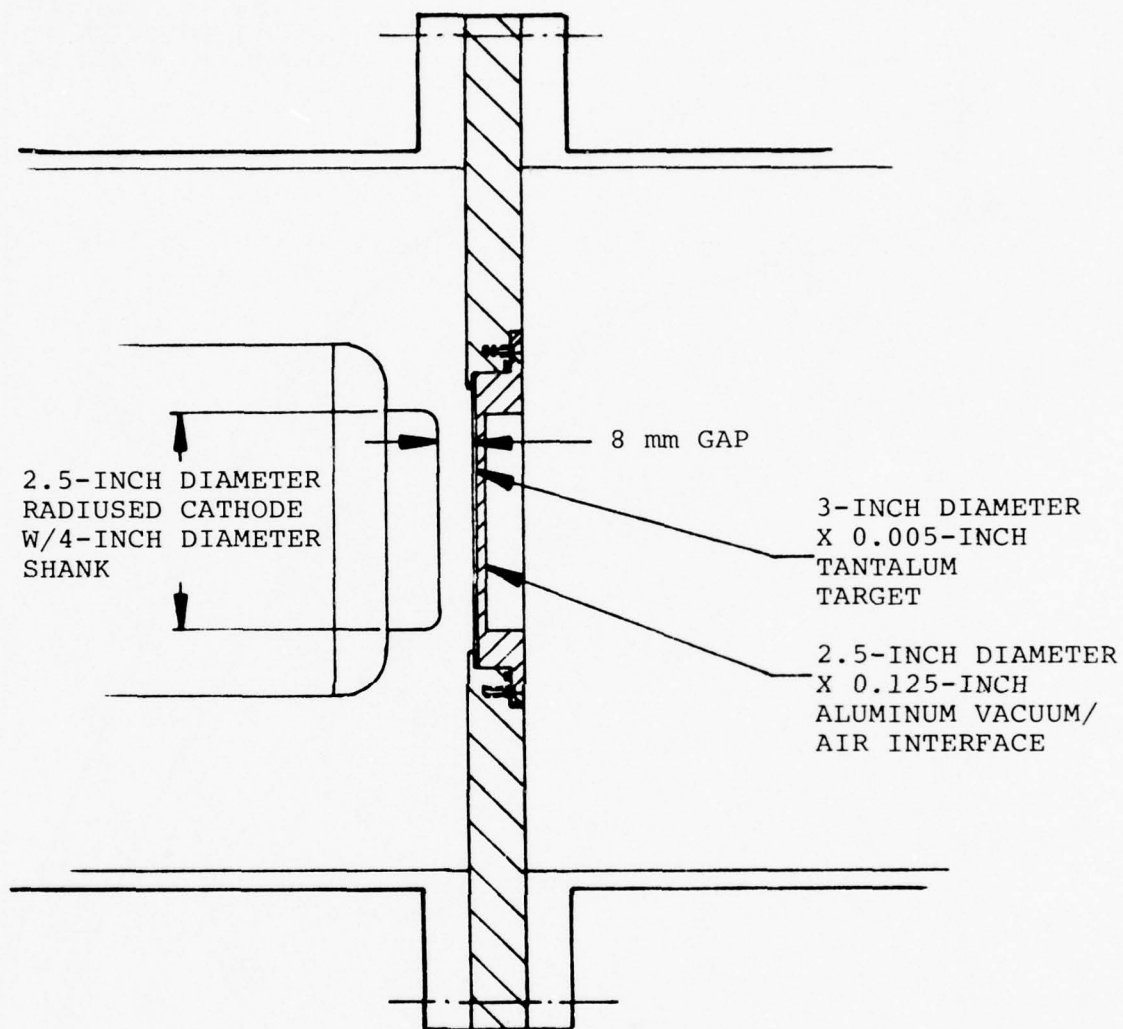


Figure 25. 2.5-INCH DIAMETER X-RAY SOURCE

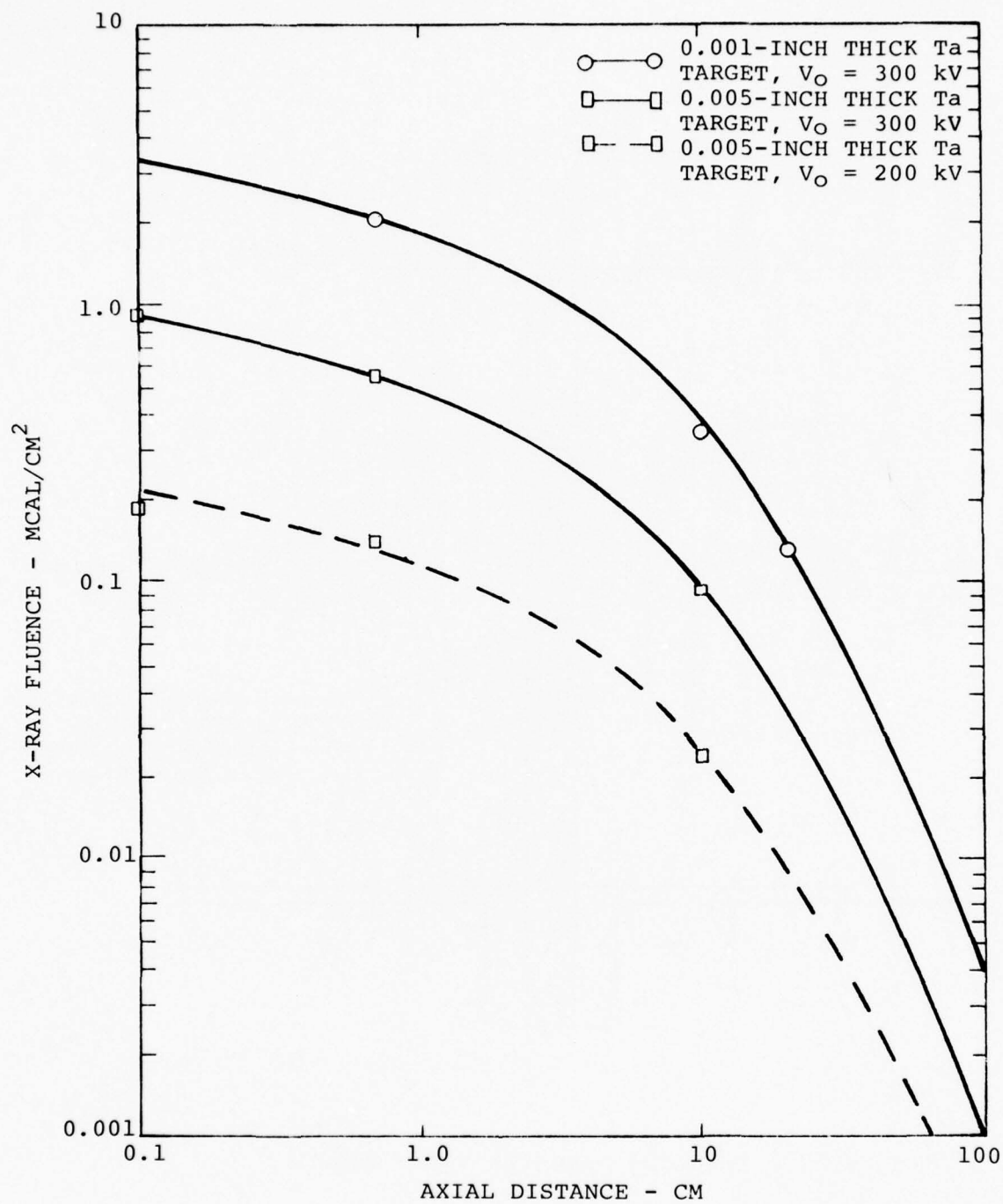


Figure 26. SPI-PULSE 6000 Axial X-ray Fluence Maps for a 2.5 Inch Diameter Ta Converter with a Range of Thickness and Generator Charging Voltages.

Axial dose maps and a corresponding 2D dose map are shown in Figures 28 and 29 respectively. Beyond 20 cm both fluence and, therefore, dose fall off with  $1/R^2$ . A measured coupling coefficient is then 0.05 cal/g per cal/cm<sup>2</sup>. A representative spectrum and time history for this configuration are shown in Figures 30 and 31 respectively.

## 7.2 12-INCH DIAMETER SOURCE

The 12-inch diameter X-ray diode is shown in Figure 32. A thin (< electron range) tantalum foil is held between a special clamping ring and the aluminum electron absorber plate. This configuration has proven to provide the most efficient X-ray production at 0.44%. With the thin anode structure, all sample irradiation must be done in the vacuum test chamber (14-inch diameter x 36-inch long) provided. Target lifetime is unlimited due to the low electron fluence. Axial dose and fluence maps are given in Figures 33 and 34. The maximum working X-ray fluence at the face is  $2 \times 10^{-4}$  cal/cm<sup>2</sup>. Beyond approximately 60 cm the fluence and dose fall off with  $1/R^2$  as shown in Figures 35 and 36. These quantities have been extrapolated to determine the radiation field in the existing 3 meter diameter vacuum test chamber. Figures 37 and 38 show the two dimensional fluence and dose maps respectively. Minimum values in the chamber are approximately  $5 \times 10^{-7}$  cal/cm<sup>2</sup> and  $5 \times 10^{-2}$  rads (Al). A representative spectrum and time history of the bremsstrahlung output are shown in Figures 39 and 40.

## 7.3 X-RAY CALORIMETER

### 7.3.1 Description

The X-ray calorimeter consists of thermally isolated gold absorber foil with a sensitive thermistor circuit to monitor small changes in temperature due to energy deposition.



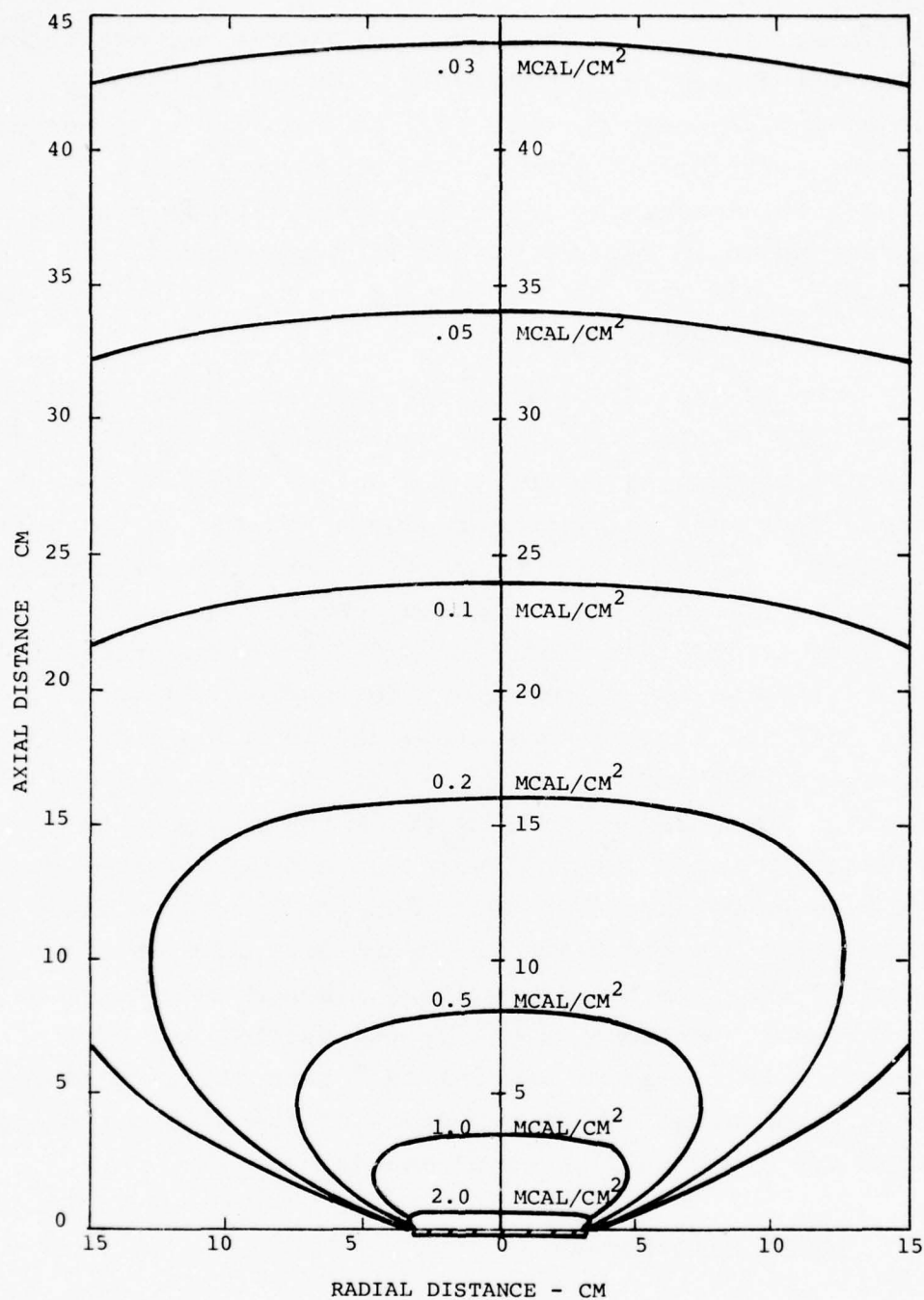


Figure 27. SPI-PULSE 6000 ISO-Fluence Map for a 0.5 Inch Diameter, 0.005-Inch Thick Ta Converter at a Generator Charging Voltage of 300 kV. ( $E_{h\nu} < 200$  keV)

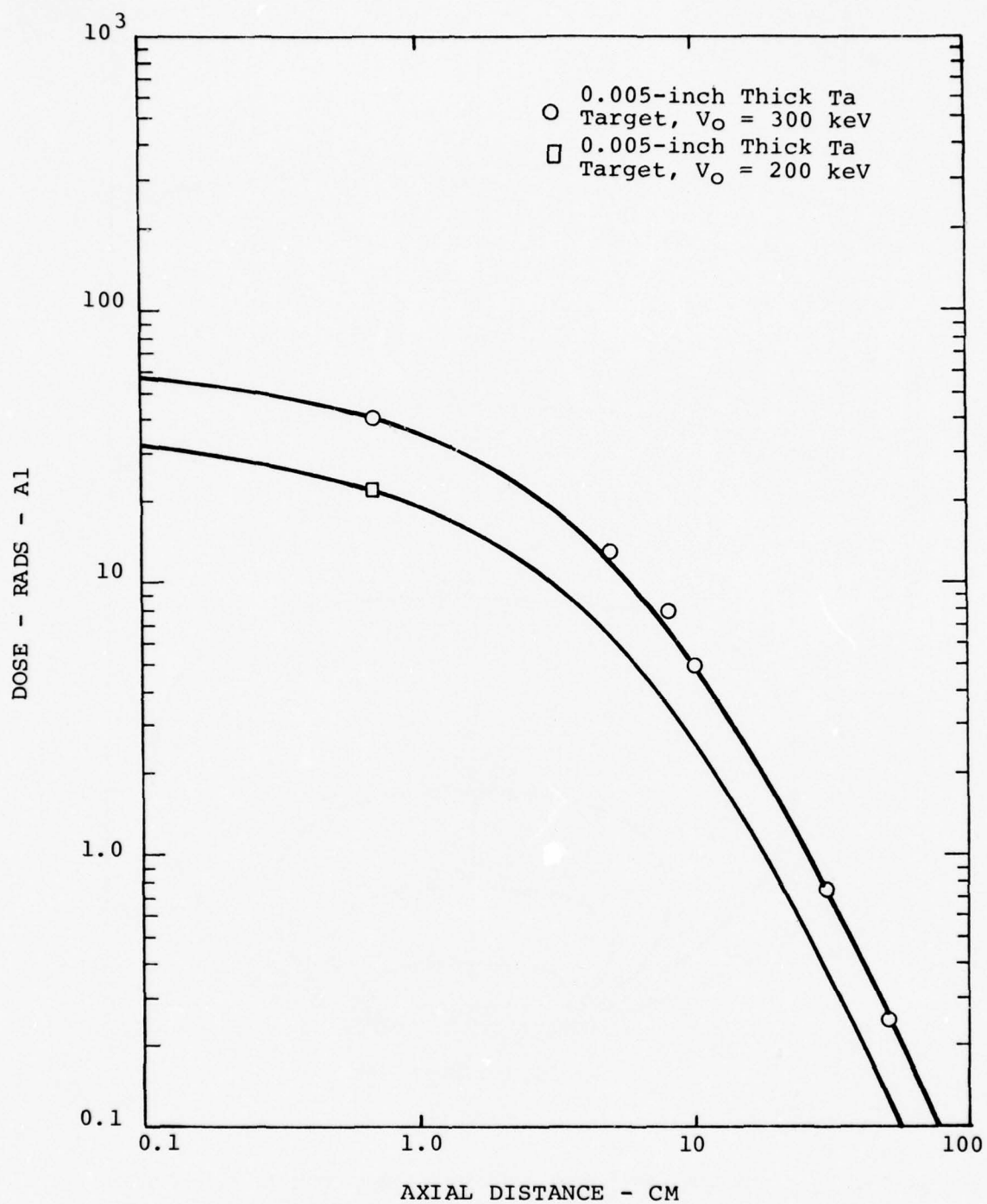


Figure 28. SPI-PULSE 6000 Axial X-ray Dose Map for a 2.5 Inch Diameter, Ta Converter with a Range of Thicknesses and Generator Charging Voltages.

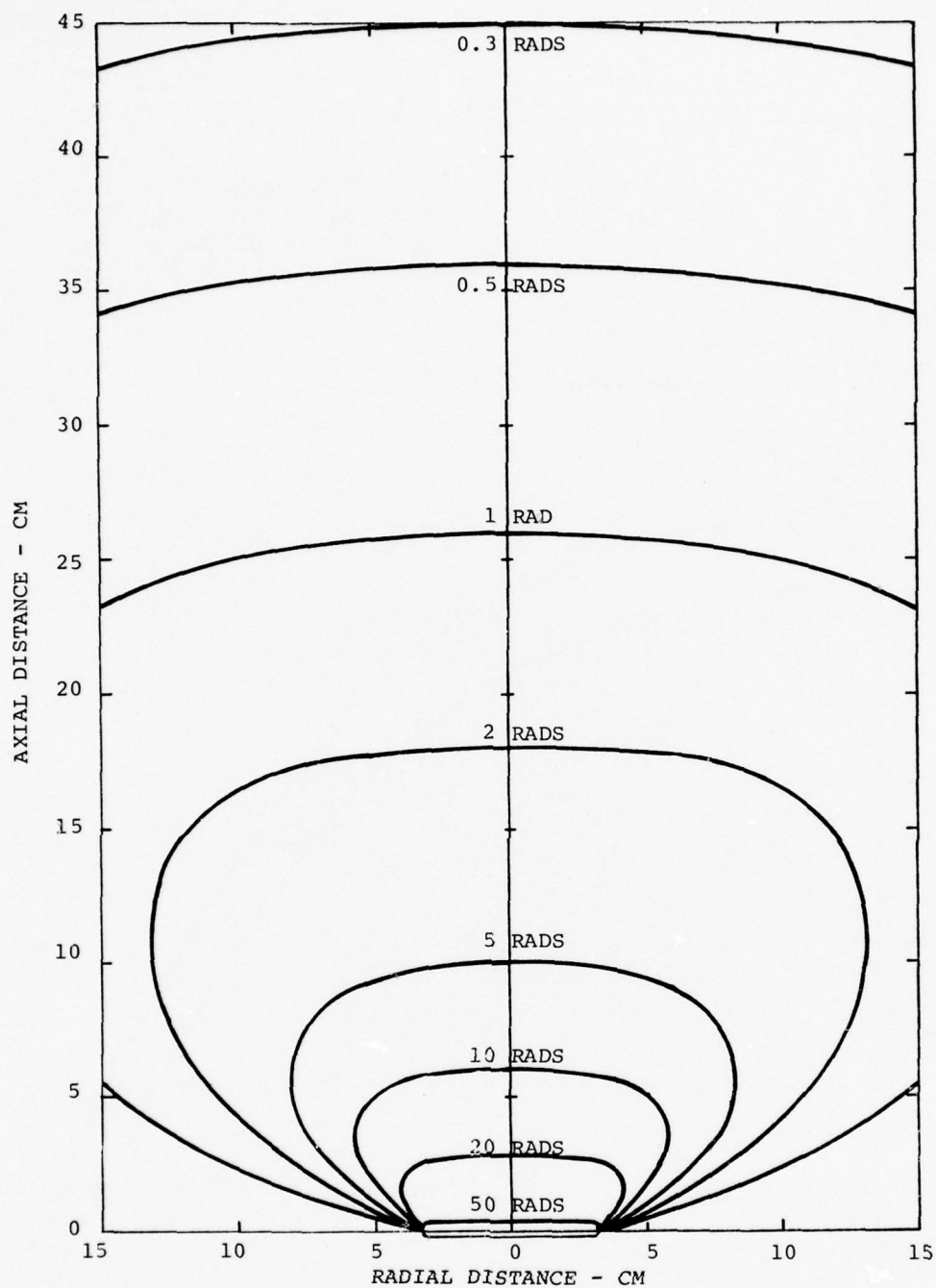


Figure 29. SPI-PULSE 6000 ISO-Dose Map for a 2.5-Inch Diameter, 0.005-Inch Thick, Ta Converter at a Generator Charging Voltage of 300 kV. ( $E_{hv} < 200$  keV)

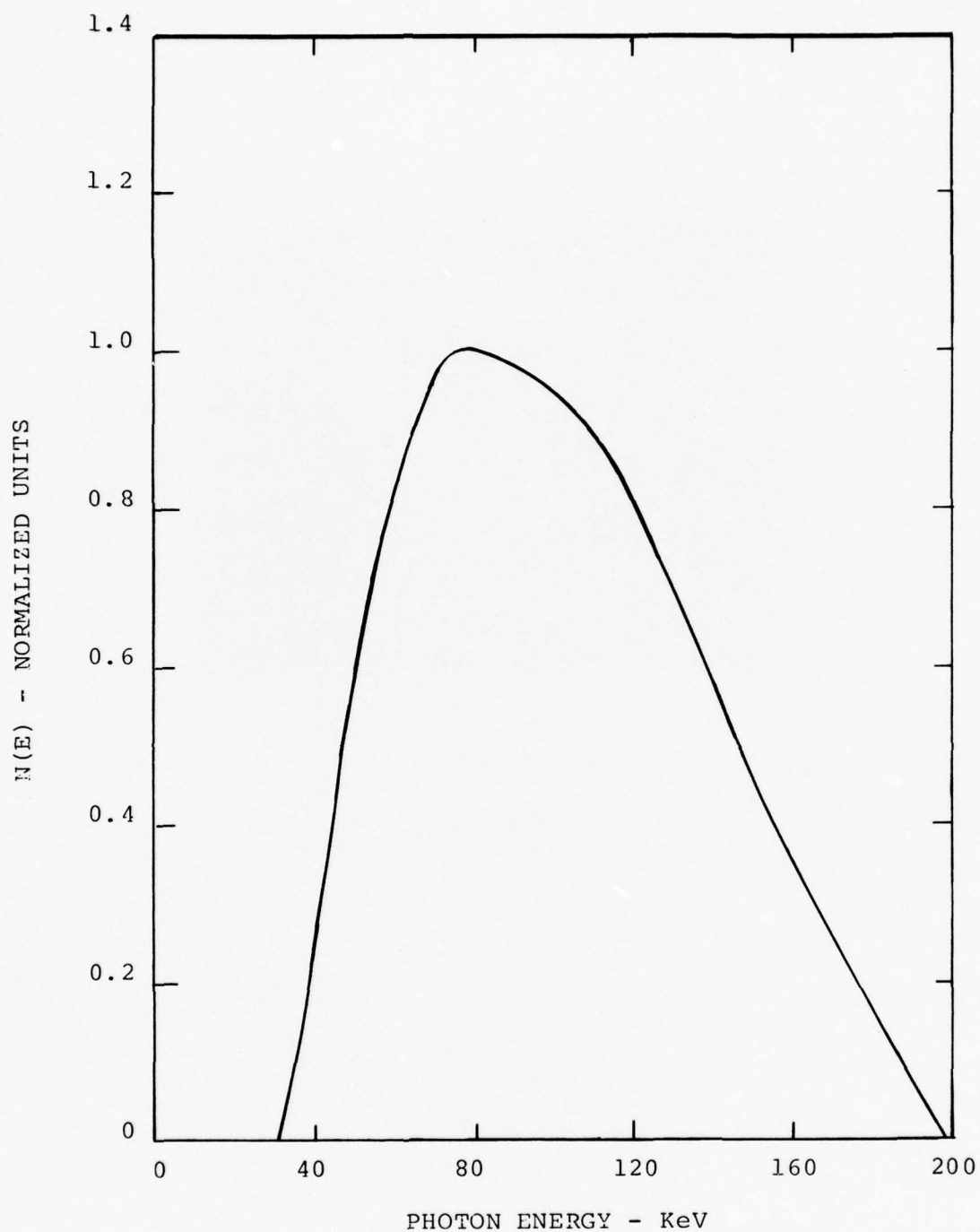
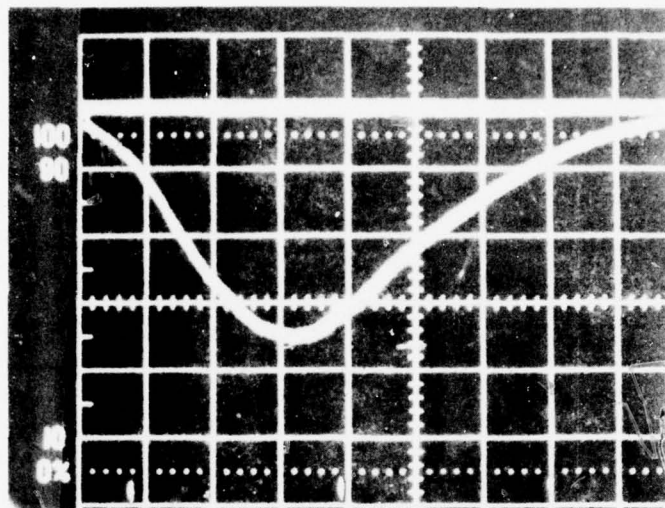


Figure 30. SPI-PULSE 6000 Bremsstrahlung Spectrum for 2.5-Inch Diameter, 0.005-Inch Thick Ta Converter at a Generator Charging Voltage of 300 kV. ( $E_{h\nu} < 200$  keV)



100 mV /  
20 ns / cm

Figure 31. SPI-PULSE 6000 Bremsstrahlung Time History for a 2.5-Inch Diameter, 0.005-Inch Thick Ta Converter at a Generator Charging Voltage of 300 kV.  
( $E_{h\nu} < 200$  keV)



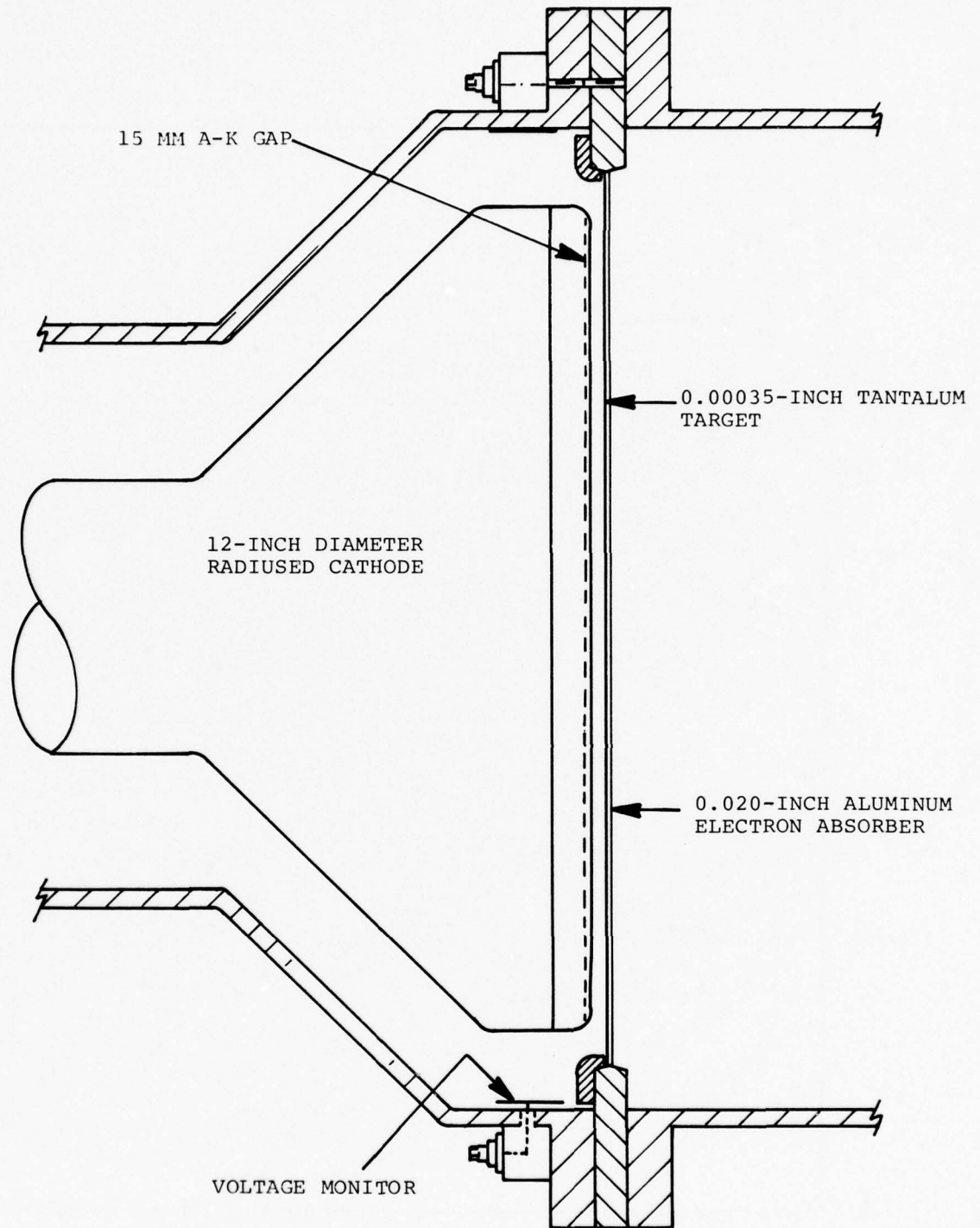


Figure 32. SPI-PULSE 6000 12-Inch Diameter Cathode Configuration for X-ray Production.

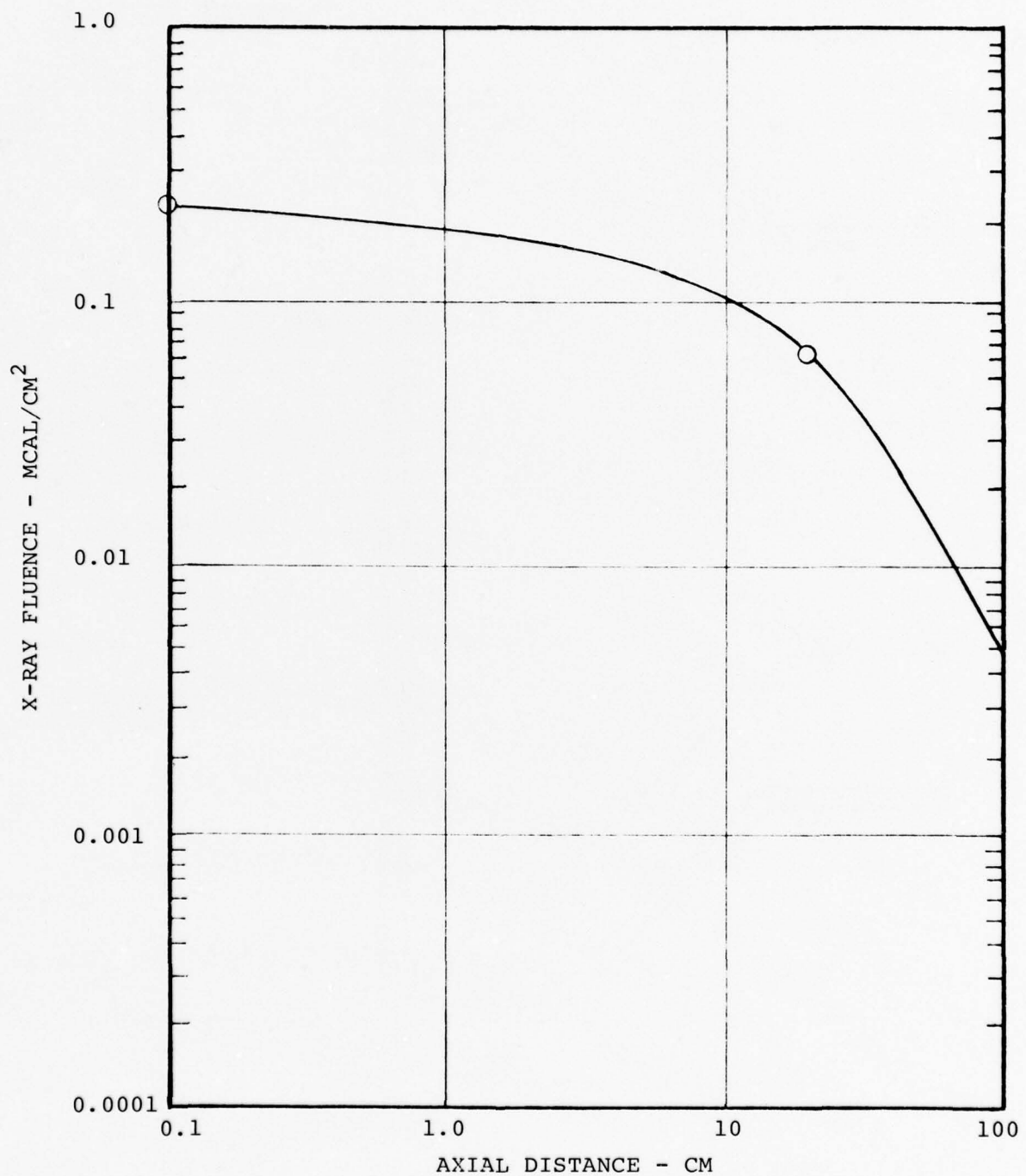


Figure 33. SPI-PULSE 600 Axial X-ray Fluence Map for a 12-Inch Diameter,  $3 \times 10^{-4}$ -Inch Thick Ta Converter at a Generator Charging Voltage of 300 kV. ( $E_{hv} < 120$  keV)

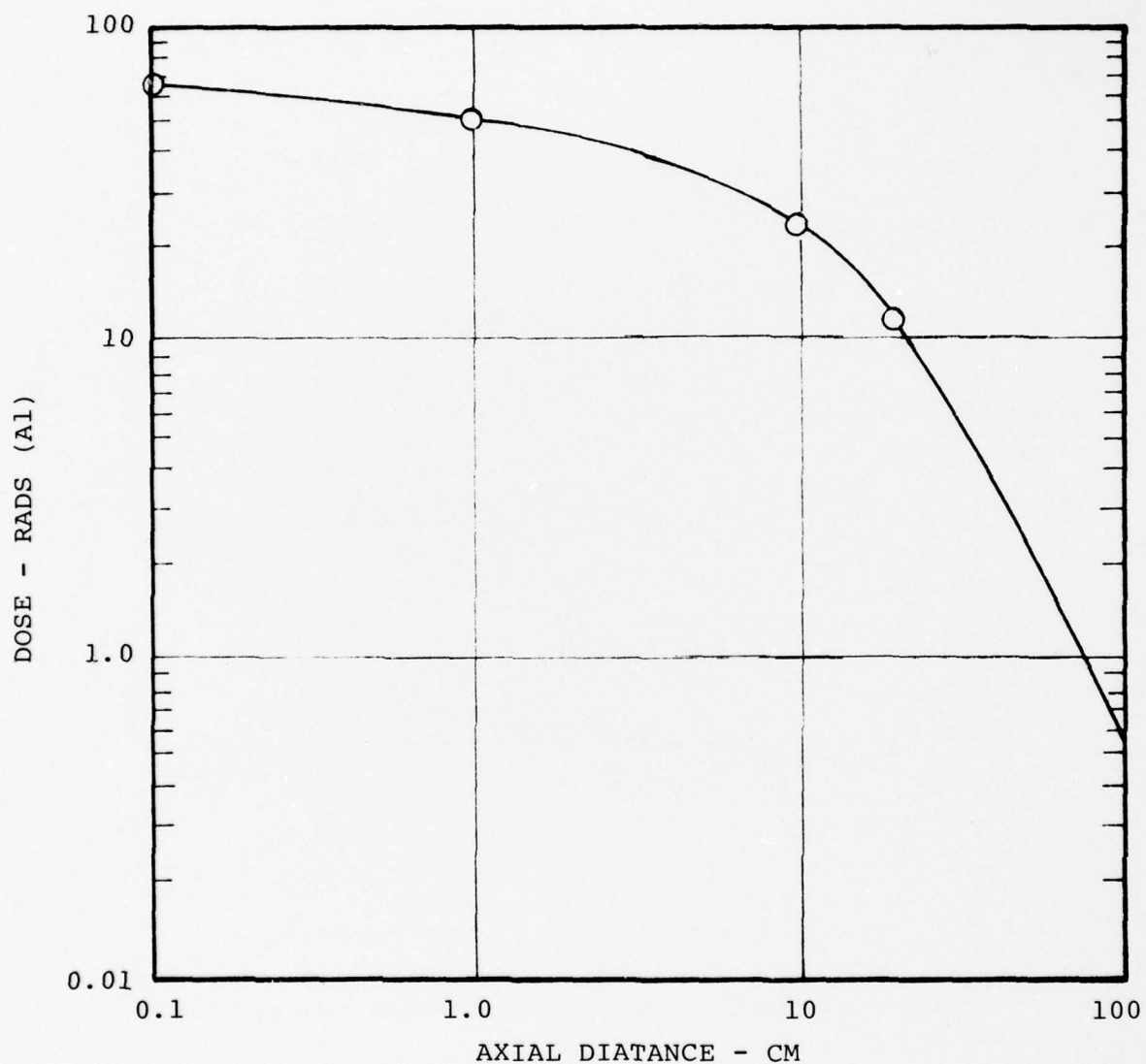


Figure 34. SPI-PULSE 6000 Axial X-ray Dose Map for a 12-Inch Diameter,  $3.5 \times 10^{-4}$ -Inch Thick Ta Converter and a Generator Charging Voltage of 300 kV. ( $E_{h\nu} < 120$  keV)

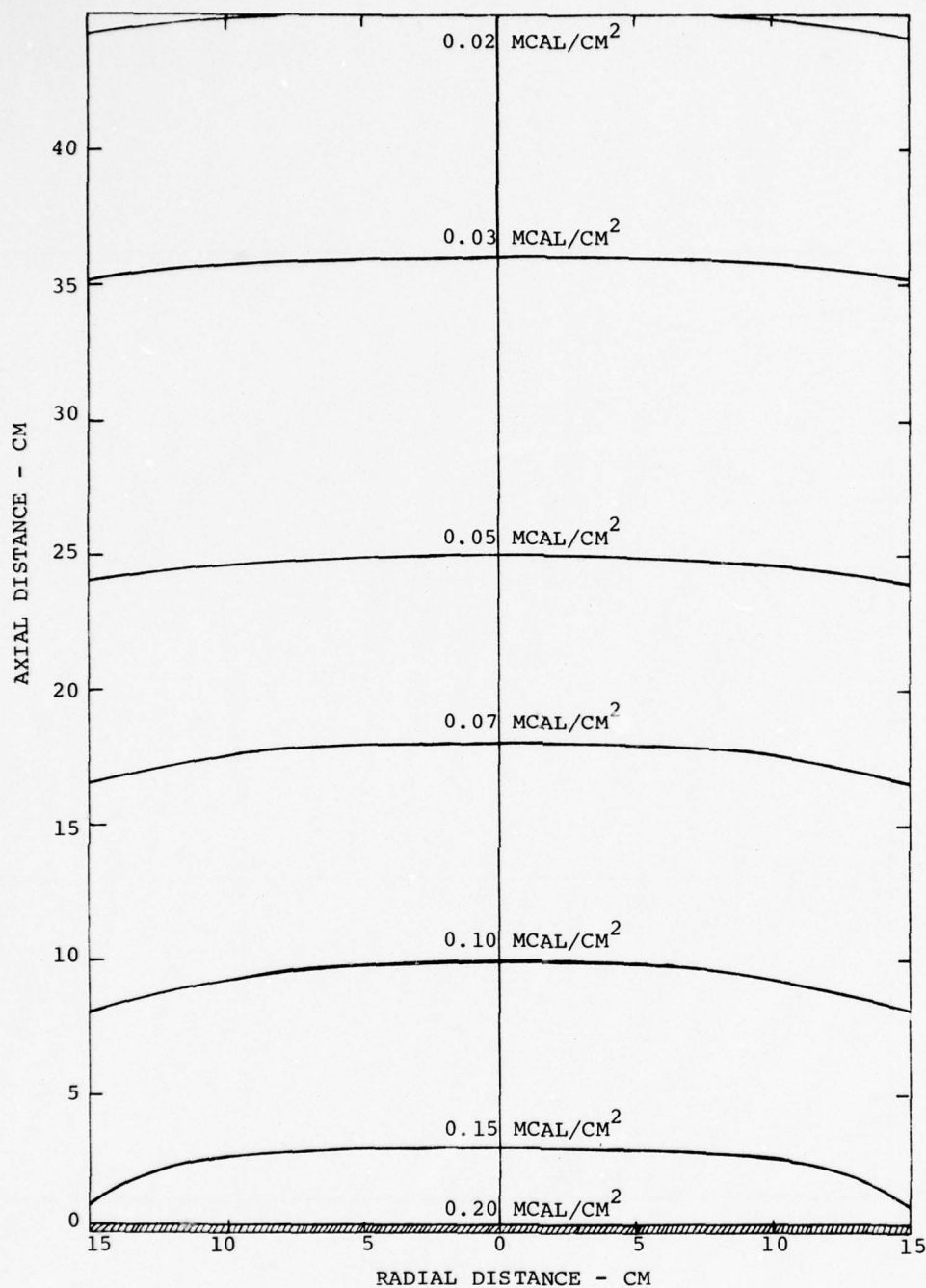


Figure 35. SPI-PULSE 6000 ISO-Fluence Map for a 12-Inch Diameter,  $3.5 \times 10^{-4}$ -Inch Thick Ta Converter at a Generator Charging Voltage of 300 kV. ( $E_{h\nu} < 120$  keV)

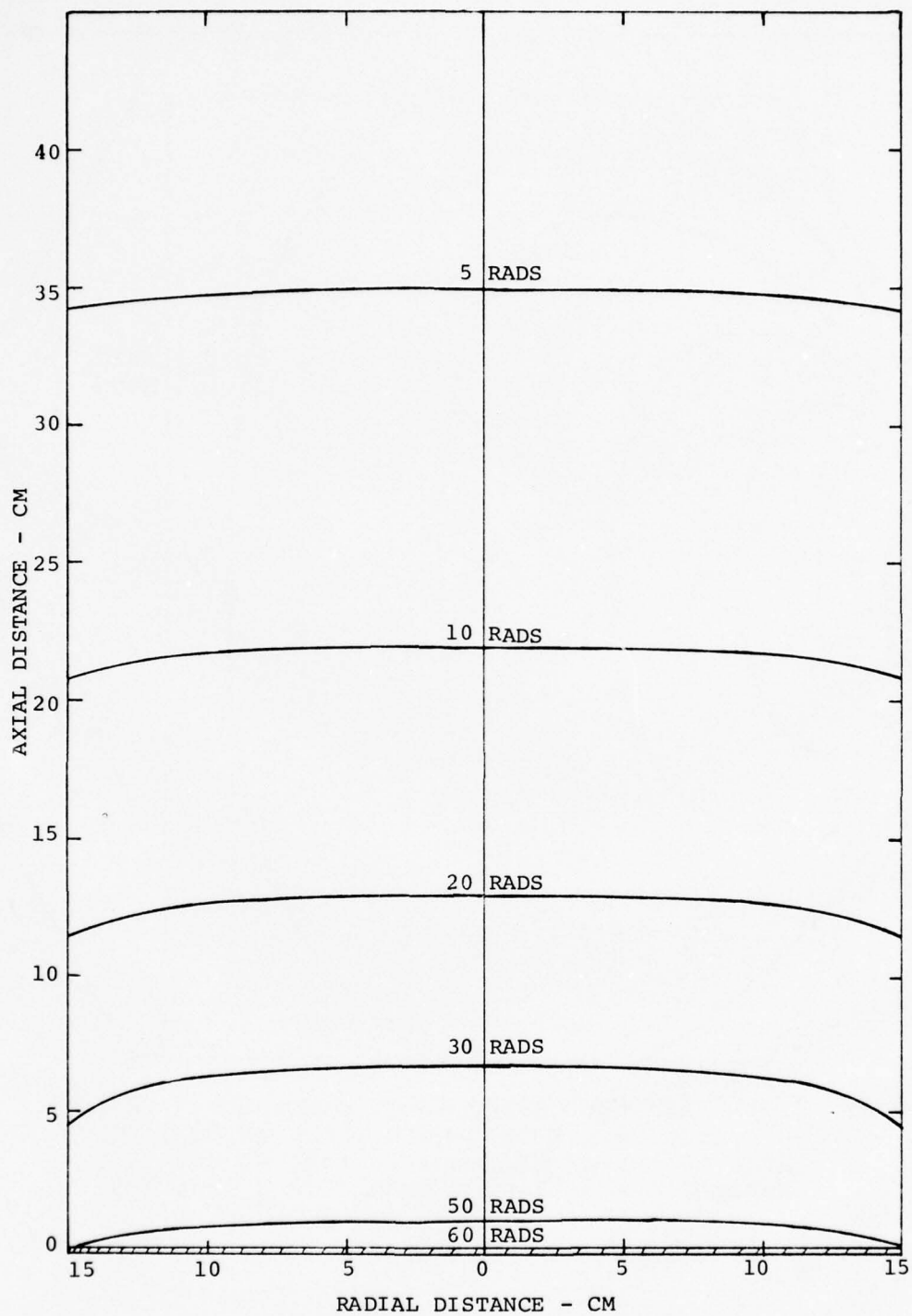


Figure 36. SPI-PULSE 6000 ISO-Dose Map for a 12-Inch Diameter  $3.5 \times 10^{-4}$ -Inch Thick Ta Converter at a Generator Charging Voltage of 300 kV. ( $E_{hv} < 120$  keV)



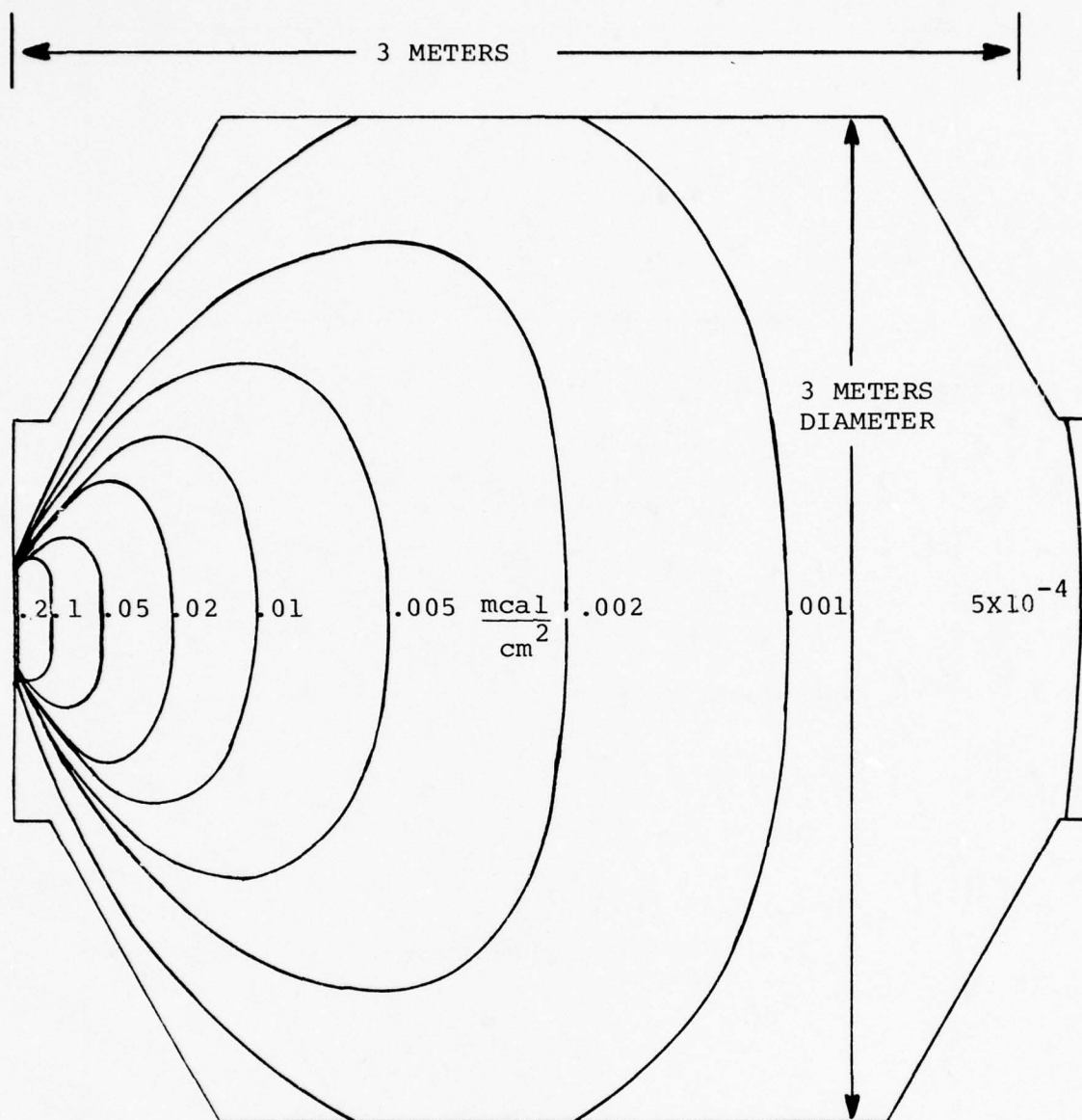


Figure 37. SPI-PULSE 6000 X-ray ISO-Fluence for a 12-Inch Diameter,  $3.5 \times 10^{-4}$ -Inch Thick Ta Converter at a Generator Charging Voltage of 300 kV in 3 Meter Diameter Vacuum Tank. ( $E_{hv} < 120 \text{ keV}$ )

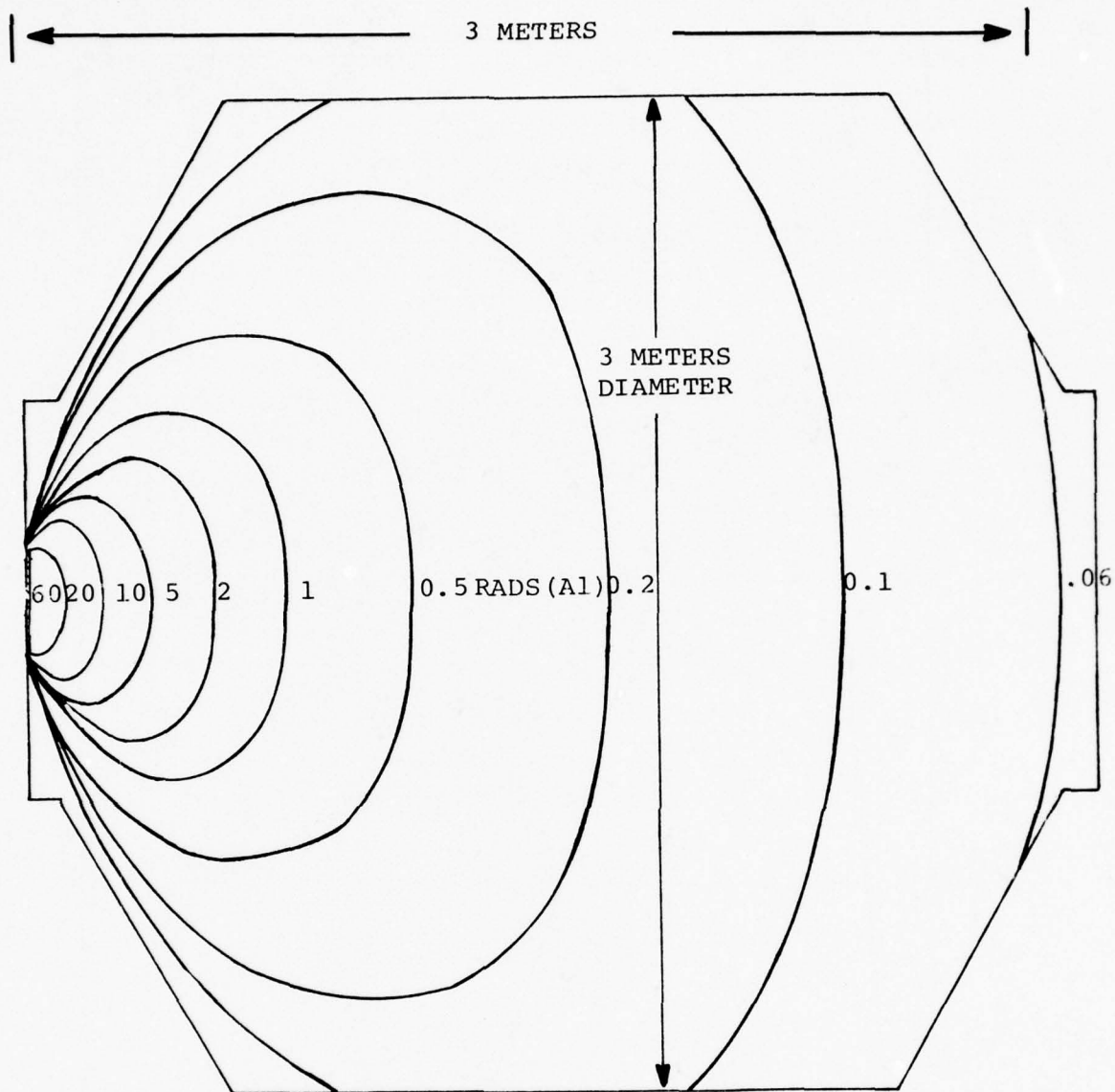


Figure 38. SPI-PULSE 6000 X-ray ISO-Dose Map for a 12-Inch Diameter,  $3.5 \times 10^{-4}$ -Inch Thick Ta Converter at a Generator Charging Voltage of 300 kV in 3 Meter Diameter Vacuum Tank. ( $E_{hv} < 120$  keV)

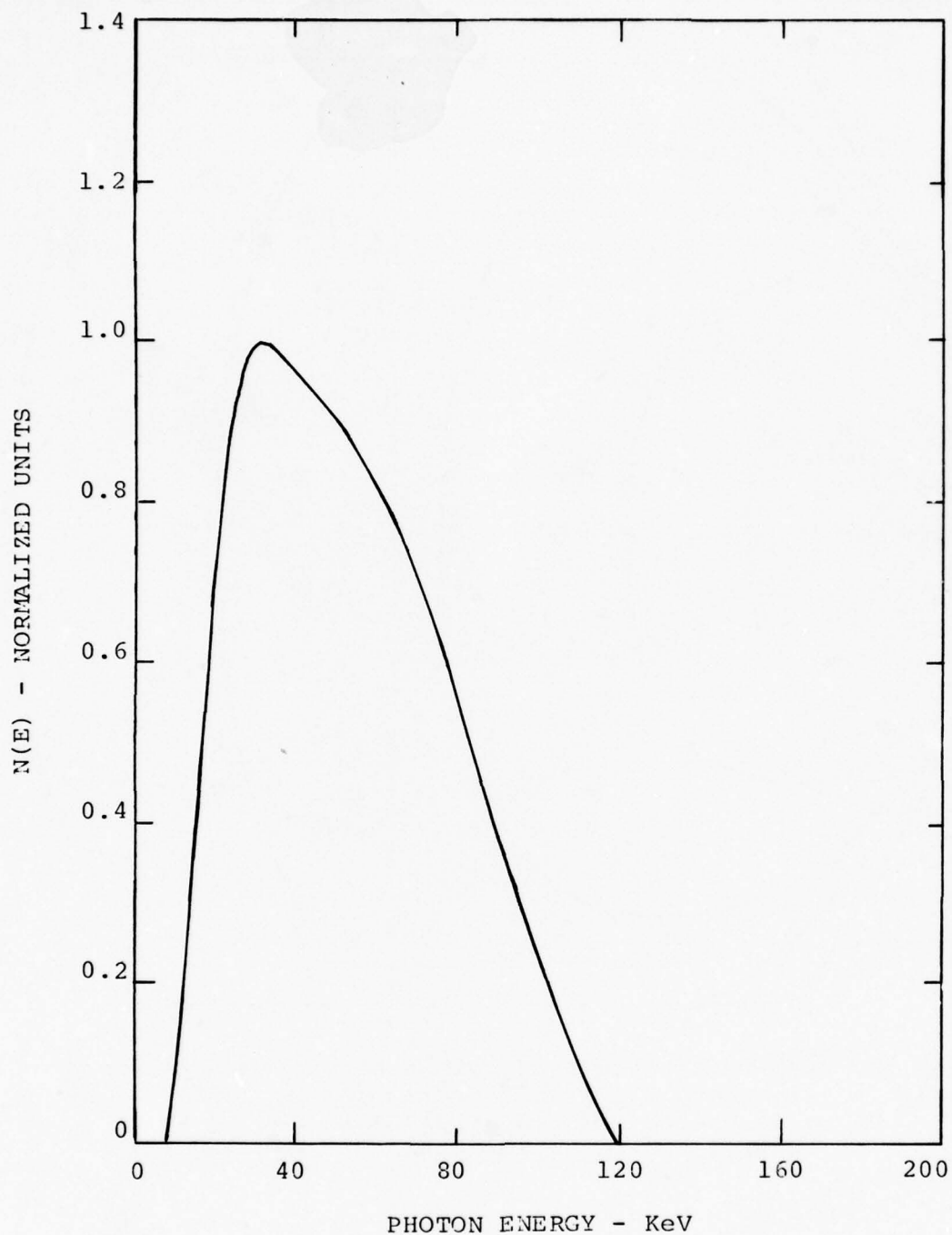
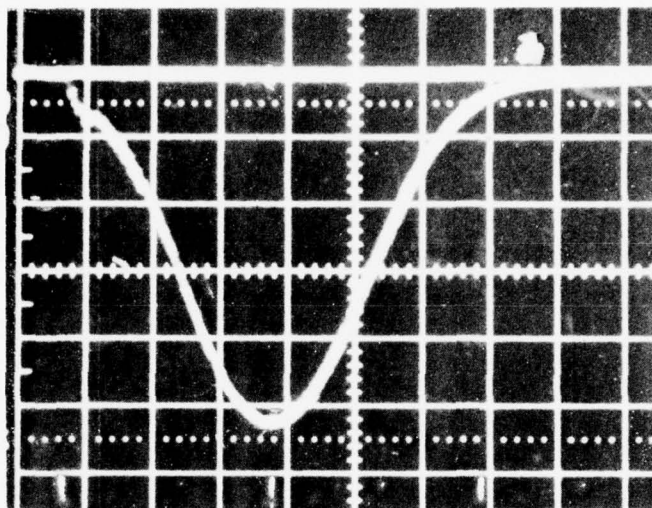


Figure 39. SPI-PULSE 6000 Bremsstrahlung Spectrum for a 12-Inch Diameter,  $3.5 \times 10^{-4}$ -Inch Thick Ta Converter at a Generator Charging Voltage of 300 kV. ( $E_{h\nu} < 120$  keV)



100 mV  
20 ns cm

Figure 40. SPI-PULSE 6000 Bremsstrahlung Time History  
for a 12-Inch Thick Ta Converter at a  
Generator Charging Voltage of 300 kV.  
( $E_{hv} < 120$  keV)

The calorimeter was specifically designed for photons with energies between 0 - 100 keV. A cross section of the diagnostic module is shown in Figure 41. The (0.020 X 0.5 inch) diameter foil is supported on a 0.00025-inch Mylar membrane to minimize heat conduction to the surrounding structure. It is located 1 mm behind a 0.5-inch diameter X 0.001-inch aluminum window which is transparent to the X-rays but helps isolate the foil from convective or radiative disturbances. The Mylar, with a thin aluminization, stops any scattered electrons that may be created at the window. Errors due to X-ray or photo electron scattering from the foil edges are minimized by keeping the thickness of the gold small compared to the diameter.

The thermistor is attached to the rear of the foil via a high thermally conductive grease. A simple circuit biased by 1.5 volts from an external battery monitors the thermistor output voltage and provides a signal which may be recorded on a suitable oscilloscope or other sensitive measuring device. The signal consists of a variation in a stable DC voltage level of  $\sim 400$  mv which must be biased out in order to be displayed on higher sensitivity scales. Figure 42 shows a typical output signal as the foil absorbs an X-ray burst. Notice the thermal decay constant is quite long. This signal was recorded on a Tektronix Type 551 oscilloscope (20 MHz) with a 1A7A plug-in preamp. This preamp has a maximum sensitivity of  $10 \mu$  volts/cm which allow fluence measurements down to  $10^{-5}$  cal/cm<sup>2</sup>.

### 7.3.2 Calorimeter Calibration Technique

An insitu calibration technique is used to determine the calorimeter's sensitivity in terms of cal/cm<sup>2</sup> per millivolt signal over a large temperature range. A precision temperature control plate is used to provide an accurate variation in



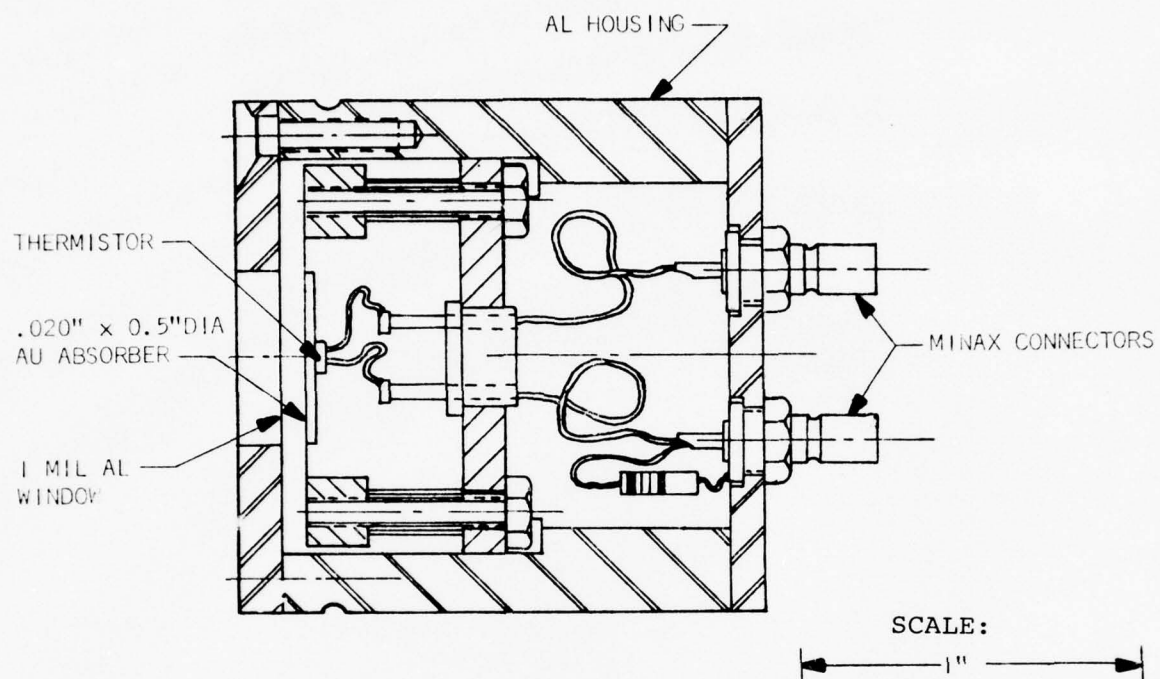
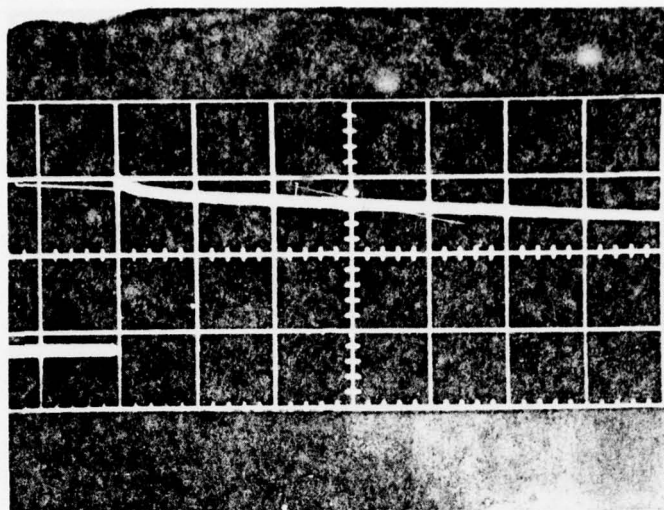


Figure 41. SPI's Gold Foil X-Ray Calorimeter



VERTICAL SENSITIVITY 0.5 mV / CM  
HORIZONTAL SWEEP 1 SEC / CM

Figure 42. X-Ray Calorimeter Output

temperature down to tenths of a degree Centigrade. The plate calibration was determined by comparison with a thermocouple circuit and a sensitive thermometer. The inner calorimeter assembly with membrane, foil and thermistor circuit is placed in series with the standard signal resistor in order to reduce the output voltage to a level which may be biased out by the measurement device. A recently calibrated Keithley Model 150A electrometer was used for this purpose. Figure 43 shows the calorimeter output signal versus temperature over the calibrated range of the control plate. This shows an almost straight line which indicates a constant calibration over the temperature range. The slope at different points was checked more accurately using smaller temperature increments. The resulting output calibration is plotted versus control plate temperature in Figure 44. However, since this depends on the temperature calibration of the plate, a second curve showing output sensitivity versus signal level is given in Figure 45. The calorimeter sensitivity is equal to the inverse of the calibration at any point and results in a curve of the opposite slope. Note that the sensitivity scale has been expanded and that the total variation over the range of interest is only a few percent. A temperature change  $\Delta T$ , is converted to an incident fluence,  $\Delta \phi$ , by multiplying by the areal mass,  $m/A$ , and the specific heat,  $C_p$ , of the gold foil:

$$\Delta \phi = \frac{m C_p \Delta T}{A}$$

Since the output relies directly on the biasing voltage which is supplied by the battery, the sensitivity was checked versus battery voltage. It was shown that the sensitivity varied  $\sim 2\%$  between 1.63 volts (new battery) and 1.5 volts but dropped off sharply below 1.5.

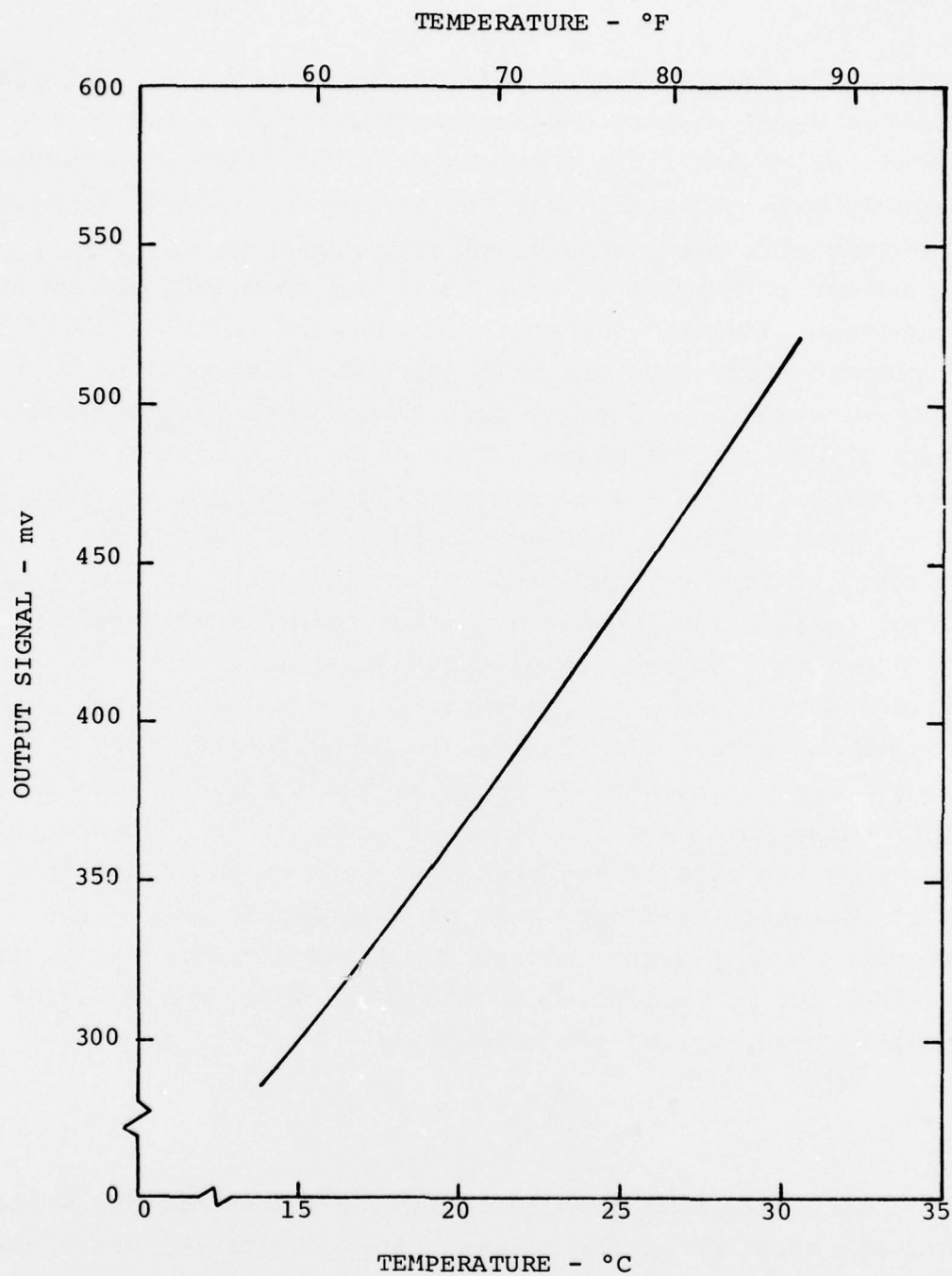


Figure 43. X-Ray Calorimeter Output Versus Ambient Temperature



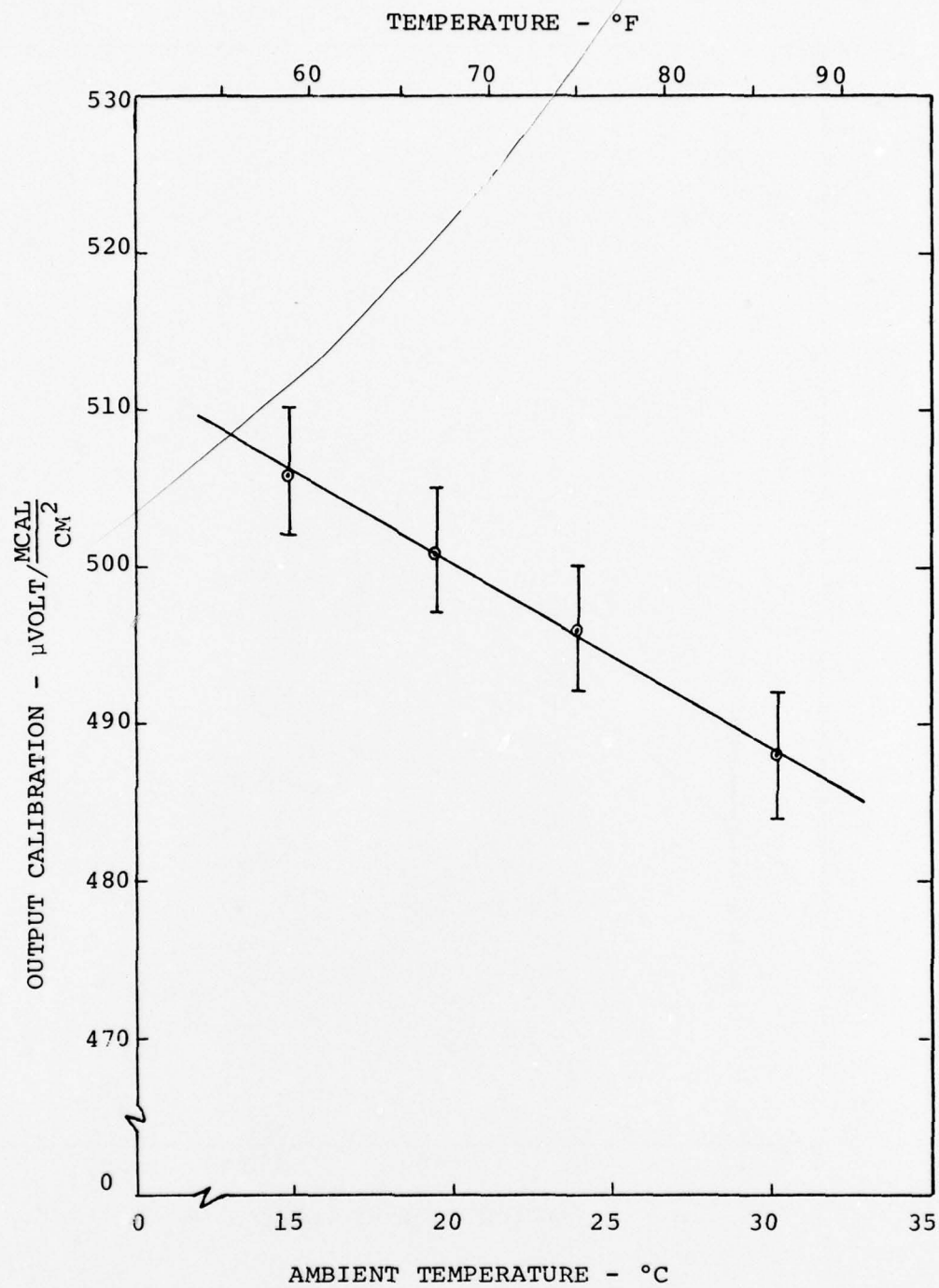


Figure 44. X-Ray Calorimeter Output Calibration Versus Ambient Temperature



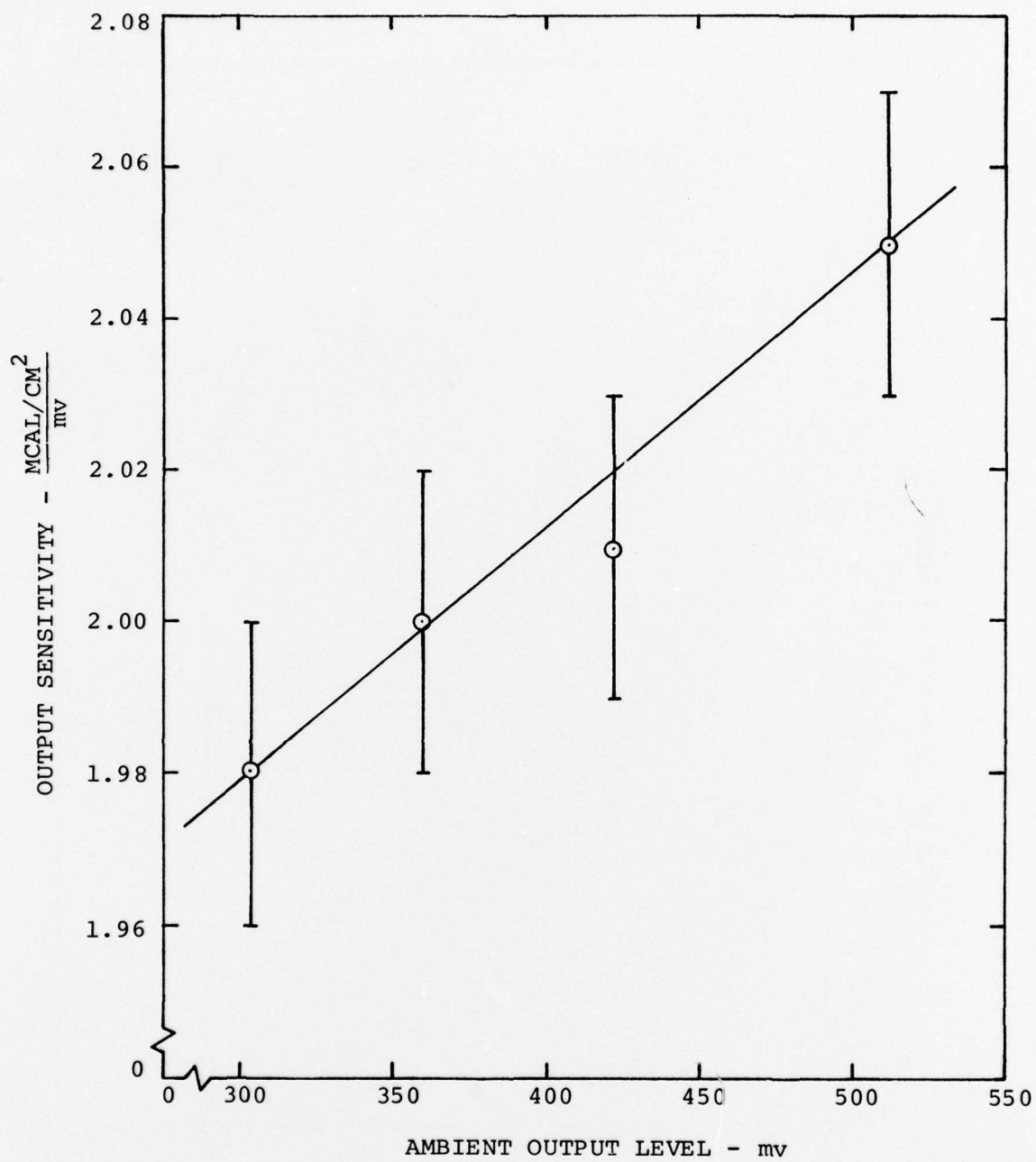


Figure 45. X-Ray Calorimeter Sensitivity Versus Output Level

## 7.4 SCINTILLATOR/PHOTODIODE

### 7.4.1 Description and Operation

The scintillator/photodiode is a pilot B scintillator/fast photodiode combination packaged in an RF tight module. It was designed to provide a time resolved waveform of a pulsed X-ray environment. A cross section of the diagnostic is shown in Figure 46. A cylindrical scintillator piece, shielded radially by lead sees incident photons through a thin aluminum window (0.3 inch diameter). The instrument is optimized for photons between 0 and 100 keV. Even at low energies the window is essentially transparent but maintains the RF and light integrity of the module. The scintillator converts a high percentage of the incident photons into light which can be detected by the thin cathode of the diode. Biased by 90 volts via a miniature coax connector (minax), the diode generates a current proportional to the incident light. The signal is recorded as a voltage waveform into the 50  $\Omega$  input of a scope via a second coax connector. The magnitude of the signal cannot be correlated directly with the quantity of incident photons since the conversion efficiency from X-rays to light in the scintillator is spectrum dependent.

The battery enclosed in an RF-tight box with coax connector and doubly shielded RG 174 coax cable are provided with the module. With the battery connected to the appropriate connector (they are labeled), the signal cable should be connected to the 50  $\Omega$  input of a scope. A 500 Mhz bandwidth is suggested in order to be compatible with the nanosecond risetime of the photodiode. Saturation of the diode occurs at  $\sim$  2 volts output signal; therefore a scope sensitivity of 1 volt/cm or greater will be necessary depending on the existing fluence levels.

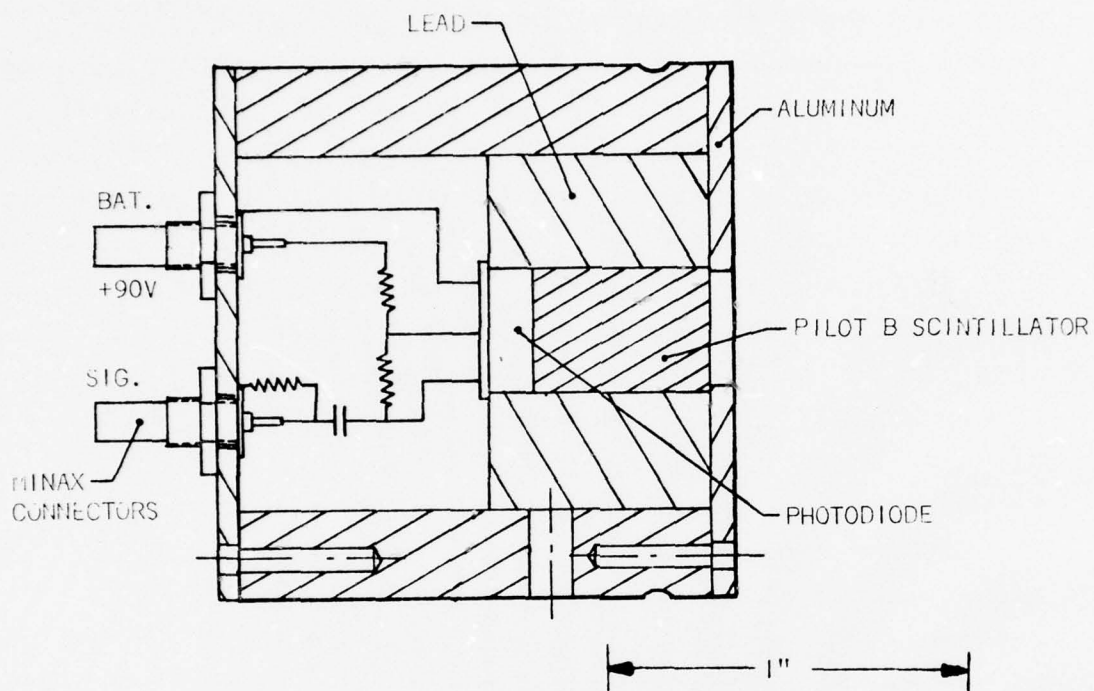


Figure 46. SPI's 500 mHz Scintillator Photodiode

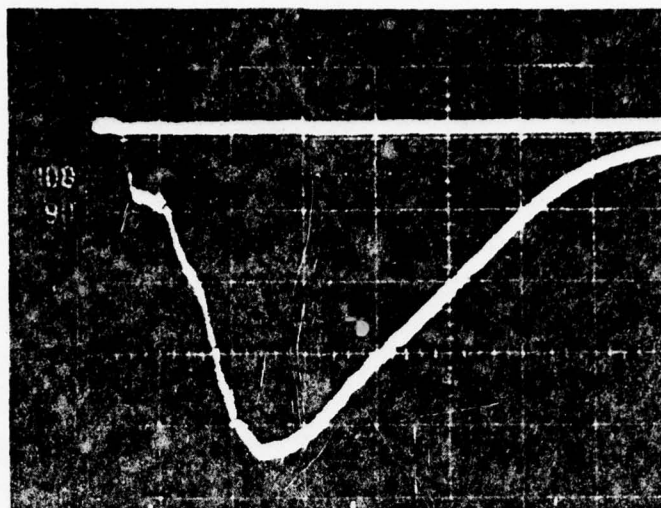
A rough calibration of the device was determined experimentally by measuring the output in a known environment. The SPI-PULSE 6000 charged to 200 keV produces a spectrum that approximates a 15 keV blackbody. In this environment, the output was:

$$150 \frac{\text{volts}}{\text{mcal/cm}^2}$$

A representative waveform is shown in Figure 47. It was recorded on a Tektronix Model 7904 oscilloscope (500 MHz) with a 7A19 preamp (maximum sweep rate - 0.5 ns/cm). With this environment and instrumentation the operational fluence range is:

$$10^{-8} - 10^{-3} \frac{\text{cal}}{\text{cm}^2}$$

The range can be extended to higher fluences by inserting optical filters between the scintillator and photodiode.



VERTICAL SENSITIVITY 20 mV / CM  
HORIZONTAL SWEEP 20 NS / CM

Figure 47. Scintillator/Photodiode  
Typical Output



## SECTION VIII

### SUMMARY

This report has presented the status of using low voltage pulsed electron beams for IEMP/SGEMP simulation and the status of low voltage bremsstrahlung X-ray environments.

Two specific examples of applying low voltage pulsed electron beams to IEMP/SGEMP simulation were discussed which demonstrated the utility of the technique. The dependence of IEMP in a 12-inch diameter cavity upon cavity depth and pressure was shown. SGEMP phenomenology was studied by ejecting electrons from the end of a cylinder. A major point to be made is that accurate electron beam diagnosis, necessary for meaningful experiments, is done on a routine basis.

Suggestions were made for further utilization of the electron beam capability that has been developed. In addition to a wide range of beam parameters for the geometries described, possibilities for increased IEMP cavity size and geometry changes in SGEMP test bodies were presented. Also, it is feasible to inject electrons into and cause electrons to be emitted from irregular non-planar surfaces. Finally, the possibilities for combined TREE and electron effects experiments were discussed and the utility of using the 10-foot diameter chamber to assess clear time effects was mentioned.

Using a tantalum target in place of the anode, the SPI-PULSE 6000 has been configured to produce low voltage bremsstrahlung X-rays. Maximum X-ray fluences of  $2 \times 10^{-3}$

cal/cm<sup>2</sup> can be produced using a 2.5-inch diameter cathode/anode geometry. Fluence maps and time histories are illustrated for all vacuum configurations available at SPI.

# REFERENCES

1. Little, R. G., S. H. Face and R. A. Lowell, "The Characterization of Pulsed Low Voltage Electron Beams for IEMP/SGEMP Simulation", Simulation Physics Report TR-76-04, Submitted to IEEE Meeting on Nucl. Sci., July, 1976.
2. Rosado, J., R. Genaudio, M. Kime, and R. Little, "Six Inch Diameter IEMP Experiments", Simulation Physics Report FR-73-10032, August, 1973.
3. Little, R. G., et. al., "Cavity Current Enhancement by Dielectrics", IEEE Trans. on Nucl. Sci., Vol. NS-20, No. 6, December, 1973.
4. Genaudio, R., and A. Bromborsky, "Charge and Current Neutralization Phenomena in Low-Impedance Diode Structures", IEEE Trans. on Nucl. Sci., Vol. NS-21, December, 1974.
5. "Large Area Electron Beam Experiments", Intel-RT 8101-011, HDL Contract No. DAAG 39-74-C-0006, July, 1975.
6. Fisher, et. al., "Experimental SGEMP Results Using Electron Beam Injection", IEEE Trans. on Nucl. Sci., Vol. NS-22, No. 6, December, 1975.
7. Gilbert, J., "Mighty Epic UGT SGEMP Experiment Definition", Air Force Weapons Laboratory, ME/S-13, January, 1976.
8. Stahl, R. H., et. al., "Pressure Effect on Space-Charge-Limited Current Transmitted Across a Cylindrical Cavity", IEEE Trans. on Nucl. Sci., Vol. NS-20, No. 6, December, 1975.
9. Sneider, S., "Electron Beam Simulation of IEMP in Scaled System Models", McDonnell Douglas Astronautics Company, MDAC Paper WD 2243, September, 1973.
10. To be Published, Stahl, R. and D. Osborn, Intelcom Rad Tech.
11. Little, R. G., et. al., "Cavity Current Enhancement by Dielectric Walls", IEEE Trans. on Nucl. Sci., Vol. NS-22, No. 6, December, 1975.
12. Wenaas, E. P., and S. H. Rogers, "Effects of Dielectrics on the SGEMP Response of Satellite Structures", Intelcom Rad Tech Topical Report Intel-RT 8111-082, AFWL Contract No. F29601-74-C-0039, July, 1975.

REFERENCES (Continued)

13. Rich, W. Foster, and Eugene P. DePlomb, "Studies Related to the Use of Electron Spraying as a Satellite SGEMP Response Simulation Technique", Kaman Science Corporation, February, 1976.
14. Lowell, R. A., "SPI-6000 X-ray Environment Generation and Characterization", Simulation Physics Report No. TR-76-02, March, 1976.
15. Hine, G. and G. Brownell, Radiation Dosimetry (New York, 1958).
16. Neal, W. R., "Design of SGEMP Vacuum Chamber Damping Tests", Simulation Physics Report FR-20026, ARO Subcontract 76-17-VKF, March, 1976.



## DISTRIBUTION LIST

### DEPARTMENT OF DEFENSE

Director  
Defense Advanced Rsch. Proj. Agency  
ATTN: NMR

Defense Documentation Center  
Cameron Station  
12 cy ATTN: TC

Director  
Defense Nuclear Agency  
ATTN: TISI Archives  
ATTN: DDST  
2 cy ATTN: RAEV  
3 cy ATTN: TITL, Tech. Library

Commander, Field Command  
Defense Nuclear Agency  
ATTN: FCLMC  
ATTN: FCPR

Director  
Interservice Nuclear Weapons School  
ATTN: Document Control

Chief  
Livermore Division, Field Command, DNA  
Lawrence Livermore Laboratory  
ATTN: FCPRL

Under Secretary of Def. for Rsch. & Engrg.  
ATTN: S&SS (OS)

### DEPARTMENT OF THE ARMY

Director  
BMD Advanced Tech. Ctr.  
Huntsville Office  
ATTN: RDMH-O

Commander  
BMD System Command  
ATTN: BDMSC-TEN

Dep. Chief of Staff for Rsch. Dev. & Acq.  
ATTN: DAMA-CSM-N

Commander  
Harry Diamond Laboratories  
ATTN: DELHD-RCC, Raine Gilbert  
ATTN: DELHD-RCC, John A. Rosado  
ATTN: DRXDO-TI, Tech. Lib.  
ATTN: DELHD-NP

Commander  
Redstone Scientific Information Ctr.  
U.S. Army Missile Command  
ATTN: Chief, Documents

Commander  
U.S. Army Electronics Command  
ATTN: DRSFL

### DEPARTMENT OF THE NAVY

Chief of Naval Research  
ATTN: Henry Mullaney, Code 427

Director  
Naval Research Laboratory  
ATTN: Code 5565, Pete Ulrich  
ATTN: Code 7750, Jack Davis

Officer-in-Charge  
Naval Surface Weapons Center  
ATTN: Code WA501, Navy Nuc. Prgms. Off.

Director  
Strategic Systems Project Office  
ATTN: NSP

### DEPARTMENT OF THE AIR FORCE

AF Weapons Laboratory, AFSC  
ATTN: SUL  
2 cy ATTN: DYC  
2 cy ATTN: NXS

Hq. USAF/RD  
ATTN: RDQSM

Commander  
Rome Air Development Center, AFSC  
ATTN: Edward A. Burke

SAMSO/DY  
ATTN: DYS

SAMSO/MN  
ATTN: MNNG  
ATTN: MNNH

Commander in Chief  
Strategic Air Command  
ATTN: XPFS  
ATTN: NRI-STINFO Library

SAMSO/XR  
ATTN: XRS

DEPARTMENT OF ENERGY

University of California  
Lawrence Livermore Laboratory  
ATTN: Tech. Info. Dept. L-3

Los Alamos Scientific Laboratory  
ATTN: Doc. Con. for Reports Lib.

Sandia Laboratories  
Livermore Laboratory  
ATTN: Doc. Con. for Theodore A. Dellin

Sandia Laboratories  
ATTN: Doc. Con. for 3141, Sandia Rpt. Coll.



DEPARTMENT OF DEFENSE CONTRACTORS

Aerospace Corporation  
ATTN: Library  
ATTN: Julian Reinheimer  
ATTN: Frank Hai  
ATTN: V. Josephson

Avco Research & Systems Group  
ATTN: Research Lib. A830, Rm. 7201

The Boeing Company  
ATTN: Preston Geren

Computer Sciences Corporation  
ATTN: Alvin T. Schiff

Dikewood Industries, Inc.  
ATTN: K. Lee  
ATTN: Tech. Lib.

General Electric Company  
Space Division  
Valley Forge Space Center  
ATTN: Joseph C. Peden, VFSC, Rm. 4230M

General Electric Company  
TEMPO-Center for Advanced Studies  
ATTN: William McNamara  
ATTN: DASIAC

Institute for Defense Analyses  
ATTN: IDA Librarian

IRT Corporation  
ATTN: Technical Library  
ATTN: Dennis Swift

JAYCOR  
ATTN: Library  
ATTN: Eric P. Wenaas

JAYCOR  
ATTN: Robert Sullivan

Kaman Sciences Corporation  
ATTN: Library  
ATTN: W. Foster Rich  
ATTN: Jerry I. Lubell

DEPARTMENT OF DEFENSE CONTRACTORS (Continued)

Lockheed Missiles & Space Co., Inc.  
ATTN: Dept. 85-85

McDonnell Douglas Corporation  
ATTN: Stanley Schneider

Mission Research Corporation  
ATTN: Conrad L. Longmire  
ATTN: Roger Stettner

Mission Research Corporation-San Diego  
ATTN: V. A. J. Van Lint  
ATTN: Library

R&D Associates  
ATTN: Technical Library  
ATTN: Leonard Schlessinger

Rockwell International Corporation  
ATTN: Technical Library

Science Applications, Inc.  
ATTN: Willaim L. Chadsey

Simulation Physics, Inc.  
ATTN: S. H. Face  
ATTN: R. A. Lowell  
ATTN: W. A. Seigler

Spire Corporation  
ATTN: Roger G. Little

SRI International  
ATTN: Library

Systems, Science & Software, Inc.  
ATTN: Technical Library  
ATTN: Andrew R. Wilson

TRW Defense & Space System Group  
ATTN: Tech. Info. Center/S-1930